NTNU
Norwegian University of
Science and Technology

Polarimetry using classical polarizing components and nanostructured beam splitting surfaces

Sigurd Aune Borstad

Master of Science in Physics and Mathematics
Submission date: June 2018
Supervisor: Morten Kildemo, IFY

Norwegian University of Science and Technology
Department of Physics

NTNU – Trondheim
Norwegian University of
Science and Technology

Analysis and Generation of the polarization state of light in combination with a supercontinuum laser source

Sigurd Aune Borstad
06.06.2018

Master's thesis
Department of Physics
Norwegian University of Science and Technology (NTNU).

Supervisor: Morten Kildemo.

Abstract

Two methods for generation and analysis of the polarization state of light are studied in this thesis. The first method is based on a traditional bulk design consisting of two active components and 3 passive components in order to optimally generate 4 Stokes vectors, and analyse one complete Stokes vector, respectively. The innovative step reported in this thesis is the combination of a 600-1100 nm 2-Ferroelectric Liquid Crystal (FLC) based system with a supercontinuum laser source tuned by an Acousto-Optic Tunable Filter (AOTF). The system operates as a complete spectroscopic Mueller matrix Ellipsometer for transmission measurements, using a single IngGaAs detector. It shows highly promising results in the 700 to 930 nm range with a sub 2% Mueller matrix element error. Equally good results in the 600 to 700 nm regime may also be possible.

The behaviour of the AOTF and the FLCs were studied in terms of switching speed and stability. The source reached a stable state within 2 milliseconds after switching, and was stable with a variation $<0.2\%$ in the short time regime. The FLCs revealed a tendency to drift a short time after switching, and a stable state was not reached until 0.2 seconds after switching was initiated.

The second method for generation and analysis of the polarization state of light is the use of passive beam splitting metasurfaces. I outline the design and production steps for beam splitting surfaces, and report the preliminary results for a manufactured Au/oxide/Au thin film stack. Production involves the deposition of a multilayered film consisting of two layers of Au with an intermediate layer of SiO_2, and thin adhesive layers of Ti. Characterisation of the films is performed using spectroscopic ellipsometry, Scanning Electron Microscopy (SEM), Atomic Force Microscopy (AFM), and 3D Optical Profilometry. Important properties such as deposition rate and the resulting surface roughness have been determined, and satisfying optical models for each of the materials and the multilayered film have been constructed. This forms a solid foundation for the production of films which can later be nanostructured into beam splitting surfaces.

Sammendrag

I denne oppgaven er to metoder for generering og analysering av polarisasjonstilstander til lys studert. Den første metoden baserer seg på et klassisk optisk komponentdesign bestående av to aktive og tre passive komponenter, hvor målet er å generere fire- og analysere én komplett Stokes vektor. En superkontinuerlig laserkilde, hvis bølgelengde på utsendt lys kontrolleres av en akusto-optisk modulator (AOM), har for første gang blitt kombinert med et 2-ferroelektrisk flytende krystall (FLK) basert system. FLK-systemet er optimert for målinger i det synlige og nær-infrarøde regimet, og fungerer, sammen med den superkontinuerlige kilden og en InGaAs detektor, som et komplett spektroskopisk Muellermatrise ellipsometer med målinger i transmisjon. Systemet viser lovende resultater i regimet fra 700 til 930 nanometer, med en 2% eller lavere feil i de 16 Muellermatriseelementene. Det er forventet at tilsvarende gode resultater skal være oppnåelig i regimet fra 600 til 700 nanometer.

Oppførselen til AOM'en og FLK'ene har blitt studert med tanke på stabilitet og tiden de bruker på å bytte fra en stabil tilstand til en annen. Lyskilden og AOM'en når en stabil tilstand innen 2 millisekunder, og som holdt seg stabil innenfor en feil på 0.2%. KLF'ene derimot skulle vise seg å drifte etter at et skifte var gjennomført, og nådde ikke en stabil tilstand før 0.2 sekunder hadde passert.

Den andre metoden for generering og analysering av polarisasjonstilstander baserer seg på bruken av polarisasjonssplittende overflater. Design og produksjonssteg av disse overflatene blir redgjort for, samt de første testene av en gull/silisiumoksid/gull-film blir presentert. Produksjonen involverer deponering av to lag med gull og et mellomliggende lag med silisiumoksid. Mellom lagene er det tynne, adherende lag med titan. Karakterisering med både spektroskopisk ellipsometri, atomkraftmikroskopi, skanningelektronmikroskopi og 3D optisk profilometri. Avgjørende parametre som deponeringsrate og resulterende overflateruhet har blitt fastsatt, og optiske modeller for de forskjellige materialene og den komplette filmen har blitt laget. Dette utgjør et solid grunnlag for produksjon av filmer som senere skal nanostruktureres til polarisasjonssplittende overflater.

Acknowledgments

This Master's thesis is the culmination of five beautiful years of study at NTNU. The project has been carried out at the Applied Optics Group, Department of Physics under the energetic supervision of Professor Morten Kildemo. A special thanks to you, Morten. You are quite the character, and I hope you never change.

PhD candidate Per Magnus Walmsness is another key figure to whom I owe a special thanks. I hope you treat every future Masters student as patiently as you have treated me, beeing a quality worthy of admiration.

I would also like to mention Tom André Hansen and Roland Richter since all my hours at the office have been ten times more fun with the two of you present.

Finally I would like to thank my beautiful Elisa for putting up with me and for reading my entire thesis in search of typos. I promise to now devote my fullest attention to you.

Trondheim, June 2018

Sigurd Aune Borstad

Contents

1 Introduction

Few have been more instrumental than Maxwell when it comes to establishing a theory of electromagnetism (EM) [1], and since the mid 1800s knowledge and understanding of this field has grown steadily. The ability to measure and control fundamental properties of EM waves like intensity, wavelength, coherence and polarisation [2, 3] opens a world of possibilities.

Natural examples of light polarisation occur all around us. For example, the unpolarised light from the sun can be polarised by Rayleigh Scattering in the atmosphere [4], or similarly light can be polarised when reflected from a surface [5][6]. Even though humans are capable of perceiving polarisation with the naked eye [7](an entoptic effect known as the Haidinger's brushes [8]), it is not something we benefit from as a species. There are, however, many animal species, particularly insects [9], who benefit. Both locusts [10] and bats [11] use polarised light to navigate, while for birds, polarised light can actually cause some confusion as it may interfere with their inner compass [12].

Polarimetry is the measurement and interpretation of the polarisation states of EM waves. It is a sensitive and nondestructive way of measuring the change in polarisation of an EM wave transmitted through, or reflected, diffracted or refracted by a sample. The goal of polarimetry to determine two or more components of the *Stokes vector*, where all four components completely describe the polarisation state of light [13]. An acknowledged way of doing this is by division-of-amplitude polarimetry. This makes use of both classical optical components, such as *Wollaston prisms* [14], as well as various types of gratings [15, 16], to split the various polarisations in different directions.

In its simplest form, polarimetry can be demonstrated by putting a piece of plastic between an LCD-screen and a polarisation filter as shown in Figure 1. Polarised light is emitted from the screen. The plastic will act like a retarder by causing a wavelength dependent phase-shift, changing the polarisation of the light. The transmittance through the polarisation filter will in turn be wavelength dependent, resulting in the observation of different colours.

EM waves will always have some degree of polarisation, no matter how small a fraction. This has enabled polarimetry to played a key role in the development of modern astronomy. The partly polarised light resulting from various interactions with dust grains, reveals information about numerous astronomical phenomenons such as nebulas, activity in debris disks, redshifts, supernovaes, and gamma ray bursts [17, 18].

Polarimetry takes on a more active role in a LIDAR (Light Detection and Ranging), where Stokes parameters of backscattered light from a pulsed laser are measured. LIDAR can give us information such as distances, Earth-surface properties [19], and ice to water ratio in a cloud [20]. Another active form of polarimetry, commonly known as *ellipsometry*, is a cornerstone within the characterisation of thin films. It is an excellent tool to determine the thickness and optical properties of films, and can also be used to

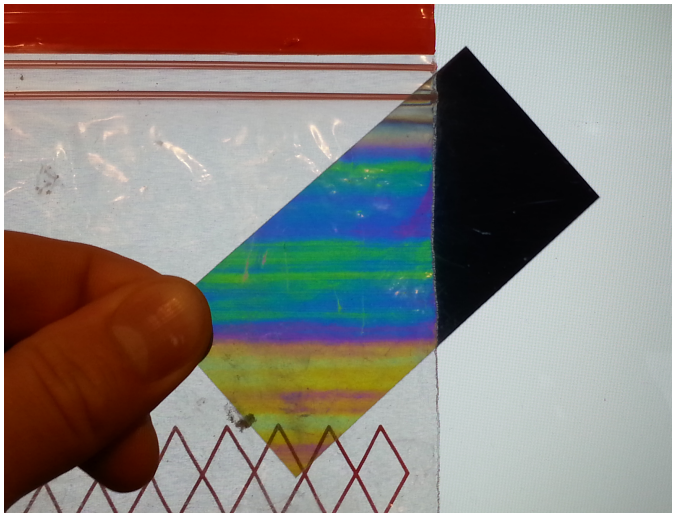

Figure 1: A demonstration of photoelasticity by holding a piece of plastic between an LCD screen and a linear polariser.

study nanostructures [21], strain evolution [22], and more.

Ellipsometers contain a set of optical components which create multiple generating and analysing states. A photo-elastic modulator (PEM) [23] is one such component, which makes use of the photoelastic effect to produce a time-varying birefringence [24, 25, 26]. Similarly, one can exploit the electro-optic effect [27] and use electro-optic modulators (EOM) [28, 29]. Finally, one can use Pockel's cells [30], rotating prisms retarders [31], or waveplates [32].

Standard ellipsometry is limited in the sense that it can only measure some of the Mueller matrix elements of the sample. It is therefore not applicable for anisotropic samples or diffractive structures. *Mueller Matrix Ellipsometry*, on the other hand, identifies all the 16 Mueller matrix components of a sample, which completely describes the polarisation response of the material. It is a powerful technique for the study and accurate determination of the dielectric function, the optical properties, and the geometric characteristics of anisotropic materials and complex systems. Mueller matrix imaging ellipsometry is regarded as a low cost *in-situ* alternative to the currently available metrology methods, such as scanning electron microscopy (SEM), atomic force microscopy (AFM), and transmission electron microscopy (TEM) [33] [34].

Common light sources in an ellipsometer are monochoromatic lasers or a broad band light source, e.g. a Xenon lamp. The introduction of a supercontinuum laser will provide distinct advantages, both for general spectroscopy and imaging systems. The high intensity of lasers enables both fast measurements and off-axis ellipsometry, known as *Scatterometry*. The bright beam of high spatial coherence can be focused into a microscopic spot, enabling fast high resolution spectroscopic scanning imaging. Its brightness makes it highly suitable for characterisation of scattering samples, such as tissue, both in

transmission and reflection. This makes it ideal for biomedical purposes and offers new and exciting opportunities within a field that still has a potential for various ellipsometric applications.

While ellipsometry has been utilised for multiple biomedical purposes [35, 36], the geometrical restrictions make *in-vivo* measurements troublesome [37, 38]. This is one of many areas that will benefit greatly from a miniaturisation in polarisation controlling components.

A step in this direction is the creation of beam splitting metasurfaces [39]. Operating similarly to a blazed grating, a beam splitting metasurface will passively split incident orthogonal polarisations. A small, non-moving, electricity independent optical component has a huge potential for applications where size and simplicity are imperative.

The NTNU Polarimetry, Plasmonics and Metamaterials group has developed several concepts and prototype Mueller Matrix Ellipsometer systems including multistate liquid crystal variable retarders (LCVR) [40], 2 and 3-ferroelectric liquid crystal (FLC) based systems [41], and electro-optic modulator systems [42]. Some of the systems have been optimized using genetic algorithms [43]. In terms of light sources, multiple lasers were used for light scattering instruments, and near infrared (NIR) LEDs [44] and NIR lasers were used for NIR-Mueller Matrix Imaging (MMI) [45]. The systems operated in spectroscopy mode and imaging mode, and may form a solid foundation for hyperspectral (multiwavelength) Mueller matrix imaging.

One of the main goals of this thesis is to combine a supercontinuum laser source with a 2-Ferroelectric Liquid Crystal (FLC) bulk system for fast spectroscopic Mueller matrix ellipsometry in the bio-medical diagnostic window (600-1100 nm). The introduction of a new laser source will require thorough testing to decide if it is suited for this application. The high intensity of the supercontinuum source and the range in which it operates makes the bulk system well suited for characterisation of strongly scattering materials such as biological samples. The system can easily be altered to measure samples in reflection. It is also envisioned as a Mueller matrix imaging system, and one goal will be to determine if this is feasible or not.

An additional project, with the goal of creating polarisation splitting metasurfaces, has also been initiated. The first step of this project will be to create and characterise multilayered thin films. The films will be produced at the NTNU NanoLab. Both surface studies and ellipsometric characterisation will then be performed, in order to construct an optical model of the multilayered film. After creating and characterising the films nanostructuring and final testing should be carried out, but this is outside the time frame of this thesis. This additional project is particularly interesting as Beam splitting surfaces have enormous potential in cases where classical bulk systems are impractical, such as for *in-vivo* measurements or applications in space.

Chapter 2 gives an overview of the fundamental theory of light as electromagnetic waves. Nonlinear optics and supercontinuum generation is also discussed. Chapter 3 gives a

general introduction to ellipsometry, and a more detailed explanation of the spectroscopic ellipsometer constructed. Chapter 4 summarises the creation and characterisation, both optical and non-optical, of the multilayered thin films. Chapter 5 describes the realisation of the Mueller matrix spectroscope, focusing on components and controlling software. Results and improvements for both projects are discussed in Chapter 6, and in Chapter 7 the thesis is concluded.

2 Theory

2.1 Polarized Light

The general differential form of Maxwell's equations

$$\begin{aligned} \nabla \cdot \vec{E} &= \frac{1}{\epsilon_0}\rho, & \nabla \times \vec{E} &= -\frac{\partial \vec{B}}{\partial t}, \\ \nabla \cdot \vec{B} &= 0, & \nabla \times \vec{B} &= \mu_0 \vec{J} + \mu_0 \epsilon_0 \frac{\partial \vec{E}}{\partial t}, \end{aligned}$$

fully describes classical electromagnetic waves. The two curl equations can be combined to eliminate the magnetic field giving us the electric field vector $\vec{E}(\vec{r},t) = (E_x(\vec{r},t), E_y(\vec{r},t), E_z(\vec{r},t))^T$. Now considering a plane wave propagating in the z-direction, one has $E_z(\vec{r},t) = 0$, and the wave can be expressed by a superposition of an electric field oscillating in the $\hat{x}$ and $\hat{y}$ direction

$$\vec{E}(z,t) = \Re[E_x(z,t)\hat{x} + E_y(z,t)\hat{y}], \tag{2.1}$$

where the field in the x- and y-direction is written as

$$\begin{aligned} E_x(z,t) &= E_{x0} e^{i(\omega t - kz + \delta_x)} \\ E_y(z,t) &= E_{y0} e^{i(\omega t - kz + \delta_y)} \end{aligned} \tag{2.2}$$

where E_{n0} is the real amplitude of the electric field in the n-direction and ω, k and δ_n are the angular frequency, wave number, and phase factor, respectively. The polarisation ellipse can be deduced from equation (2.2)

$$\left(\frac{E_x}{E_{0x}}\right)^2 + \left(\frac{E_y}{E_{0y}}\right)^2 - 2\left(\frac{E_x E_y}{E_{0x} E_{0y}}\right)\cos\delta = \sin^2\delta, \tag{2.3}$$

where the phase shift $\delta = \delta_x - \delta_y$. In the case of $\delta = n\pi$ equation (2.3) will trace a linear line, while $\delta = n\pi + \pi/2$ will trace a perfect circle. Any value between these two will give an ellipse. The polarisation state is therefore determined by the ratio E_x/E_y and the phase shift δ, giving linearly polarised light in the case of $\delta = n\pi$ and circularly polarised light when $\delta = n\pi + \pi/2$. In *Principles of Optics* [46] polarisation is defined as right-handed when $sin(\delta) > 0$ with the instantaneous electric field vector forming a right-handed helix in space.

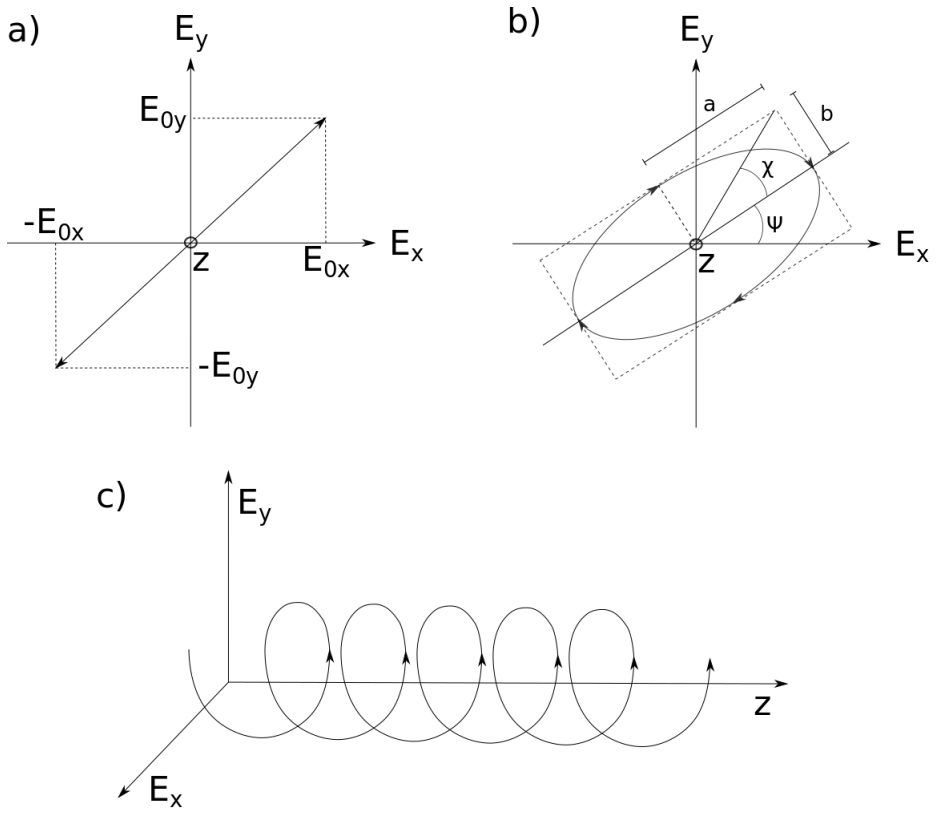

Figure 2: Figure a) shows linear polarisation, while Figure b) shows an elliptical polarisation whos shape is specified by the azimuth angle, Ψ, and the ellipticily, χ. Figure c) exhibits a right handed space-dependent field propagating in the z-direction.

2.2 Jones Formalism

It can be cumbersome to study the propagation of polarized light through optical elements using amplitudes and phases. Jones introduced a matrix formalism [47] to simplify these calculations. Equation (2.1) can be rewritten in vector form, representing the complex electric field vector when time- and space dependencies have been removed

$$\vec{E} = \begin{bmatrix} E_x \\ E_y \end{bmatrix} = \begin{bmatrix} E_{0x} e^{i\delta_x} \\ E_{0y} e^{i\delta_y} \end{bmatrix}. \tag{2.4}$$

The Jones matrix $\mathbf{J}$ is a 2×2 matrix describing an optical component. Together with the Jones vector this can be used to describe the change of polarisation state of an electromagnetic wave as it passes through the optical component. The outgoing Jones' vector $\vec{E}'$ is a product of the Jones' matrix $\mathbf{J}$ and the incoming vector $\vec{E}$

$$\vec{J'} = \mathbf{J}\vec{J}. \tag{2.5}$$

In the case of multiple optical components, $\mathbf{J}_1$,$\mathbf{J}_2$ $\ldots$ $\mathbf{J}_N$, these components will be equivalent to one system given by the Jones matrix $\mathbf{J}_{sys}$=$\mathbf{J}_n$·$\mathbf{J}_{n-1}$· $\ldots$ $\mathbf{J}_1$ and the calculations will be as shown above. A selection of Jones matrices can be found in Appendix A.

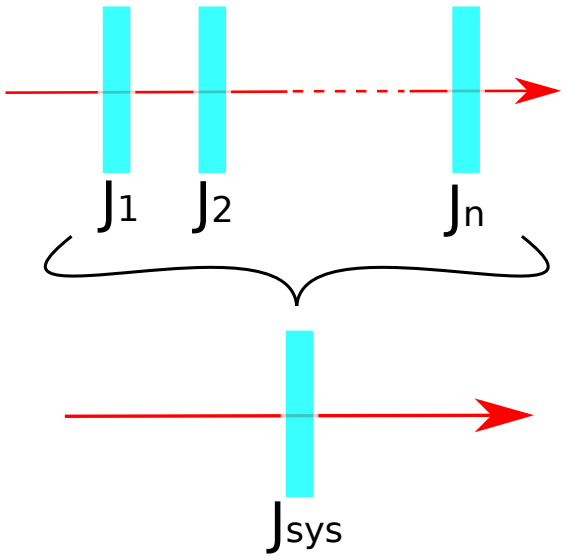

Figure 3: A set of Jones matrices can be multiplied together and treated as one system matrix.

When many optical components are used, some or all of them individually rotational, a fixed coordinate system is needed. The Jones matrix for an optical device that has been rotated an angle α between the u-axis in our fixed uv-system and the x-axis of the input coordinate system of the device is given by

$$\mathbf{J}^{uv} = \mathbf{R}(-\alpha)\mathbf{J}^{xy}\mathbf{R}(\alpha). \tag{2.6}$$

2.3 Polarising Optical Elements

A polarising optical element can modify the polarisation state of light. This means that the components of the electric field vector will experience a change in amplitude and/or phase. Some important polarising optical elements are polarisers and retarders.

2.3.1 Polarisers

Before explaining polarisers the **diattenuator** needs to be introduced. A diattenuator is an optical element that does not change the phase difference between fields in the x-

and y-directions. It is denoted by a Jones matrix

$$\mathbf{J}_D = \begin{bmatrix} p_x & 0 \\ 0 & p_y \end{bmatrix}, \tag{2.7}$$

where p_x and p_y, often written on the form $p_i = e^{\alpha_i d}$ where d is the thickness of the optical element, are real-valued amplitude transmission coefficients with values between 0 and 1. Uneven transmission ($p_x \neq p_y$) will give us partially polarised light, and in the case where the diattenuation,

$$D_{\mathbf{J}_P} = \frac{|p_x^2 - p_y^2|}{p_x^2 + p_y^2}, \tag{2.8}$$

reaches unity, the light is perfect linearly polarised. There are many types of polarisers; beam splitter polarisers [48], doubleprism polarisers, and Brewster's-angle polarisers [5] are a few specific examples.

2.3.2 Retarders

Most linear retarders, often known as *waveplates*, are optical components which alter the polarisation state by "delaying" one of the two perpendicular electric field components. They are made out of crystals with anisotropic electric properties, so called *birefringent* materials. In electrically anisotropic materials the electric displacement vector and the electric field vector are no longer parallel, and the electric permittivity ε takes on the form of a second rank tensor ε_{ij}

$$\vec{D} = \boldsymbol{\varepsilon}\vec{E}, \qquad \boldsymbol{\varepsilon} = \begin{bmatrix} \varepsilon_{11} & \varepsilon_{12} & \varepsilon_{13} \\ \varepsilon_{21} & \varepsilon_{22} & \varepsilon_{23} \\ \varepsilon_{31} & \varepsilon_{32} & \varepsilon_{33} \end{bmatrix}. \tag{2.9}$$

Letting our coordinate system coincide with the principal axes of the permittivity tensor, the tensor becomes diagonal and can be rewritten as

$$\boldsymbol{\varepsilon} = \begin{bmatrix} \varepsilon_1 & 0 & 0 \\ 0 & \varepsilon_2 & 0 \\ 0 & 0 & \varepsilon_3 \end{bmatrix}. \tag{2.10}$$

In an isotropic material like glass, all the diagonal elements will be the same, while for a birefringent material, either one (uniaxial) or two (biaxial) of the elements will differ. For a uniaxial material like calcite, the tensor (2.10) is written

$$\boldsymbol{\varepsilon} = \begin{bmatrix} \varepsilon_o & 0 & 0 \\ 0 & \varepsilon_o & 0 \\ 0 & 0 & \varepsilon_e \end{bmatrix}, \tag{2.11}$$

where ε_o is the permittivity of the fast axis, also called the *Ordinary* axis, and ε_e the permittivity of the slow axis, or the *Extraordinary* axis, referring to the propagation speed of the wave. The corresponding ordinary wave velocity is $v_o = 1/\sqrt{\mu_0 \varepsilon_o}$, where μ_0 is the vacuum permeability, and the ordinary refractive index $n_o = c/v_o$. Similarly, $v_e = 1/\sqrt{\mu_0 \varepsilon_e}$ and $n_e = c/v_e$. This difference in propagation speed will cause a phase shift, δ, between the two electric field components given by

$$\delta = \frac{2\pi}{\lambda} d\,(n_e - n_o)\,, \tag{2.12}$$

where λ is the wavelength observed along the ordinary axis, d is the thickness of the retarder, and n_o and n_e are the refractive indices along the ordinary and extraordinary axes, respectively. The Jones' matrix of a retarder is written

$$\mathbf{J}_R = \begin{bmatrix} 1 & 0 \\ 0 & e^{-i\delta} \end{bmatrix}. \tag{2.13}$$

A phase shift of $\pi/2$ can change a linear polarisation into a circular one, and components with this phase shift are known as quarter-wave plates. Components resulting in a phase shift of π are called a half-wave plates, and can be used to change the direction of a linear polarisation.

2.4 Stokes Formalism and the Mueller Matrix

The Jones formalism is useful when dealing with fully polarised light and optical components which do not compromise the polarisation. This formalism is, however, not sufficient when light is only partially or non-polarised, or when the polarised light becomes depolarised during propagation. Rather than basing models on amplitude and phase, parameters not easily measured, Stokes introduced a 4D vector with real-valued elements in the dimension of irradiance. This vector can describe fully polarised light, partially polarised light, and unpolarised light, as well as both quasi-monochromatic and monochromatic light. This making it superior in most cases compared to Jones' formalism.

The Stokes column vector is defined as

$$\vec{S} = \begin{bmatrix} s_0 \\ s_1 \\ s_2 \\ s_3 \end{bmatrix} = \begin{bmatrix} I_{0^\circ} + I_{90^\circ} \\ I_{0^\circ} - I_{90^\circ} \\ I_{45^\circ} - I_{-45^\circ} \\ I_R - I_L \end{bmatrix} = \begin{bmatrix} \langle E_{0x}^2 \rangle + \langle E_{0y}^2 \rangle \\ \langle E_{0x}^2 \rangle - \langle E_{0y}^2 \rangle \\ 2\langle E_{0x} E_{0y} \rangle \cos\delta \\ 2\langle E_{0x} E_{0y} \rangle \sin\delta \end{bmatrix} = A^2 \begin{bmatrix} 1 \\ \cos 2\Psi \cos 2\chi \\ \sin 2\Psi \cos 2\chi \\ \sin 2\chi \end{bmatrix}, \tag{2.14}$$

where I_{0° and I_{90° are the irradiances for linear polarisations in the x and y directions, $I_{\pm 45^\circ}$ are the irradiances in the $\pm 45^\circ$ directions, and I_R and I_L are the irradiances for right and left polarised light. $\langle\rangle$ signifies the time average. All these irradiances are measurable using simple optical components. s_0 describes the total irradience of the

light, s_1 describes the difference in irradience between the $x-$ and $y-$components, s_2 describes the difference in irradience between the $+45°$ and $-45°$ directions, while s_3 describes the difference between the irradience of the left- and right-circulated states of polarisation.

An important quantity from the Stokes vector is the degree of polarisation (DOP), P, given by

$$P = \frac{I_{pol}}{I_{tot}} = \frac{\sqrt{s_1^2 + s_2^2 + s_3^2}}{s_0}, \tag{2.15}$$

where P will reach unity for fully polarised light, and zero for non-polarised light.

The following table gives an overview of selected polarisations represented in both Jones and Stokes vectors

Table 1: The Jones' and Stokes vectors for different polarisations.

Polarisation	Jones vector	Stokes vector
Unpolarised	N/A	$[1\ 0\ 0\ 0]^T$
Linear horizontal	$[0\ 1]^T$	$[1\ 1\ 0\ 0]^T$
Linear vertical	$[1\ 0]^T$	$[1\ -1\ 0\ 0]^T$
Linear $\pm 45°$	$\frac{1}{\sqrt{2}}[1\ \pm 1]^T$	$[1\ 0\ \pm 1\ 0]^T$
Right circular	$\frac{1}{\sqrt{2}}\ [1\ -i]^T$	$[1\ 0\ 0\ 1]^T$
Left circular	$\frac{1}{\sqrt{2}}\ [1\ +i]^T$	$[1\ 0\ 0\ -1]^T$

The Stokes vector can also be visualised by introducing the Poincaré sphere, formulated by H. Poincaré in 1892. A unit vector defined by

$$\vec{u} = \frac{1}{s_0} \begin{bmatrix} s_1 \\ s_2 \\ s_3 \end{bmatrix}$$

spans the Poincaré sphere starting with unpolarised light in the origin, and increasing towards fully polarised light at the surface. The south and north poles represent circular polarisation, the equator represents different states of linear polarisation, while all other points represents elliptical states of polarisation. An addition to equation (2.16) can thus be written

$$\vec{S} = A^2 \begin{bmatrix} 1 \\ \cos 2\Psi \cos 2\chi \\ \sin 2\Psi \cos 2\chi \\ \sin 2\chi \end{bmatrix}, \tag{2.16}$$

where $A = \sqrt{I}$, I being the total irradiance.

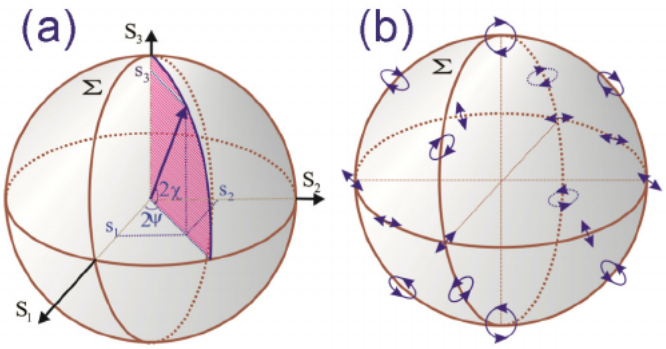

Figure 4: The Pointcaré sphere [49]: Figure (a) shows how a point on the sphere with longitude 2Ψ and latitude 2χ is represented by a polarisation state shown in Figure (b). The polarisation state is specified by the azimuth angle, Ψ, and the ellipticity, χ.

2.4.1 Mueller Matrices

Analogous to the Jones matrix definition (2.5), a 4x4 matrix description called the Mueller-matrix formalism was established [50]. The Mueller matrix describes the transformation of a Stokes vector, and is denoted as

$$\mathbf{M} = \begin{bmatrix} m_{11} & m_{12} & m_{13} & m_{14} \\ m_{21} & m_{22} & m_{23} & m_{24} \\ m_{31} & m_{32} & m_{33} & m_{34} \\ m_{41} & m_{42} & m_{43} & m_{44} \end{bmatrix}. \tag{2.17}$$

In the same way a Jones matrix transforms a Jones vector, a Mueller matrix will transform an incoming Stokes vector $\vec{S}$ into an outgoing Stokes vector $\vec{S}'$

$$\vec{S}' = \mathbf{M}\vec{S}. \tag{2.18}$$

As with Jones matrices, the combined effect of a series of N optical elements will be

$$\vec{S}' = \mathbf{M}_{sys}\vec{S}, \qquad \text{where} \qquad \mathbf{M}_{sys} = \mathbf{M}_N\mathbf{M}_{N-1}\ldots\mathbf{M}_1. \tag{2.19}$$

The 4x4 Mueller matrix is linked to the 2x2 Jones matrix by the relation

$$\mathbf{M} = \mathbf{A}(\mathbf{J} \otimes \mathbf{J}^*)\mathbf{A}^{-1}, \tag{2.20}$$

where $\otimes$ is the Kronecker product, $*$ is the complex conjugate, and $\mathbf{A}$ is the conversion matrix

$$\mathbf{A} = \begin{bmatrix} 1 & 0 & 0 & 1 \\ 1 & 0 & 0 & -1 \\ 0 & 1 & 1 & 0 \\ 0 & i & -i & 0 \end{bmatrix}. \tag{2.21}$$

Rotating a Mueller matrix around a coordinate system is done in the same manner as for a Jones matrix (2.6)

$$\mathbf{M}(\theta) = \mathbf{R}(-\theta)\mathbf{M}\mathbf{R}(\theta). \tag{2.22}$$

Some of the more important Mueller matrices can be found in Appendix B. It is also important to note that in order to construct a Mueller matrix, there are two conditions that must be fulfilled. Both the degree of polarisation (2.15) of the outgoing Stokes vector and the transmission of the Mueller matrix must not exceed unity. These conditions are known as the *polarisation-* and *gain* constraints [51, 52, 53].

2.5 Analysing the Mueller Matrix

The Mueller matrix (2.17) can be written in a short hand form

$$\mathbf{M} = m_{11} \begin{bmatrix} 1 & \vec{D}^T \\ \vec{P} & \mathbf{m} \end{bmatrix}, \tag{2.23}$$

where $\mathbf{m}$ is a $3x3$ matrix

$$\mathbf{m} = \frac{1}{m_{11}} \begin{bmatrix} m_{22} & m_{23} & m_{24} \\ m_{32} & m_{33} & m_{34} \\ m_{42} & m_{43} & m_{44} \end{bmatrix}, \tag{2.24}$$

and $\mathbf{P}$ and $\mathbf{D}$ are the polarisance and diattenuation vectors, respectively

$$\vec{P} = \frac{1}{m_{11}} \begin{bmatrix} m_{21} \\ m_{31} \\ m_{41} \end{bmatrix}, \qquad \vec{D} = \frac{1}{m_{11}} \begin{bmatrix} m_{12} \\ m_{13} \\ m_{14} \end{bmatrix}. \tag{2.25}$$

Polarisance describes the change from the unpolarized incoming Stokes vector to the outgoing Stokes vector. Diattenuation was explained in section 2.3.1. Polarisance, diattenuation, and depolarisation are properties that can be extracted directly from the Mueller matrix without any assumptions. The depolarisation index is defined as [54]

$$P_D = \sqrt{\frac{T_r(\mathbf{M}^T\mathbf{M}) - M_{11}^2}{3M_{11}^2}} = \sqrt{\frac{\Sigma_{i,j} M_{i,j}^2 - M_{11}^2}{3M_{11}^2}}, \tag{2.26}$$

with Tr representing the trace. $P_D = 1$ and $P_D = 0$ signify a non-depolarising and a fully depolarising matrix, respectively. The last property that can be directly extracted from the Mueller matrix is the transmittance/reflectance which comes straight from m_{11}.

There are multiple ways to break down a general Mueller matrix in order to make it less complex and easier to solve. One method, suggested by Azzam [55] and improved by Ossikovski [56], is differential decomposition. This is applicable when all polarisation effects happen simultaneously and in the transmission geometry. Mueller matrix root decomposition [57] was another suggested method, later proven equivalent [58] to the third and more robust method applied in this thesis, *forward product decomposition.*

2.5.1 Forward Product Decomposition

Forward product decomposition was proposed by Lu and Chipman [59] in 1996. This technique breaks the Mueller matrix into a product of three matrices: a diattenuator, a retarder, and a depolariser

$$\mathbf{M} = \mathbf{M}_\Delta \mathbf{M}_R \mathbf{M}_D. \tag{2.27}$$

The diattenuation matrix $\mathbf{M}_D$ is defined as

$$\mathbf{M}_D = \begin{bmatrix} 1 & \vec{D}^T \\ \vec{D} & \mathbf{m}_D \end{bmatrix}, \tag{2.28}$$

where $\vec{D}$ is defined in equation (2.25) and $\mathbf{m}_D$ is defined as the 3 x 3 matrix

$$\mathbf{m}_D = \sqrt{1-D^2}\mathbf{I} + \left(1 - \sqrt{1-D^2}\hat{D}\hat{D}^T\right). \tag{2.29}$$

Here $D = |\vec{D}|$, $\mathbf{I}$ is the 3x3 identity matrix, and $\hat{D} = \vec{D}/D$. By introducing a new Mueller matrix $\mathbf{M}'$, defined as

$$\mathbf{M}' = \mathbf{M}\mathbf{M}_D^{-1} = \mathbf{M}_\Delta \mathbf{M}_R, \tag{2.30}$$

we can use $\mathbf{M}_D$ to find $\mathbf{M}_\Delta$ and $\mathbf{M}_R$. The matrices are written

$$\mathbf{M}_\Delta = m_{11}\begin{bmatrix} 1 & \vec{0}^T \\ \vec{P}_\Delta & \mathbf{m}_\Delta \end{bmatrix}, \qquad \mathbf{M}_R = m_{11}\begin{bmatrix} 1 & \vec{0}^T \\ \vec{0} & \mathbf{m}_R \end{bmatrix}, \qquad \mathbf{M}' = m_{11}\begin{bmatrix} 1 & \vec{0}^T \\ \vec{P}_\Delta & \mathbf{m}' \end{bmatrix}, \tag{2.31}$$

where $\mathbf{m}' = \mathbf{m}_\Delta \mathbf{m}_R$ and

$$\vec{P}_\Delta = \frac{\vec{P} - \mathbf{m}\vec{D}}{1 - D^2}. \tag{2.32}$$

$\vec{P}_\Delta$ is the polarisance vector of $\mathbf{M}_\Delta$ and in the same manner as for $\vec{P}$ (2.26), the depolarisation power Δ_p can be calculated using the following equation

$$\Delta_p = 1 - \frac{|Tr(\mathbf{m}_\Delta)|}{3} = 1 - \frac{|Tr(\mathbf{M}_\Delta) - 1|}{3}. \tag{2.33}$$

As done by Manhas et. al. [60], the matrix $\mathbf{m}_\Delta$ can be constructed with the eigenvalues λ_1, λ_2 and λ_3 of $\mathbf{m}'(\mathbf{m}')^T$

$$\begin{aligned}\mathbf{m}_\Delta = \pm \left[\mathbf{m}'(\mathbf{m}')^T + \left(\sqrt{\lambda_1\lambda_2} + \sqrt{\lambda_2\lambda_3} + \sqrt{\lambda_1\lambda_3}\right)\right]^{-1} \times \\ \left[\left(\sqrt{\lambda_1 + \lambda_2 + \lambda_3}\right)\mathbf{m}'(\mathbf{m}')^T + \sqrt{\lambda_1\lambda_2\lambda_3}\mathbf{I}\right],\end{aligned} \tag{2.34}$$

where $\mathbf{I}$ is the 3 x 3 identity matrix. Now that both $\vec{P}_\Delta$ and $\mathbf{m}_\Delta$ are known, the retardance matrix $\mathbf{M}_R$ can easily be found

$$\mathbf{M}_R = \mathbf{M}_\Delta^{-1}\mathbf{M}', \tag{2.35}$$

and the total retardance R can be written as

$$R = \arccos\left(\frac{Tr\left(\mathbf{M}_R\right)}{2} - 1\right). \tag{2.36}$$

A retardance vector can be constructed as

$$\vec{R} = [1 \quad r_1 \quad r_2 \quad r_3] \qquad \text{with} \qquad r_i = \frac{1}{2\sin R}\sum_{j,k=1}^{3}\epsilon_{ijk}(\mathbf{m}_R)_{jk}, \tag{2.37}$$

where ϵ_{ijk} is the Levi-Cevita permutation symbol. The retardance matrix $\mathbf{M}_R$ is written as a combination of a linear retarder matrix and an optical rotational matrix

$$\begin{aligned}\mathbf{M}_R = &\begin{bmatrix} 1 & 0 & 0 & 0 \\ 0 & \cos^2 2\theta + \sin^2 2\theta\cos\delta & \sin 2\theta\cos 2\theta(1-\cos\delta) & -\sin 2\theta\cos\delta \\ 0 & \sin 2\theta\cos 2\theta(1-\cos\delta) & \sin^2 2\theta + \cos^2 2\theta\cos\delta & \cos 2\theta\sin\delta \\ 0 & \sin 2\theta\cos\delta & -\cos 2\theta\sin\delta & \cos\delta \end{bmatrix} \\ &\times \begin{bmatrix} 1 & 0 & 0 & 0 \\ 0 & \cos 2\psi & \sin 2\psi & 0 \\ 0 & -\sin 2\psi & \cos 2\psi & 0 \\ 0 & 0 & 0 & 1 \end{bmatrix},\end{aligned} \tag{2.38}$$

where δ, θ, and ψ are linear retardance, orientation of the fast axis of the linear retarder, and optical rotation, respectively. The total retardance (2.36) can now be written

$$R = \arccos\left[2\cos^2\psi\cos^2\left(\delta/2\right) - 1\right], \tag{2.39}$$

which in turn lets us write r_3^2 as

$$r_3 = \frac{\sin^2\psi\cos^2\left(\delta/2\right) - 1}{1 - \cos^2\psi\cos^2\left(\delta/2\right)}. \tag{2.40}$$

We now have two equations (2.39) and (2.40) where R and r_3 are both functions of the linear retardance, δ, and optical rotation, ψ, but independent of the orientation of the fast axis, θ. This lets us solve δ and ψ

$$\delta = 2\arccos\left\{\sqrt{r_3^2\left[1 - \cos^2\left(R/2\right)\right] + \cos^2\left(R/2\right)}\right\}, \tag{2.41}$$

$$\psi = \arccos\left[\frac{\cos\left(R/2\right)}{\cos\left(\delta/2\right)}\right], \tag{2.42}$$

and the orientation to the fast axis can then be determined

$$\theta = \frac{1}{2}\arctan\frac{r_3}{r_2}. \tag{2.43}$$

2.6 Nonlinear Optics

The electric displacement mentioned in Section 2.3.2 can be written in a different form

$$\vec{D} = \varepsilon_0\vec{E} + \vec{P}, \tag{2.44}$$

where $\vec{P}$ is the dielectric polarisation

$$\vec{P} = \varepsilon_0\chi\vec{E}, \tag{2.45}$$

describing the electric dipole moment per unit volume inside the material. This fits the classical electron oscillation model, where the electron is visualised as being connected to the nucleus by a spring, driven up and down by the applied electric field. In laser beams, however, the electric field amplitude can be so high that the relation between $\vec{P}$

and $\vec{E}$ can no longer be regarded as linear. A nonlinear term must then be added to Equation (2.45)

$$\vec{P} = \varepsilon_0 \chi \vec{E} + \vec{P}^{NL}, \tag{2.46}$$

where the nonlinear polarisation can be expressed in terms of a power series in the electric field

$$\vec{P}^{NL} = 2\epsilon_0 d\vec{E}^2 + \epsilon_0 \chi^3 \vec{E}^3 + \dots \tag{2.47}$$

This refers to the second order nonlinearity, followed by the third order nonlinearity, etc. Here, d is the nonlinear coefficient and χ is the mediums electric susceptibility, related to the aforementioned permittivity by

$$\varepsilon = \varepsilon_r \varepsilon_0 = (1 + \chi)\varepsilon_0, \tag{2.48}$$

ε_0 being the permittivity in a vacuum, and ε_r, the relative permittivity.

A well known nonlinear effect is the generation of second order harmonics. In 1961, P. A. Franken et. al. showed how a red ruby laser at $694,3$ nm would generate light at $347,2$ nm when transmitted through crystalline quartz [61]. The effect can be understood by considering a monochromatic wave propagating in the z-direction

$$E_\omega(z,t) = \frac{1}{2} E(z,\omega) exp[j(\omega t - k_\omega z)]. \tag{2.49}$$

The relation between the wave number and frequency is given by the inverted propagation speed in the medium

$$k_\omega = \frac{n_\omega \omega}{c}. \tag{2.50}$$

When inserting this expression for E into the second order nonlinearity $P^{NL} = 2\varepsilon_0 d E^2$ this reveals a term oscillating at 2ω

$$P^{NL}_{2\omega} = \frac{\varepsilon_0 d}{2} E^2(z,\omega) exp[j(2\omega t - 2k_\omega z)]. \tag{2.51}$$

The field of the second order harmonic can thus be written

$$E_{2\omega}(z,t) = \frac{1}{2} E(z,2\omega) exp[j(\omega t - k_{2\omega} z)], \tag{2.52}$$

with

$$k_{2\omega} = \frac{n_{2\omega} 2\omega}{c}. \tag{2.53}$$

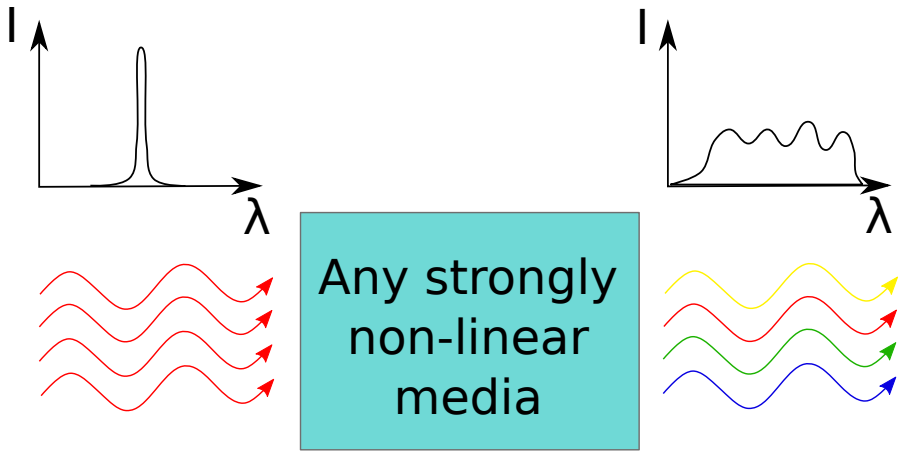

Figure 5: The bandwidth is broadened as the pulse passes through a strongly nonlinear media.

2.6.1 A Supercontinuum Laser Source

A supercontinuum laser is a light source with a broad spectral bandwidth. The most common way to accomplish spectral broadening is by propagation of optical pulses through a strongly nonlinear medium, e.g. by passing an intense ultrashort pulse through a piece of calcite [62]. For pulses with lower energy, an optical fiber can be used. An optical fiber can have a much higher nonlinearity and will ensure good beam quality due to its waveguiding structure.

Photonic Crystal Fibers(PCFs) are optic fibres of special interest [63, 64]. In a general fiber, the waveguiding properties are the result of difference in refractive indices between a solid core and its cladding. In a PCF, however, a uniform refractive index material embedded with microstructured air holes running along the fiber length. The waveguiding properties can be explained by the effective media model, where the area with air holes has a lower effective refractive index than the solid area in the center. PCFs are superior to normal optic fibers in the sense that the number and arrangement of holes can be optimised for any purpose. While a small air-fill fraction and a large core area can result in endless single-mode behaviour, a large air-filled fraction will result in the strong nonlinearity used in supercontinuum generation.

Bandwidth broadening effects are highly dependent on pulse duration from the laser source. Supercontinuum generation using femtosecond pulses are dominated by soliton-related dynamics [65]. For a femtosecond pulsed soliton passing through an optical fiber, the longer wavelengths of the optical spectrum can experience Raman amplification at the expense of power in the shorter wavelengths. The result is a *soliton self-frequency shift*, an overall spectral shift towards longer wavelengths.

For longer pulses in the picosecond to continuous wave regime, there are other effects that dominate.

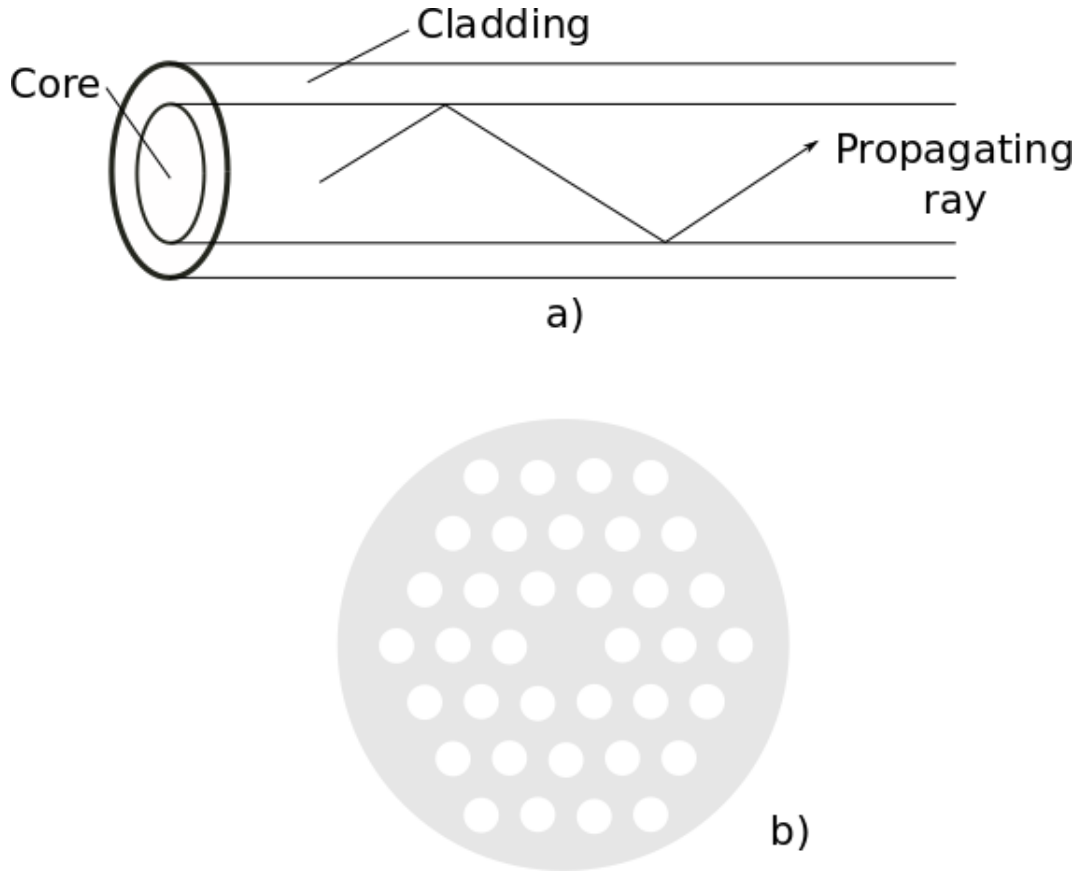

Figure 6: Figure a) exhibits the general concept of a fiber and the guiding of a ray. Figure b) shows a frequently used PCF design. Surrounding the solid center, there is a hexagonal lattice of air holes, resulting in a different effective refractive index in this area.

Four-wave mixing is an effect that arises from the third order nonlinearity in equation (2.47) [66]. It originates from the *Kerr Effect*, an instaneous altering of the refractive index due to density variations caused by the electric field [67]. Four-wave mixing can occur when two or more different frequencies co-propagate in e.g. a fiber. Refractive index modulation at the two distinct frequencies ω_1 and ω_2 will generate two new frequency components, $\omega_3 = 2\omega_1 - \omega_2$ and $\omega_4 = 2\omega_2 - \omega_1$.

Though not as significant as Four-wave Mixing, another important effect in this regime is *Raman scattering* [68]. This is a non-instantaneous response resulting from vibrations in the crystal lattice. The vibrations are caused by optical phonons from the propagating light. As two laser beams with different frequencies pass through a Raman-active medium, the longer wavelength beam, known as the *Stokes Wave*, is amplified at the expense of the shorter wavelength beam. The energy difference is carried away through the lattice as a phonon. An already existing phonon might also interact with the high frequency beam, resulting in photons with even shorter wavelengths, however this effect is usually weak.

While solitons still play a minor role in supercontinuum generation in the picosecond to continuous wave regime, the dominant contributions are from Four-wave Mixing and Raman scattering.

2.6.2 An Acousto-Optic Tunable Filter

There are multiple ways to select the desired frequency from a supercontinuum source. One of them is by applying an acousto-optic tunable filter (AOTF) [69].

Much like in the Kerr effect, acousto-optic modulation alters the refractive index of a crystal by propagating waves. Unlike the Kerr effect, however, it is not electromagnetic waves that cause the change. Instead, a vibrating piezoelectric transducer, driven by a oscillating electric signal, creates sound waves in the crystal. These acoustic waves cause stress perturbations to transverse the material, leading to variation in the refractive index. This allows the AOTF to selectively diffract, through Bragg diffraction, a single narrow-bandpass wavelength from light transmitted through the transparent crystal. The wavelength is controlled by the applied frequency from the transducer.

2.7 Optical Properties of Metals

The interaction between EM waves and a thin metal film can be mathematically described by reviewing the electric displacement (2.44). In a metal, the polarisation is regarded as linear, so the electric displacement is written as

$$\vec{D} = \varepsilon_0 \varepsilon_r \vec{E}. \tag{2.54}$$

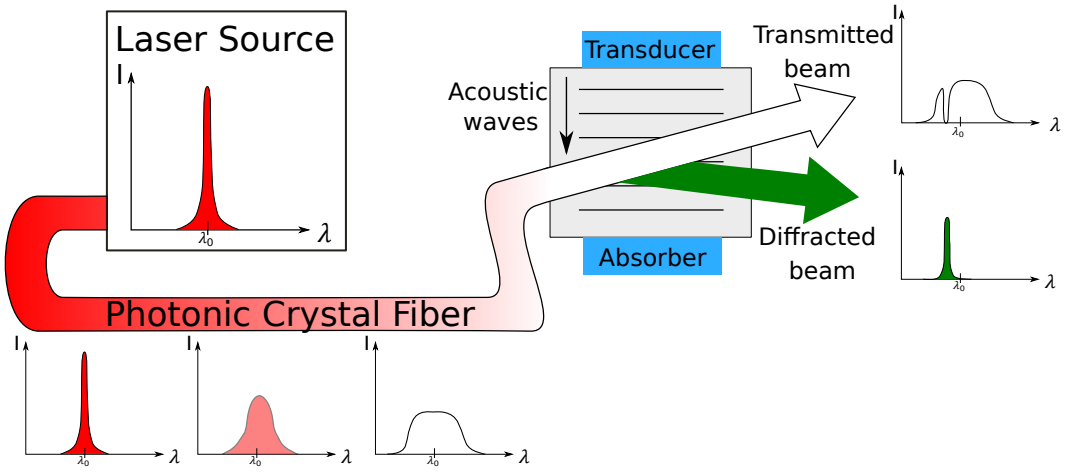

Figure 7: A monochromatic pulse is generated in the laser and broadened in a photonic crystal fiber. The desired wavelength is then diffracted from the AOTF.

The relative permittivity, ε_r, is a wavelength dependent intrinsic property describing the relationship between the applied electric field and the induced displacement field in the metal. Its relation to the refractive index is given by

$$\bar{n} = (n - i\kappa)^2 = \varepsilon_r = \varepsilon_{real} + i\varepsilon_{imaginary}. \tag{2.55}$$

The optical properties of the metal film will now be explained by the use of a plasma model. The free electrons of number density N are regarded as a gas moving against the fixed background of positive ion cores. The electrons move freely, responding to the applied EM field and dampened by a characteristic collision frequency, $\gamma = 1/\tau$. τ is the relaxion time of the free electron gas. The electron-electron interactions and lattice potentials are not taken into account, and there is an energy threshold under which this model is valid. For Au, interband transitions starts to occur around 2.4 eV, making this model only applicable for lower energies.

The movement of electrons subject to an external field, $\vec{E}$, is described by a simple equation of motion

$$m\ddot{\vec{x}} + m\gamma\dot{\vec{x}} = -e\vec{E}, \tag{2.56}$$

where m is the mass of the electron and e the electron charge. For a harmonic time dependent electric field, $\vec{E} = \vec{E}_0 e^{-i\omega t}$, the oscillation of the electron can be written as

$$\vec{x}(\omega) = \frac{e}{m(\omega^2 + i\gamma\omega)}\vec{E}(\omega). \tag{2.57}$$

The displaced electrons contribute to the macroscopic polarisation $\vec{P} = -Ne\vec{x}$, which when inserted into equation 2.57 gives

$$\vec{P}(\omega) = -\frac{Ne^2}{m(\omega^2 + i\gamma\omega)}\vec{E}(\omega). \tag{2.58}$$

The total displacement can thus be written

$$\vec{D}(\omega) = \varepsilon_0 \vec{E}(\omega) + \vec{P}(\omega) = \varepsilon_0 \left(1 - \frac{\omega_p^2}{\omega^2 + i\gamma\omega}\right) \vec{E}(\omega) = \varepsilon_0 \varepsilon_r(\omega) \vec{E}(\omega), \tag{2.59}$$

with $\omega_p = Ne/\varepsilon_0 m$ defined as the plasma frequency and

$$\varepsilon_r(\omega) = 1 - \frac{\omega_p^2}{\omega^2 + i\gamma\omega} \tag{2.60}$$

as the dielectric function of the metal, also known as the Drude model of the optical response of metals.

An expansion to this model is needed for noble metals, such as Au, in the region $\omega > \omega_p$. This is because the filled d-band close to the fermi surface creates a highly polarised environment. The residual polarisation caused by the positive background of the ion cores is described by adding the term $\vec{P}_\infty = \varepsilon_0(\varepsilon_\infty - 1)\vec{E}$ to equation (2.44). This will in turn result in an extra contribution to equation (2.60)

$$\varepsilon_r(\omega) = \varepsilon_\infty - \frac{\omega_p^2}{\omega^2 + i\gamma\omega}, \tag{2.61}$$

a dielectric constant which usually takes on the value $1 \leq \varepsilon_\infty \leq 10$.

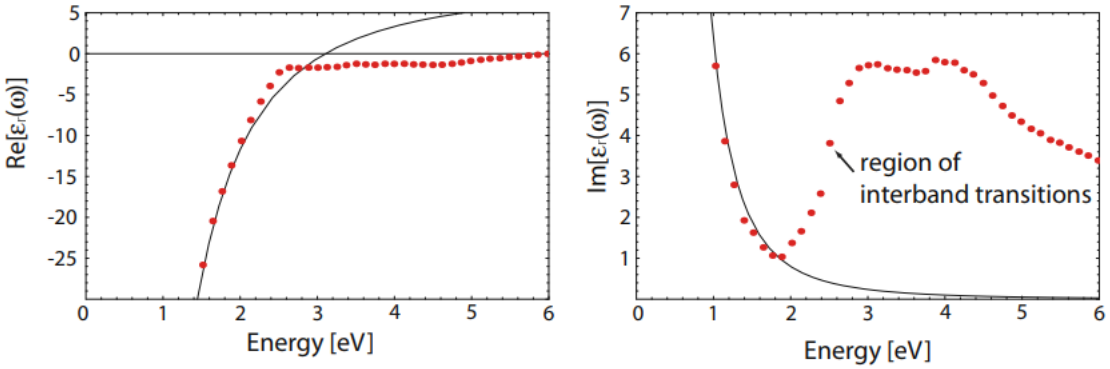

Figure 8: Using Au as an example: the dielectric function $\varepsilon_r(\omega)$ of the free electron gas (solid line) fitted to the literature values of the dielectric data for Au (dots) [70]. Interband transitions limit the validity of this model at visible and higher frequencies, above 2.4 eV.
Credits: Stefan A. Maier [71]

Whilst the validity of the Drude model for Au is compromised at energies exceeding 2.4 eV, alterations to equation (2.58) can be made to produce a model which describes the optical properties at visible frequencies. By discarding the plasma model and using the classical representation of a bound electron with resonance frequency ω_0, a new equation of motion is written

$$m\ddot{\vec{x}} + m\gamma\dot{\vec{x}} + m\omega_0^2\vec{x} = -e\vec{E}. \tag{2.62}$$

Analogous to the Drude model, equation (2.62) is solved for the dielectric function and found to be

$$\varepsilon_r(\omega) = 1 + \frac{\omega_p^2}{\omega_0^2 - \omega^2 - i\gamma\omega}, \tag{2.63}$$

which is the expression of a Lorentz oscillator. A special case of the Lorentz oscillation is the Sellmeier model, where the material is non-absorbing and the collision frequency, γ, is set to 0 [72]. The commonly used Cauchy model is an approximation of the Sellmeier model in terms of the real refractive index, n. Additionally, the Drude model may also be regarded as a special case of the Lorentz model, as they will be identical when $\omega_0 = 0$.

Multiple Lorentz oscillators may be used to model the interband transition, but will not take into account the actual band-gap. The Tauc-Lorentz model, however, does this explicitly. It combines the Lorentz equation (2.62) with an expression developed by Tauc et al. [73] and expanded by Forouhi and Bloomer [74]. The Tauc-Lorentz model describes interband mechanisms with an optical band gap $\hbar\omega_g$, and is written

$$\varepsilon_{imaginary}(\omega) = \frac{A\omega_0\Gamma(\omega - \omega_g)^2}{(\omega^2 - \omega_0^2)^2 - \Gamma^2\omega^2}\frac{1}{\omega}, \tag{2.64}$$

where, A is the amplitude, ω_0 the centre frequency, Γ the broadening frequency, and ω_g the band gap frequency. The equation is only valid for frequencies above the optical band gap; below, it is equal to 0. ε_{real} is obtained by Kramers-Kronig integration.

3 Ellipsometry

Ellipsometry is an optical measurement technique that characterises light reflected from, or transmitted through, a sample. It's key feature is that is that is measures the change in the polarised light, and is therefore also known as *polarimetry*.

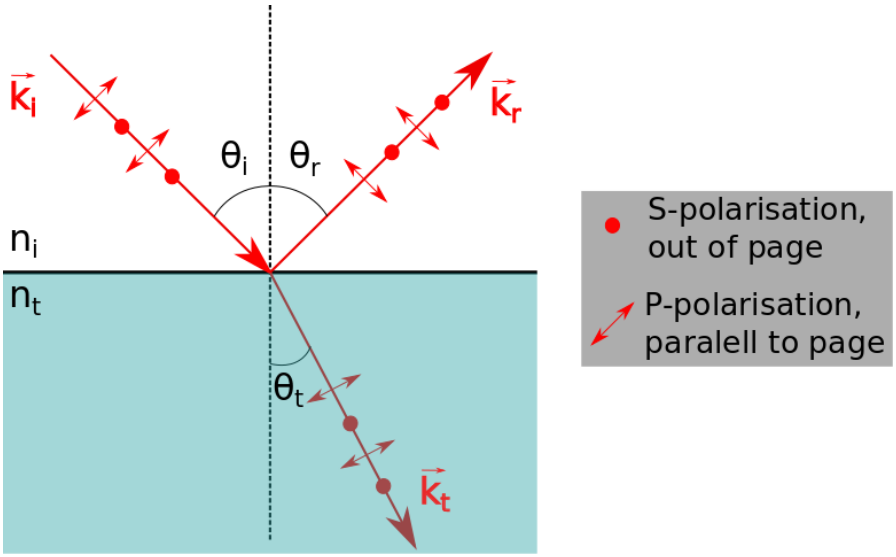

Figure 9: The incident light, $\vec{k}_i$, encountering another material is partially reflected, $\vec{k}_r$, and transmitted, $\vec{k}_t$. Crucial parameters are the angle of incidence, θ_i, the refractive indices, n_i and n_t, and the polarisation of the light. Polarisation is generally defined as either s-polarised (perpendicular to the plane of incidence) or p-polarised (paralell to the plane of incidence).

The underlying physics can be explained by studying the Fresnel equations for EM waves incident on an interface between different optical media. The E_p- and E_s-field components reflected or transmitted will be altered independently with respect to the incoming components. Using Jones formalism, one writes

$$\begin{bmatrix} E_{rp} \\ E_{rs} \end{bmatrix} = \begin{bmatrix} r_{pp} & r_{ps} \\ r_{sp} & r_{ss} \end{bmatrix} \cdot \begin{bmatrix} E_{ip} \\ E_{is} \end{bmatrix} \qquad \text{and} \qquad \begin{bmatrix} E_{tp} \\ E_{ts} \end{bmatrix} = \begin{bmatrix} t_{pp} & t_{ps} \\ t_{sp} & t_{ss} \end{bmatrix} \cdot \begin{bmatrix} E_{ip} \\ E_{is} \end{bmatrix} \tag{3.1}$$

for reflected and transmitted light, respectively. For an isotropic sample, the diagonal matrix elements are given by the Fresnel equations [75]

$$\begin{aligned} r_{pp} &= \frac{E_{rp}}{E_{ip}} = \frac{n_t \cos\theta_i - n_i \cos\theta_t}{n_t \cos\theta_i + n_i \cos\theta_t}, & r_{ss} &= \frac{E_{rs}}{E_{is}} = \frac{n_i \cos\theta_i - n_t \cos\theta_t}{n_i \cos\theta_i + n_t \cos\theta_t}, \\ t_{pp} &= \frac{E_{tp}}{E_{ip}} = \frac{2n_i \cos\theta_i}{n_t \cos\theta_i + n_i \cos\theta_t}, & t_{ss} &= \frac{E_{ts}}{E_{is}} = \frac{2n_i \cos\theta_i}{n_i \cos\theta_i + n_t \cos\theta_t}. \end{aligned} \tag{3.2}$$

The off-diagonal elements are the coupling modes between the two orthogonal fields, where t_{sp} is the transmitted s-polarised light induced by the incoming p-polarised light, and so on.

For an isotropic sample there is no coupling between the orthogonal fields, so the off-diagonal elements all equals zero. The change in polarisation can be described by a complex ratio

$$\rho_{pp} = \frac{r_{pp}}{r_{ss}} = \frac{t_{pp}}{t_{ss}} = \tan\Psi_{pp} e^{i\Delta_{pp}}, \tag{3.3}$$

where Ψ is the relative change in amplitude and Δ the change in phase, δ, known from equation (2.12). Ψ and Δ are the parameters measured in standard ellipsometry.

Anisotropic samples complicate the matter, since the off-diagonal elements from equation (3.1) are no longer zero. Two more complex ratios must then be measured to explain the change in polarisation

$$\rho_{ps} = \frac{r_{ps}}{r_{ss}} = \frac{t_{ps}}{t_{ss}} = \tan\Psi_{ps} e^{i\Delta ps} \qquad \text{and} \qquad \rho_{sp} = \frac{r_{sp}}{r_{ss}} = \frac{t_{sp}}{t_{ss}} = \tan\Psi_{sp} e^{i\Delta sp}. \tag{3.4}$$

Measurements of these properties are known as generalised ellipsometry.

3.1 Mueller Matrix Ellipsometry

In Mueller matrix ellipsometry, all of the 4x4 matrix elements of a sample are measured. Combining equation (2.20) with the reflecting Jones matrix from equation (3.1), the resulting reflection Mueller matrix is written

$$\mathbf{M}_{anisotropic} = \begin{bmatrix} \frac{1}{2}(|r_{pp}|^2 + |r_{sp}|^2 + |r_{ps}|^2 + |r_{ss}|^2) & \frac{1}{2}(|r_{pp}|^2 + |r_{sp}|^2 - |r_{ps}|^2 - |r_{ss}|^2) \\ \frac{1}{2}(|r_{pp}|^2 - |r_{sp}|^2 + |r_{ps}|^2 - |r_{ss}|^2) & \frac{1}{2}(|r_{pp}|^2 - |r_{sp}|^2 - |r_{ps}|^2 + |r_{ss}|^2) \\ Re(r_{pp}r_{sp}^* + r_{ps}r_{ss}^*) & Re(r_{pp}r_{sp}^* - r_{sp}r_{ss}^*) \\ -Im(r_{pp}r_{sp}^* + r_{ps}r_{ss}^*) & -Im(r_{pp}r_{sp}^* - r_{ps}r_{ss}^*) \end{bmatrix}$$
$$\begin{bmatrix} Re(r_{pp}r_{ps}^* + r_{sp}r_{ss}^*) & Im(r_{pp}r_{ps}^* + r_{sp}r_{ss}^*) \\ Re(r_{pp}r_{ps}^* - r_{sp}r_{ss}^*) & Im(r_{pp}r_{ps}^* - r_{sp}r_{ss}^*) \\ Re(r_{pp}r_{ss}^* + r_{ps}r_{sp}^*) & Im(r_{pp}r_{ss}^* - r_{ps}r_{sp}^*) \\ -Im(r_{pp}r_{ss}^* + r_{ps}r_{sp}^*) & Re(r_{pp}r_{ss}^* + r_{ps}r_{sp}^*) \end{bmatrix}. \tag{3.5}$$

For an isotropic, non-depolarising surface where $r_{sp} = r_{ps} = 0$, this can be simplified and rewritten as

$$\mathbf{M}_{isotropic} = \frac{|r_{pp}|^2 + |r_{ss}|^2}{2} \begin{bmatrix} 1 & -\cos 2\Psi & 0 & 0 \\ -\cos 2\Psi & 0 & 0 & 0 \\ 0 & 0 & \sin 2\Psi \cos \Delta & \sin 2\Psi \sin \Delta \\ 0 & 0 & -\sin 2\Psi \sin \Delta & \sin 2\Psi \cos \Delta \end{bmatrix}, \quad (3.6)$$

and one can introduce the N,S,C parameters

$$N = \cos 2\Psi, \quad (3.7a)$$
$$C = \sin 2\Psi, \quad (3.7b)$$
$$S = \sin 2\Psi \sin \Delta, \quad (3.7c)$$

as the non-zero elements; N=m_{12}=m_{21}, C=m_{33}=m_{44}, and S=m_{34}=-m_{43}.

3.2 Construction of a Mueller Matrix Ellipsometer

A Mueller matrix ellipsometer consists of five basic parts: a light source, a Polarisation State Generator (PSG), a sample, a Polarisation State Analyser (PSA), and a detector. The PSG is used to set appropriate polarisation states, while the PSA analyses the polarisation states altered by the sample. A minimum of four intensity measurements are required to determine a single Stokes vector [76]. To find the complete Mueller matrix, at least four polarisation states are required for each Stokes vector measurement [27].

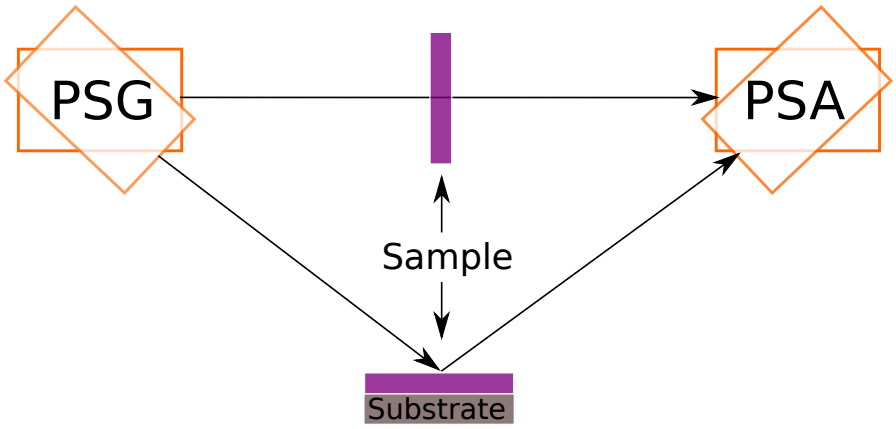

Figure 10: Light exiting from the polarisation state generator is transmitted through- or reflected in a sample before passing through the polarisation state analyser.

The general idea of a Mueller matrix ellipsometer is to determine the Mueller matrix of the sample **M** from the collected intensity matrix **B**, and the system's generating and

analysing matrices $\mathbf{W}$ (PSG) and $\mathbf{A}$ (PSA). In accordance with (2.19) one writes

$$\mathbf{B} = \mathbf{AMW}, \tag{3.8}$$

and by inverting the matrices $\mathbf{A}$ and $\mathbf{W}$, $\mathbf{M}$ is found

$$\mathbf{M} = \mathbf{A}^{-1}\mathbf{B}\mathbf{W}^{-1}. \tag{3.9}$$

The matrices $\mathbf{W}$ and $\mathbf{A}$ are constructed from a set of probing Stokes vectors, $\vec{w}_i$, and analysing states, $\vec{a}_j$. Each of the probing Stokes vectors can be found by multiplying the polarisation state generator's matrix with the Stokes vector of the incoming unpolarised light

$$\vec{w}_i = \mathbf{W}_{PSG_i} \cdot \vec{S}_{unpol}, \tag{3.10}$$

where $\vec{S}_{unpol} = [1, 0, 0, 0]^T$. The result is a matrix $\mathbf{W}$ of n probing states given by

$$\mathbf{W} = [\vec{w}_1, \vec{w}_2, ..., \vec{w}_n]. \tag{3.11}$$

Similarly, $\mathbf{A}$ can be defined as

$$\mathbf{A} = \begin{bmatrix} \vec{a}_1 \\ \vec{a}_2 \\ \vdots \\ \vec{a}_m \end{bmatrix}, \tag{3.12}$$

where each analysing state is written

$$\vec{a}_j = [1, 0, 0, 0] \cdot \mathbf{M}_{PSA_j}. \tag{3.13}$$

If at least four probing and analysing states are present, each element $b_{i,j}$ can be measured, to obtain the Mueller matrix $\mathbf{M}$ of the sample. In cases where the ellipsometer generates more than four states in the PSG and PSA, the two matrices $\mathbf{W}$ and $\mathbf{A}$ are no longer square 4-by-4 matrices, resulting in a so-called *overdetermined* system [41]. In general, non-square matrices are singular, meaning they do not have an inverse, and equation (3.9) is thus invalid. By introducing the Moore-Penrose pseudo-inverse, however, cases where $m, n \geqslant 4$ can be solved as

$$\mathbf{M} = \mathbf{A}^{\dagger}\mathbf{B}\mathbf{W}^{\dagger}, \tag{3.14}$$

where † is the Moore-Penrose pseudo-inverse. The relative error of the Mueller matrix $\mathbf{M}$ is

$$\frac{||\Delta\mathbf{M}||}{||\mathbf{M}||} \lesssim \kappa_A \frac{||\Delta\mathbf{A}||}{||\mathbf{A}||} + \kappa_W \frac{||\Delta\mathbf{W}||}{||\mathbf{W}||} + \kappa_W \kappa_A \frac{||\Delta\mathbf{B}||}{||\mathbf{B}||}, \tag{3.15}$$

where $\frac{||\Delta\mathbf{A}||}{||\mathbf{A}||}$ and $\frac{||\Delta\mathbf{W}||}{||\mathbf{W}||}$ are relative calibration errors and $\frac{||\Delta\mathbf{B}||}{||\mathbf{B}||}$ is the measurement noise [77]. κ_W and κ_A are the corresponding condition numbers for the matrices $\mathbf{W}$ and $\mathbf{A}$. The condition number is defined by the matrix norm

$$\kappa_W = ||\mathbf{W}||||\mathbf{W}^{-1}||, \tag{3.16}$$

where $||\mathbf{W}||$ represents the second norm, or euclidean norm of $\mathbf{W}$, generally defined as [78]

$$||\mathbf{W}|| = \sup_{\vec{x}\neq\vec{0}} \frac{||\mathbf{W}\vec{x}||}{||\vec{x}||} = \max_{||\vec{x}||=1} ||\mathbf{W}\vec{x}||, \quad \mathbf{W} \in \mathbb{R}^{m\times n}, \quad \vec{x} \in \mathbb{R}^n. \tag{3.17}$$

A good polarimeter with small errors requires low condition numbers. The lowest possible condition number for a matrix constructed from four Stokes vectors is $\kappa = \sqrt{3}$ [79], which is therefore also the lowest possible condition number for $\mathbf{W}$ and $\mathbf{A}$.

3.3 The Eigenvalue Calibration Method

The eigenvalue calibration method (ECM) suggested by Compain et al. [80] is a technique to determine the system matrices $\mathbf{W}$ and $\mathbf{A}$ in a Mueller matrix ellipsometer. The method requires a set of suitable calibration samples $\{\mathbf{M}\}$ with properties sufficiently different to one another. The system matrices are uniquely determined through matrix algebra performed on the measurements of these known samples.

From the set of reference samples $\{\mathbf{M}\}$ there is a corresponding set of intensity matrices $\{\mathbf{B}\}$ given by equation (2.19). By choosing air as reference sample $\mathbf{M}_0$, the corresponding intensity matrix is simply $\mathbf{B}_0 = \mathbf{AW}$ since the mueller matrix of air is equal to the identity matrix $\mathbf{I}_{4x4}$. Two sets of matrices $\{\mathbf{C}^W\}$ and $\{\mathbf{C}^A\}$ can then be constructed as

$$\begin{aligned} \mathbf{C}_i^W &= \mathbf{B}_0^\dagger \mathbf{B}_i = (\mathbf{AW})^\dagger \mathbf{A}\mathbf{M}_i\mathbf{W} = \mathbf{W}^\dagger\mathbf{M}\mathbf{W}, \\ \mathbf{C}_i^A &= \mathbf{B}_i \mathbf{B}_0^\dagger = \mathbf{A}\mathbf{M}_i\mathbf{W}(\mathbf{AW})^\dagger = \mathbf{AMA}^\dagger, \end{aligned} \tag{3.18}$$

where $\mathbf{C}_i^W$ and $\mathbf{C}_i^A$ are independent of $\mathbf{W}$ and $\mathbf{A}$, respectively. In the special case where $n = 4$, $\{\mathbf{C}^W\}$ and $\{\mathbf{C}^A\}$ are, with the except of some random measurement noise, similar to $\{\mathbf{M}_i\}$ and thus share the same eigenvalues.

A general non-depolarising Mueller matrix with both diattenuation and retardance is written

$$\mathbf{R}(\tau, \Psi, \Delta) = \tau \begin{bmatrix} 1 & -cos(2\Psi) & 0 & 0 \\ -cos(2\Psi) & 1 & 0 & 0 \\ 0 & 0 & sin(2\Psi)cos(\Delta) & sin(2\Psi)cos(\Delta) \\ 0 & 0 & -sin(2\Psi)cos(\Delta) & sin(2\Psi)cos(\Delta) \end{bmatrix}, \tag{3.19}$$

where τ is the transmission coefficient, and Ψ and Δ are the ellipsometry angles. This matrix has two real and two complex eigenvalues

$$\begin{aligned} \lambda_{r1} &= \tau sin^2(\Psi), & \lambda_{r2} &= 2\tau sin^2(\Psi) \\ \lambda_{c1} &= \tau sin^2(2\Psi)e^{-i\Delta}, & \lambda_{c2} &= \tau sin^2(2\Psi)e^{i\Delta}, \end{aligned} \tag{3.20}$$

where the subscripts r and c represent real and complex values, respectively. The theoretical eigenvalues of $\mathbf{M}_i$ can now be associated with the eigenvalues of $\mathbf{C}_i^W$ and $\mathbf{C}_i^A$,

allowing the reconstruction of each Mueller matrix calibration sample as

$$\begin{aligned} \tau_{pol} &= Tr(\mathbf{c}_{pol}), \qquad \tau_{ret} = \frac{1}{2}\left(\lambda_{r1} + \lambda r2\right), \\ \Delta &= \frac{1}{2}\arg\left(\frac{\lambda_{c1}}{\lambda_{c2}}\right), \quad \Psi = \arctan\left(\sqrt{\frac{\lambda_{r1}}{\lambda_{r2}}}\right). \end{aligned} \tag{3.21}$$

In principal, when $n > 4$ and no noise is present, one can find the four eigenvalues of $\mathbf{C}_i^W$ and $\mathbf{C}_i^A$ corresponding to the eigenvalues of $\mathbf{M}_i$ by comparison to what is anticipated for that certain reference sample. The presence of noise, however, make this difficult. A solution is to calculate the 4x4 matrices $\mathbf{C}_i'^W$ and $\mathbf{C}_i'^A$ from the 4x4 subsets of $\mathbf{B}_0$ and $\mathbf{B}_i$ which give the lowest condition number in $\mathbf{B}_0$ [81].

The orientation of the reference samples are not directly given by the eigenvalues of $\{\mathbf{C}^W\}$ and $\{\mathbf{C}^A\}$, but can be found through the calculations of the system matrices $\{\mathbf{W}\}$ and $\{\mathbf{A}\}$. To do this, one first writes equation (3.18) as

$$\begin{aligned} \mathbf{M}_i\mathbf{W} - \mathbf{W}\mathbf{C}_i^W &= 0, \\ \mathbf{A}\mathbf{M}_i - \mathbf{C}_i^A\mathbf{A} &= 0. \end{aligned} \tag{3.22}$$

Defining $\vec{w}$ and $\vec{a}$ as $\mathbf{W}$ and $\mathbf{A}$ in vector form, equation (3.22) is by linear transformation rewritten as

$$\begin{aligned} \mathbf{H}_i^W \vec{w}^{4n} &= 0, \\ \mathbf{H}_i^A \vec{a}^{4n} &= 0. \end{aligned} \tag{3.23}$$

$\mathbf{H}_i^W$ and $\mathbf{H}_i^A$ are matrices of size $4n \times 4n$

$$\begin{aligned} \mathbf{H}_i^W &= [\vec{g}_i^{W1} \quad \vec{g}_i^{W2} \ldots \vec{g}_i^{W4n}], \\ \mathbf{H}_i^A &= [\vec{g}_i^{A1} \quad \vec{g}_i^{A2} \ldots \vec{g}_i^{A4n}], \end{aligned} \tag{3.24}$$

and the $\vec{g}_i^W$ and $\vec{g}_i^A$ vectors are constructed from the matrices $\mathbf{G}_i^W$ and $\mathbf{G}_i^A$

$$\begin{aligned} \mathbf{G}_i^{W1} = \mathbf{M}_i\mathbf{U}_1^W - \mathbf{U}_1^w\mathbf{C}_i^W \quad \ldots \quad \mathbf{G}_i^{W4n} &= \mathbf{M}_i\mathbf{U}_{4n}^W - \mathbf{U}_{4n}^W\mathbf{C}_i^W \\ \mathbf{G}_i^{A1} = \mathbf{M}_i\mathbf{U}_1^A - \mathbf{U}_1^A\mathbf{C}_i^A \quad \ldots \quad \mathbf{G}_i^{A4n} &= \mathbf{M}_i\mathbf{U}_{4n}^A - \mathbf{U}_{4n}^A\mathbf{C}_i^A, \end{aligned} \tag{3.25}$$

where

$$\{\mathbf{U}^W\} = \left\{ \mathbf{U}_1^W = \begin{bmatrix} 1 & 0 & \ldots & 0 \\ 0 & 0 & \ldots & 0 \\ 0 & 0 & \ldots & 0 \\ 0 & 0 & \ldots & 0 \end{bmatrix}, \mathbf{U}_2^W = \begin{bmatrix} 0 & 1 & \ldots & 0 \\ 0 & 0 & \ldots & 0 \\ 0 & 0 & \ldots & 0 \\ 0 & 0 & \ldots & 0 \end{bmatrix}, \ldots, \mathbf{U}_{4n}^W = \begin{bmatrix} 0 & 0 & \ldots & 0 \\ 0 & 0 & \ldots & 0 \\ 0 & 0 & \ldots & 0 \\ 0 & 0 & \ldots & 1 \end{bmatrix} \right\}, \tag{3.26}$$

and

$$\{\mathbf{U}^A\} = \left\{ \mathbf{U}_1^A = \begin{bmatrix} 1 & 0 & 0 & 0 \\ 0 & 0 & 0 & 0 \\ \vdots & \vdots & \vdots & \vdots \\ 0 & 0 & 0 & 0 \end{bmatrix}, \mathbf{U}_2^A = \begin{bmatrix} 0 & 1 & 0 & 0 \\ 0 & 0 & 0 & 0 \\ \vdots & \vdots & \vdots & \vdots \\ 0 & 0 & 0 & 0 \end{bmatrix}, \ldots, \mathbf{U}_{4n}^A = \begin{bmatrix} 0 & 0 & 0 & 0 \\ 0 & 0 & 0 & 0 \\ \vdots & \vdots & \vdots & \vdots \\ 0 & 0 & 0 & 1 \end{bmatrix} \right\}. \tag{3.27}$$

One can now construct a total measurement matrix for all reference samples i

$$\begin{aligned} \mathbf{K}^W &= \sum_{i=1}^{n} (\mathbf{H}_i^W)^T \mathbf{H}_i^W, \\ \mathbf{K}^A &= \sum_{i=1}^{n} (\mathbf{H}_i^A)^T \mathbf{H}_i^A, \end{aligned} \tag{3.28}$$

and then find the over-determined solution to the system by solving the equation

$$\begin{aligned} \mathbf{K}^W \vec{w} &= 0, \\ \mathbf{K}^A \vec{a} &= 0. \end{aligned} \tag{3.29}$$

The matrices in equation (3.28) are positive semi-definite symmetric real matrices, meaning they have only non-negative eigenvalues and can be diagonalised. In theory these matrices will have 1 zero and 15 non-zero eigenvalues, due to the unique solutions of $\mathbf{W}$ and $\mathbf{A}$ from equation (3.29). With real measurements, however, some noise will be present and a good approximation is found by sorting the eigenvalues

$$\begin{aligned} \lambda_1^W > \lambda_2^W > \cdots > \lambda_{4n}^W \gtrsim 0, \\ \lambda_1^A > \lambda_2^A > \cdots > \lambda_{4n}^A \gtrsim 0, \end{aligned} \tag{3.30}$$

then choosing the eigenvalues corresponding to λ_{4n}^W and λ_{4n}^A.

Since the orientation of the calibration samples cannot be determined from the matrix eigenvalues, a θ-dependency is introduced for the unknown calibration sample orientations by

$$\mathbf{M}_i'(\theta_i) = \mathbf{R}(-\theta_i)\mathbf{M}_i\mathbf{R}(\theta_i), \tag{3.31}$$

inducing a θ-dependency in $\mathbf{K}$, $\mathbf{K}^W$=$\mathbf{K}^W(\theta_1, \ldots, \theta_j)$ and $\mathbf{K}^A$=$\mathbf{K}^A(\theta_1, \ldots, \theta_j)$. By minimising the ration between the smallest eigenvalue and the sum of the other eigenvalues, the angles can be determined through

$$\epsilon_W = \frac{\lambda_{4n}^W}{\sum_{i=1}^{4n-1} \lambda_i^W} \qquad \text{and} \qquad \epsilon_A = \frac{\lambda_{4n}^A}{\sum_{i=1}^{4n-1} \lambda_i^A}. \tag{3.32}$$

3.3.1 A Ferroelectric Liquid Crystal Based Bulk-MME System

Liquid crystals (LCs) are matter in a state which has properties between those of conventional liquids and those of solid crystals. Ferroelectric liquid crystals [82] (FLCs) are liquid crystals in a smectic C phase where long molecules are arranged in layers, and the orientation is in the same direction within each layer. The direction of the molecules is controlled by the dipole moment induced by the chirality of the molecules. By switching the polarity of an external electric field, the molecules change their direction, and thus the orientation of the LCs effective fast axis. FLCs can operate as both waveplates and

as normal phase retarders, where the retardance is proportional to the thickness of the optical component.

Due to the stable voltage controlled azimuth orientation, an FLC will have two stable states. To generate four probing and analysing states, the PSG and PSA will require two FLCs each

PSG	FLC1	FLC2
State 1	0	0
State 2	1	0
State 3	0	1
State 4	1	1

PSA	FLC3	FLC4
State 1	0	0
State 2	1	0
State 3	0	1
State 4	1	1

The custom built system developed by Hagen [83] consists of a symmetric generator and analyser, both composed of a polariser, two fixed waveplates, and two ferroelectric liquid crystals. The Mueller matrix of the PSG is a product of the Mueller matrix of each component

$$\mathbf{M}_{FLC_{PSG}} = \mathbf{M}_{ret}(\theta_{FLC_2}, \Delta_{FLC_2})\mathbf{M}_{ret}(\theta_{W_2}, \Delta_{W_2})\mathbf{M}_{ret}(\theta_{FLC_1}, \Delta_{FLC_1}) \\ \mathbf{M}_{ret}(\theta_{W_1}, \Delta_{W_1})\mathbf{M}_{pol}, \tag{3.33}$$

where the rotation of the matrices (equation (2.22)) has been included in $\mathbf{M}_{ret}$. Similarly one gets

$$\mathbf{M}_{FLC_{PSA}} = \mathbf{M}_{pol}\mathbf{M}_{ret}(\theta_{W_4}, \Delta_{W_4})\mathbf{M}_{ret}(\theta_{FLC_4}, \Delta_{FLC_4})\mathbf{M}_{ret}(\theta_{W_3}, \Delta_{W_3}) \\ \mathbf{M}_{ret}(\theta_{FLC_3}, \Delta_{FLC_3}) \tag{3.34}$$

for the PSA matrix. When switching between the two stable states of each FLC, variation in the angles $\theta_{FLC_1}, \theta_{FLC_2}, \theta_{FLC_3}, \theta_{FLC_4}$, resulting in $2^4 = 16$ different combined generating and analysing polarisation states.

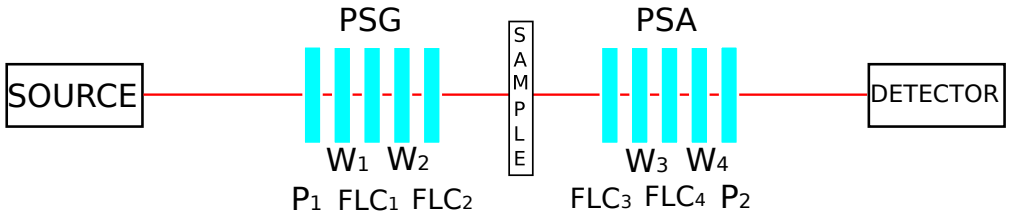

Figure 11: The optical components of the FLC setup. Source, polariser (P_i), fixed waveplate (W_i), and ferroelectric liquid crystal (FLC_i).

4 Beam Splitting Metasurfaces

In contrast to the relatively big and electricity dependent bulk-MME systems, beam splitting metasurfaces can be made microscopic in size and are electricity independent. This makes them a hot topic for ellipsometry performed in space, for *in-vivo* purposes, and many other applications.

4.1 Concept

A *Blazed Grating* is a special type of *Diffraction Grating*. Its purpose is to achieve reflection of maximum optical power in a desired diffraction order, while suppressing the other orders (especially the zeroth order). A blazed grating has a sawtooth shape where the periodicity and the blazed angle are optimised for diffraction of a certain wavelength.

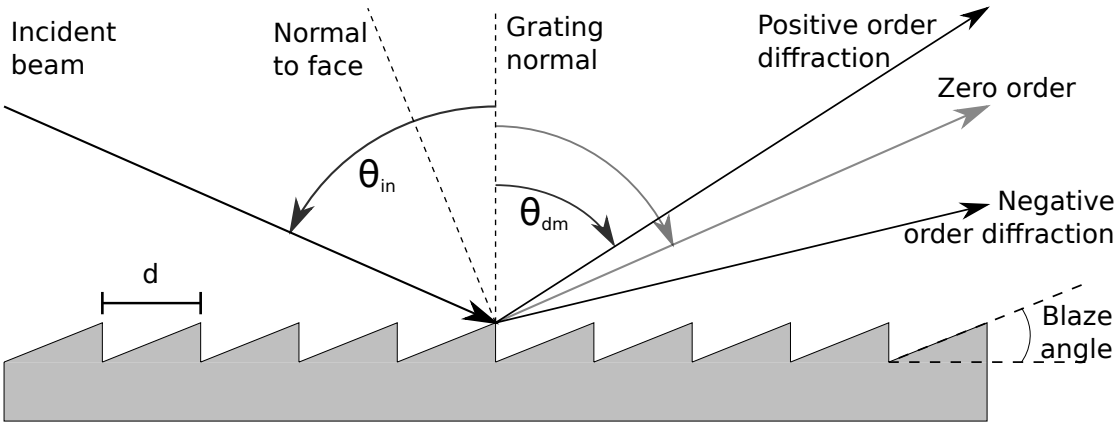

Figure 12: A blazed grating where the zeroth order reflection is suppressed.

In 2013, Pors et al. [39] suggested a new design for beam splitting of orthogonal polarisations. By structuring a periodic arrangement of metal nanobricks with only two degrees of freedom, the reflection of the two normal incidence polarisations could be controlled independently.

Light reflected from a structured metasurface will, in accordance with the laws of diffraction, undergo a phase change. If one can control these orthogonal phase changes independently, the TE and TM waves can be separated into individual orders, and one has succeeded in making a beam splitting metasurface. Pors et. al. discovered that near the gap surface plasmon resonance, this could be achieved with only two degrees of freedom; namely the length and width, L_x and L_y, of the structured boxes.

A surface reflecting orthogonal polarisations in opposite diffraction orders can be regarded as a blazed grating where the blaze angle has opposite signs for the two polari-

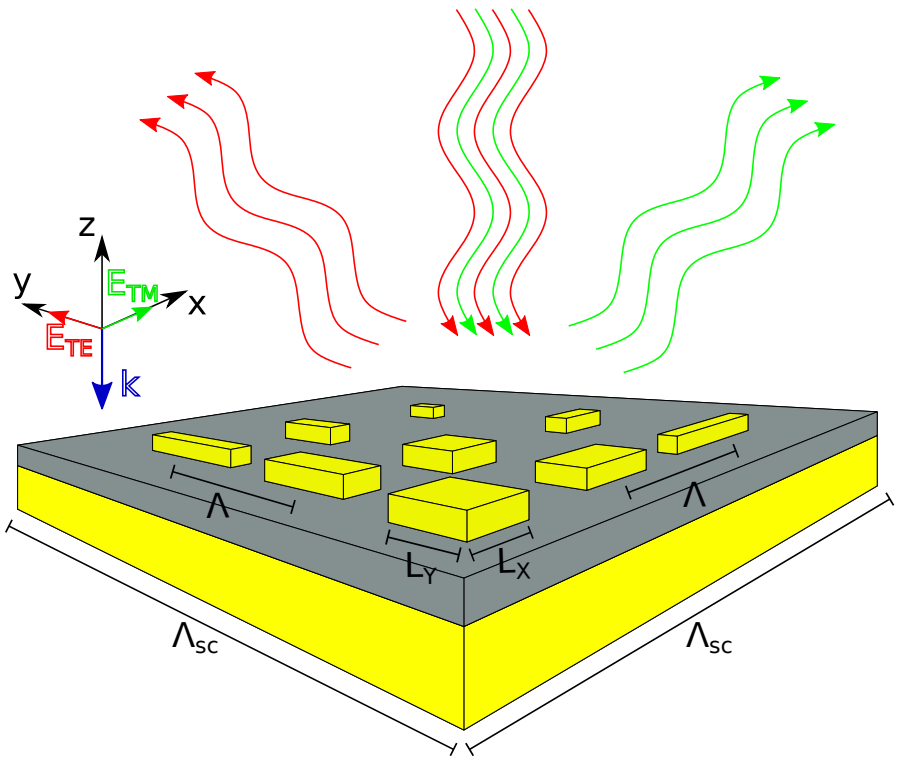

Figure 13: A metasurface with boxes of length and width L_x and L_y, evenly spaced with a center distance of Λ and periodicity Λ_{sc}

sations. The goal is to implement the reflection coefficient

$$r(x) = |r|e^{\pm i\phi} = |r|e^{\pm i2\pi x/\Lambda_{sc}},$$

where $|r|$ is the reflection coefficient, x the spatial coordinate, Λ_{sc} the super cell grating periodicity, and where the sign of the phase gradient depends on the polarisation. Studying the diagonal arrangement of circle-marked shapes in Figure 14a one observes an increasing phase gradient for the TM mode and a decreasing phase gradient for the TE mode. This corresponding arrangement of nano bricks is shown in Figure 14b and will behave as a grating where $r(x + \Lambda_{sc}) = r(x)$ and TM and TE modes are reflected in opposite directions. The x-marked shapes from Figure 14a show an increase in the phase gradient of the TM mode, but TE phase gradient is constant. The TE mode will thus experience a "flat" surface and be reflected back into the zeroth mode, while the TM mode will act as though reflected from a blazed grating.

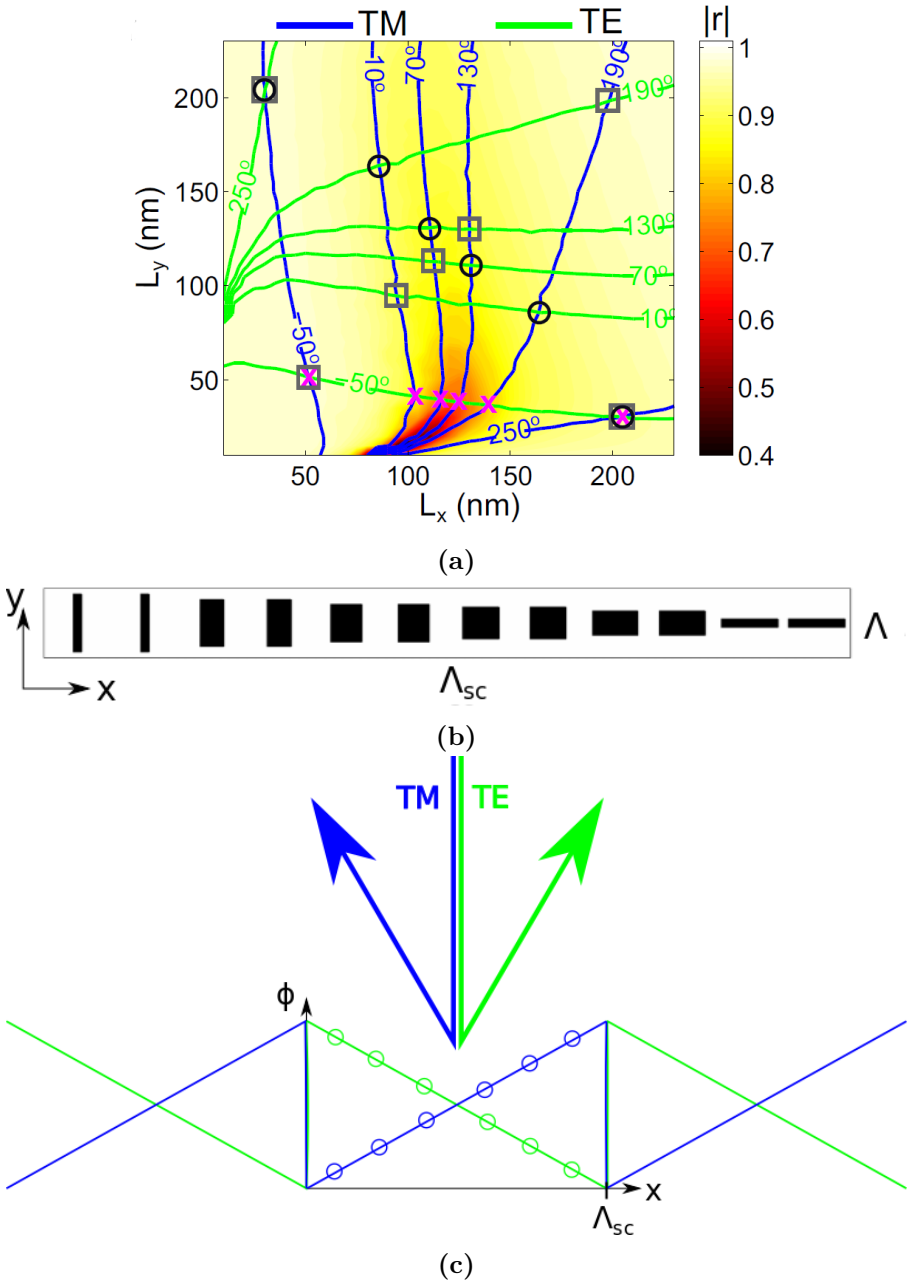

Figure 14: Figure (a) shows the calculated reflection coefficient, r, as a function of nanobrick widths for $\Lambda = 240nm$. The nanobrick height was 50 nm, and the wavelength 800 nm. The colour map shows the reflection coefficient $|r|$ for TM polarisation, while the blue and green lines are the contours of the reflection phase for TM and TE polarisations, respectively. Figure (b) shows the box arrangement for reflection in $m = \pm 1$ with a center distance Λ and periodicity Λ_{sc}. Figure (c) shows how the nanostructured pattern from Figure (b) will result in an increasing (decreasing) phase gradient for the TM (TE) mode.
Credits: Pors et. al.

4.2 Production of Multilayered Films

A vital element in the creation of beam splitting meta surfaces is a high quality multilayered thin film with well known optical properties. After a thin film has been created, its optical properties and surface must be investigated to confirm sufficient quality before the structuring process is initiated.

Composition of Multilayered Film and Preparation of Substrate

The multilayered film consists of a 100 nm thick layer of gold (Au), 40 nm of silicon-oxide (SiO_2), and a 40 nm top layer of Au. Between each layer there is a 2 nm titanium binding layer. The substrate is a silicon wafer chosen due to its close to non-existent surface roughness. The bottom Au layer should be opaque, and 100 nm is considered sufficient.

2" Si wafers of 250 μm thickness were skribed into smaller pieces to make them fit the different characterisation tools. They were cleaned with acetone in an ultrasonic bath, rinsed with ispropanol, and blown dry with nitrogen. Once clean, the substrates were loaded into the AJA Sputter and Evaporator, a tool utilised to make thin films. This is a *Custom ATC-2200V* from AJA International Inc., which can be employed for both sputtering and electron beam evaporation. The AJA has a plasma cleaning function, so all substrates were plasma cleaned for about 3 minutes before deposition was initiated.

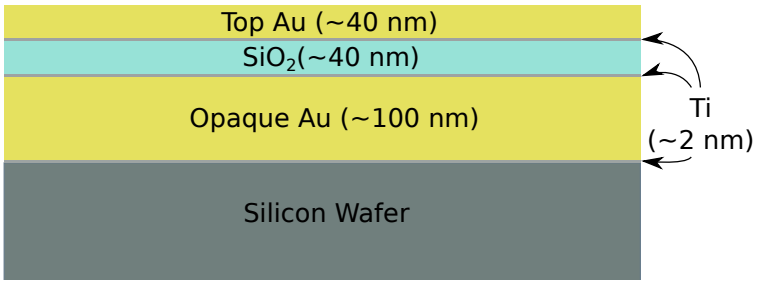

Figure 15: The different components of the multilayered thin film.

Sputtering

Sputtering is a technique used to deposit a thin film of a material onto a substrate. A gas, in this case argon, is metered into a pre-pumped vacuum chamber until the chamber pressure reaches a specific level. By introducing a live electrode into this environment, gaseous plasma is obtained. Ions from this plasma are accelerated onto the desired source material, eroding it by energy transfer from the ions. Neutral particles - either individual atoms, clusters of atoms, or molecules - are ejected from the source material in a straight line and will continue to do so until they come into contact with an obstacle.

By placing the substrate in the path of these ejected particles, it will be coated by a thin film of the source material. This technique was used to deposit SiO_2, with an expected deposition rate of 0.4 Å/s.

Electron Beam Evaporation

Electron beam (E-beam) evaporation is a physical vapor deposition (PVD) technique whereby an intense electron beam strikes a source material, vaporising it within a vacuum environment. As the surface atoms receive enough energy to leave the source material, they will traverse the vacuum chamber and hit the substrate positioned above the evaporating material. Both Au and Ti were deposited by evaporation with an expected deposition rate of 5.0 Å/s.

Spitting is an error that might occur during e-beam evaporation, and is illustrated in Figure 16. Spitting is caused when liquid droplets from the source material fasten on the substrate creating relatively large spheres on the surface. It can be caused by the quality of the source material, the choice of crucible in which the source material is contained, or the power from the electron beam. Few, if any, of these are settings easily controlled by the user.

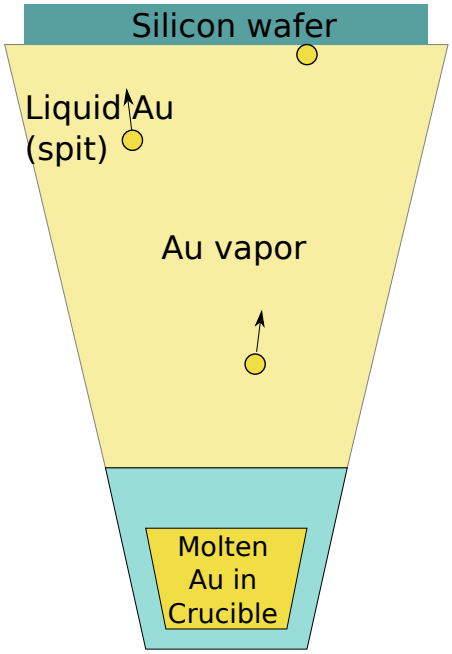

Figure 16: A simple sketch of how spitting might occur when Au is being deposited onto a Si substrate. The liquid droplets will form solid spheres on the substrate surface.

4.3 Thin Film Ellipsometer Measurement and Analysis

In standard ellipsometry, the refractive index, n, is easily derived from the measured Ψ and Δ of a single isotropic boundary. This will not be the case, however, if the sample is a thin film, or layers of thin films, placed upon a substrate. The reflected wave will be a superposition of waves reflected from the different boundaries. These reflected waves may interfere and cause local maxima for certain angles. Spectroscopic ellipsometry with a variable angle of incidence is thus a powerful tool to measure the thickness and refractive indices of each layer.

Berreman et al. [84] [85] [86] [87] developed a 4x4 matrix algorithm, thoroughly explained in the *Handbook of Ellipsometry* [88], to calculate the reflection coefficient for a plane wave reflected from a stack of anisotropic layers with parallel boundaries. This method enables decomposition of the system matrix of a measured multilayered film into each layers individual Mueller matrix. The method is implemented in most commercial ellipsometer data analysing software.

The accuracy of the model obtained from the Berreman method compared to the experimental data is tested by calculating the Mean Square Error (MSE). It is defined as

$$MSE = \sqrt{\frac{1}{2N-M}\sum_{i=1}^{N}\left[\left(\frac{\Psi_i^{mod}-\Psi_i^{exp}}{\sigma_{\Psi,i}^{exp}}\right)^2+\left(\frac{\Delta_i^{mod}-\Delta_i^{exp}}{\sigma_{\Delta,i}^{exp}}\right)^2\right]}, \tag{4.1}$$

where N is the number of Ψ - Δ pairs, M is the number of variable parameters in the model, and σ_i is the standard deviation in the experimental data points. The fitting problem is thus reduced to finding a set of variable models resulting in a single unique absolute minimum of MSE.

Mueller matrix measurements of the films were performed with a J.A.Woollam dual rotating compensator (RC2) Ellipsometer, Figure 21, using three different angles of incident. The characterisation was then completed by curve fitting the data from the RC2 ellipsometer in CompleteEASE, and searching for a minimum MSE using models described in section 2.7.

4.4 Surface Characterisation of the Thin Films

Various techniques within the NTNU NanoLab were employed in order to study the surface roughness of the produced films.

Atomic Force Microscopy

Atomic Force Microscopy (AFM) provides topographic measurements of surfaces with nanometric scale resolution. Applicable for both organic and inorganic materials, it is a

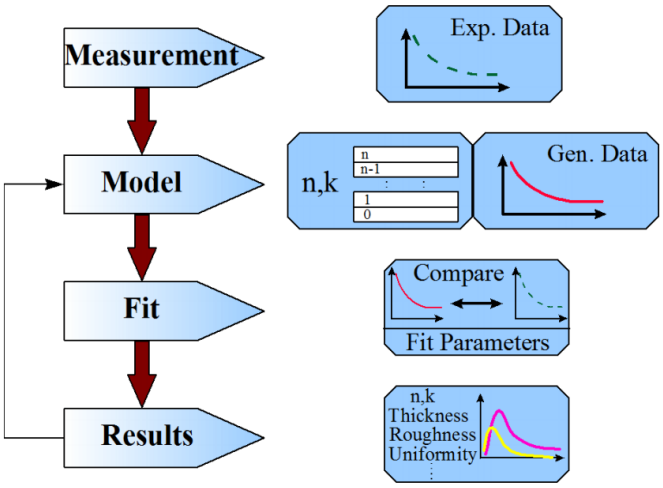

Figure 17: Basic procedure used in ellipsometry measurements to determine material properties from experimental data. Models are built based on experimental data, then fitted and continuously improved until an acceptably low MSE is reached.
Credits: J.A. Woollam Co., Inc.

useful tool to study properties such as topography, roughness and softness.

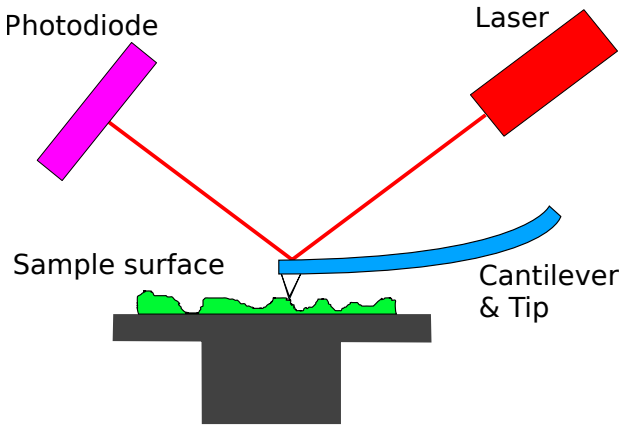

Figure 18: A simple sketch of an AFM.

A simple sketch of an AFM is shown in Figure 18. The sharp tip at the end of the cantilever is used to scan the specimen surface. A sharp tip is required for high resolution. As the tip probes the surface, the forces between the tip and the specimen surface will cause a deflection of the cantilever according to Hooke's Law. The cantilever is generally made of silicon or silicon nitride and the spring constant is typically in the order of $\sim$1N/m.

An AFM can operate in different modes, according to the nature of the tip motion. The three modes are contact mode, tapping mode, and non-contact mode. The different

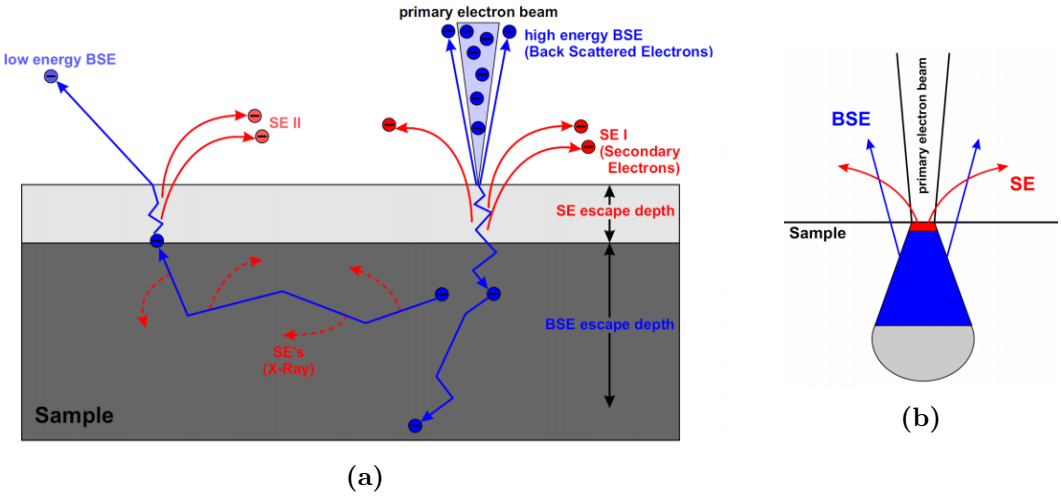

Figure 19: Figure (a) shows the interactions and formations of the BSE and SE within the sample. Figure (b) displays the interaction volume and resulting resolution of the SE and BSE.
Credits: NTNU NanoLab

modes are applicable for different samples, e.g. if one is investigating a liquid, tapping mode is superior since contact mode might cause liquid to stick to the tip. The AFM diMultimode V at NTNU NanoLab, produced by Veeco Metrology, offers a fourth possible mode, called ScanAsyst. ScanAsyst uses peak force mode to calculate the optimal setting for every individual sample, enabling even inexperienced users to achieve quality measurements.

Scanning Electron Microscopy

In a Scanning Electron Microscope (SEM) an image is produced by scanning a focused electron beam over the surface of a sample. The electrons interactions with the material will produce Secondary Electrons (SE) and Back Scattered Electrons (BSE). This is illustrated in Figure 19a. SEM provides information about both a samples surface topography and its composition. As seen in Figure 19b, the SE signal is of high resolution and is used to investigate the topographical features of the sample. The much greater penetration depth of the BSE compromises the high resolution, but gives elemental (Z) contrast.

The acceleration voltage and beam current are essential for the resolution of the SEM image. Decreasing the acceleration voltage will result in a smaller interaction volume (higher resolution), but will increase the spherical aberration of the lens (lower resolution). Increasing the beam current gives an enhanced signal-to-noise ratio (smoother edges), but also a larger beam size (lower resolution) due to repulsion between the electrons. A typical image might have an acceleration voltage of 10 kV and a beam current

of 0.5 nA. The adjustment of these parameters depends greatly on which information one aims to extract, and optimised adjustments are critical for high quality results.

The FEI SEM APREO at the NTNU NanoLab is built to operate in different modes. In *Standard Operational Lens Mode*, the secondary electrons are detected by a Everhart Thornley Detector [89] (ETD). This mode is ideal for navigation and imaging at lower magnifications. For non-magnetic samples, the instrument can be run in *Immersion Mode*. In immersion mode, a very strong magnetic field is applied between the lens and sample, which serves to focus and collimate the electron beam even further. The two detectors T1 and T2 detect the BSE and SE, respectively. While standard mode is easier to use, immersion mode offers ultrahigh resolution on a nanometeric scale.

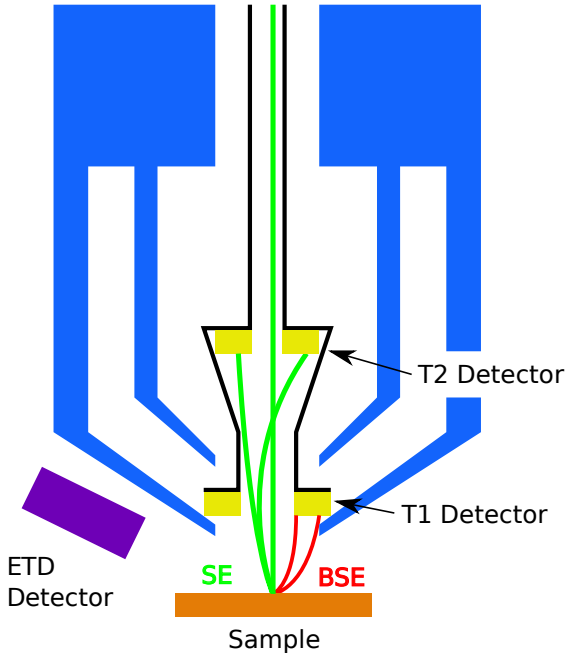

Figure 20: A sketch of the SEM APREO showing the detection of BSE and SE in immersion mode. Credits: NTNU NanoLab

3D Optical Profiler

The 3D optical profiler (3D-OP) utilises white light interferometry which allows for rapid, non-destructive imaging of a sample surface. It is an excellent tool to study parameters such as surface roughness and step height. The *Bruker Contour GT-K Profiler* at the NTNU NanoLab supports two different measurement techniques: vertical scanning interferometry (VSI/VXI) and phase shifting interferometry (PSI) [90]. The latter technique offers sub 1 nm vertical resolution and can be run with a monochromatic green light source.

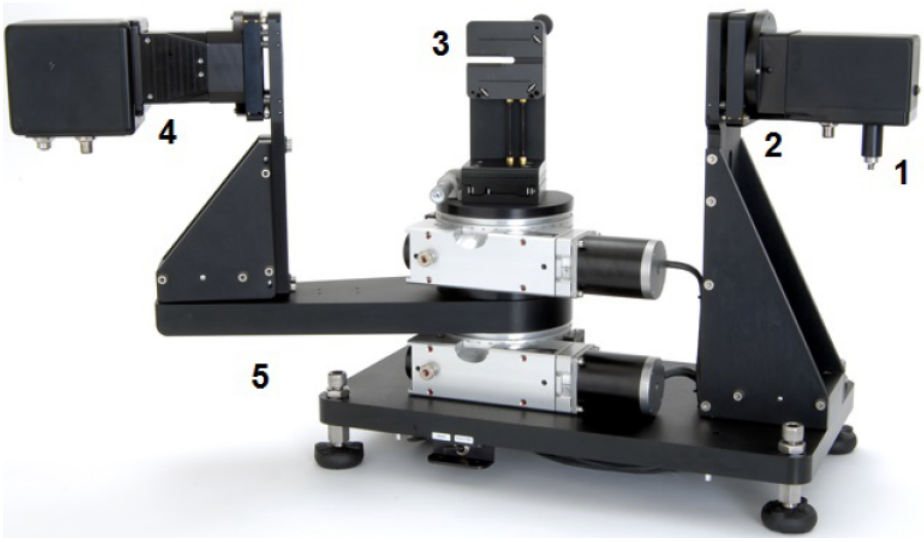

Figure 21: An image of the RC2 Ellipsometer.
Credits: J.A. Woollam Co., Inc.

Table 2: RC-2 components list

# in Figure 21	Component
1	The light source: a 150W Xenon lamp.
2	Source optics unit: has a software controlled intensity unit, collimator, a fixed polariser element, and an achromatic prism compensator which operates at 10Hz.
3	Sample mount: a vacuum pump keeps the samples in place, and the slit is for transmission measurements.
4	Reciever optics unit: consists of a through-hole quadrant detector, a compensator element which rotates at 6Hz, and a fixed polariser. Light then enter two spectrometers: an Si CCD detector for the 210-1000 nm wavelength range and an InGaAs photodiode array for wavelengths between 1000-1690 nm.
5	Auto angle vertical sample mount base unit: Consists of a high accuracy variable angle rotating arm and stepper motors for accurate angle reflection/ transmission measurements.
6	RC2 Electronics Box (not shown): contains DC converter for power supply.

4.5 Metasurface Structuring

Once a high quality multilayered film with sufficiently low surface roughness has been produced and its optical properties thoroughly investigated, the structuring process can be initiated. Two well known structuring techniques are briefly described here; *Etching* and *Lift-off*.

Etching

The first step of an etching process is to place a layer on top of the film and form this into a mask. The mask must have the same pattern as the desired end result. The sample is then etched, with the mask protecting certain parts of the film while leaving other exposed. The etching process will etch away the exposed part, leaving a patterned layer of film when the mask is removed.

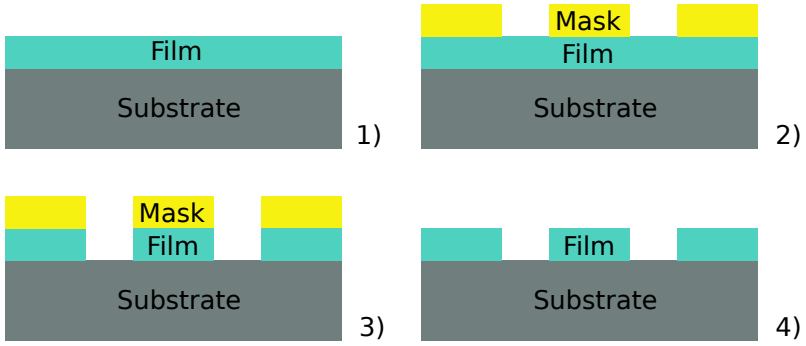

Figure 22: Etching: 1) A film is deposited on a substrate. 2) A material is placed atop the film and structured into a mask. 3) The exposed film is etched away. 4) The mask is removed and a structured film remains.

Lift-off

In a sense, lift-off is the opposite of etching. A sacrificial layer, e.g. a photoresist, is placed atop the substrate and an inverse pattern created. A film is then deposited and the sacrificial layer removed, leaving only deposited material in the areas where the sacrificial material was absent.

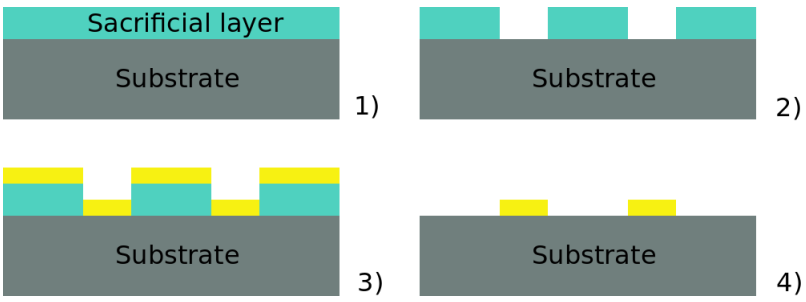

Figure 23: Lift-off: 1) A sacrificial layer is placed atop a substrate. 2) The sacrificial layer is structured into an inverse pattern. 3) Target material is deposited. 4) The sacrificial layer is removed and a film structure is left on the substrate.

4.6 Final testing

Characterisation of the nanostructured film will be similar to the testing of the multilayered films. The surface structures will be imaged with AFM, SEM and 3D-OP. Ellipsometric measurements in RC2 will verify if the wanted optical properties have been achieved or not.

5 Realisation of an FLC-based Mueller Matrix Spectroscope

The major part of this thesis was the construction and calibration of a spectroscopic FLC-based Mueller matrix ellipsometer in the visible and near infrared region, with the prospect of building it into an imaging system. In this section, the components, the data acquisition programs, and the data processing will be presented.

5.1 Components in the Setup

The components of the setup were based on both work from former students and PhD-candidates, and newly acquired instruments.

5.1.1 The FLCs

The FLC-based PSG and PSA were developed by Hagen in his masters thesis [83]. The design was chosen based on a genetic algorithm developed by Letnes et al. [43] for spectroscopy in the 550 nm to 1150 nm range. This range is know as the optical window for biological tissue, and the goal was to build a system that could perform Mueller matrix transmission imaging of biosamples. Table 3 shows the result of the optimised genetic algorithm, the components, and their orientation of the PSG and PSA built. At the front of the PSG and at the back of the PSA there is a linear polariser. Due to the uniqueness of the setup, the components were custom made. The FLCs were manufactured by CITIZEN FINETECH MIYOTA, and the waveplates by CASIX. The FLCs are connected to the computer using a *NI SCB-68* shielded I/O connector block and a *NI PCI 6259* DAQ, both products from National Instruments.

Table 3: The best result of the genetic algorithm. Angle refers to the theoretical angle of the components, while PSG and PSA are the azimuthal angels of the realised design. The note is at what wavelength the component will act as either a half waveplate ($\lambda/2$) or a quarter waveplate ($\lambda/4$).

Component	Thickness	Angle [°]	PSG [°]	PSA [°]	Note
FLC1	1.348	142.3	136.3	135.8	$\lambda/2$ @ 610 nm
FLC2	1.456	72.7	70.3	71.4	$\lambda/2$ @ 650 nm
WP1	1.439	73.7	74.2	73.7	$\lambda/4$ @ 630 nm
WP2	1.585	8.6	0.6	3.0	$\lambda/4$ @ 690 nm

5.1.2 The Supercontinuum Light Source

The supercontinuum light source consists of a monochormatic laser source, a photonic crystal fiber, and an AOTF. It operates as explained in section 2.6. The laser source

is a *WL-SC-400-8-PP-02 WhiteLase Super Continuum laser* provided by *Fianium UK Ltd.* The unpolarised light emitted from the photonic crystal fibre ranges from 400 to 2400 nm, and the total power of the source is > 8W. The fundamental repetition rate is 80MHz, but this is adjustable in the 100kHz- 80MHz range.

The AOTF is an *AOTF-N1-D-FDS-MM Acousto-Optic Tunable Filter system*, also supplied by *Fianium UK Ltd.*. It has a wavelength range from 600 to 1100 nm, with a bandwidth of 2-5 nm, a minimum step length of 5 nm, and a 90% maximum diffraction efficiency. The resulting laser spot has a diameter of $\sim$3.4 mm at 650 nm. It is highly collimated with both high spatial and temporal coherence. The exhibited light is vertically polarised.

The RF input on the AOTF is controlled by a *AODS Synth DDS 8 CH* from *Gooch & Housego*.

5.1.3 Calibration Samples

The four calibration samples required to perform the eigenvalue calibration method, described in section 3.3, were the same as used by Hagen in his thesis. The first sample was air, the next two were linear polarisers that should have a 0° and 90° orientation for optimal results, and the last calibration sample was a quartz crystal acting as a quarter-waveplate at 910 nm oriented at 55°. The samples were mounted on an automatic six-slotted filter wheel, where one of the empty slots was covered in order to perform zero-reference measurements.

5.1.4 Other Components

Intensity measurements are performed with an InGaAs point detector from *OEC GmbH*, which has a measurement rate tunable up to 150kHz. The detector returns voltage between 0 and 10 depending on the input power. A *Textronic TDS 200 oscilloscope* was utilised for easy monitoring of the intensity measurements.

Due to the high output power of the light source, neutral density filters were placed in front of the PSG to prevent saturation and possible destruction of the detector. Samples to be measured were mounted in the sample holder which could be moved vertically and horisontally othogonal to the optical axis. Vertical and horisontal movement was controlled with a Standa 8MT175 stepper motor and a Thorlabs LTS300 stepper motor, respectively. The calibration samples were mounted in the *Thorlabs FW102C* filter wheel.

The bandwidth of the source was investigated with an *Ocean Optics USB4000-UV-VIS Spectrometer* and a basic spectralon. The spectrometer only covers the 200 to 850 nm range, so no measurements of longer wavelengths were possible.

5.2 Software

The light source, FLCs, calibration sample filter wheel, stepper motors, and detector, were all controlled using National Instruments LabVIEW 2012. The function of one of the main programs was to investigate the behaviour of the FLCs and the light source. A second important program performed the Mueller matrix measurements and the calibration measurements.

5.2.1 Component Behaviour

The combination of FLCs with an AOTF enables fast spectroscopic measurements. It was, however, important to ensure that the frequency of the light and the state of the FLCs were stable before intensity measurements were performed. The switching speed of both the FLCs and the AOTF was of interest, and a program was written in order to investigate this.

The interface for this program is shown in Figure 24. The total run time of the program is shown in the panel marked 1). In panel 2) one can perform a test of the FLCs to see how fast they switch and how steady their given state is. Multiple controls for a frequency range scan are found in 3). Of special interest is *Step*, the wavelength step length between each measurement. This was generally set to 5. Increasing *Samples* (the number of detector measurements per wavelength) or *Iterations* (the back-and-forth switching of the FLCs) may give a better result, but will increase the run time of the program. The number of detector measurements per wavelength was generally set to 100. The laser source can be manually controlled in 4), and any written command and its response will be shown in the "Output Text"-frame, 5). All measured intensities are constantly graphed in 6), and 7) will display any error that may occur.

5.2.2 Sample and Calibration Measurements

The main program for performing sample or calibration measurements is shown in Figure 25. The panel denoted 1) contains a short user interface which enables users to run the program without thorough knowledge on how it is written. The user chooses between sample measurement or calibration measurement in panel 2). He must also decide if a filter wheel should be applied or not. 3) and 4) serves the same purpose as in the program presented in section 5.2.1, providing a manual way to control the laser source. A "Start Scan" button has not been implemented, so the scan will start when "Exit" is pressed. It is therefore important to set the scan parameters, 5), before pressing "Exit". Two buttons which force stop the program are shown in 6), output data from the detector is graphed in the intensity plot, 7), and 8) will show any errors obtained when the program is run. The program was also written to function with a manual filter wheel. Since the user must physically move this filter wheel for each different sample, six

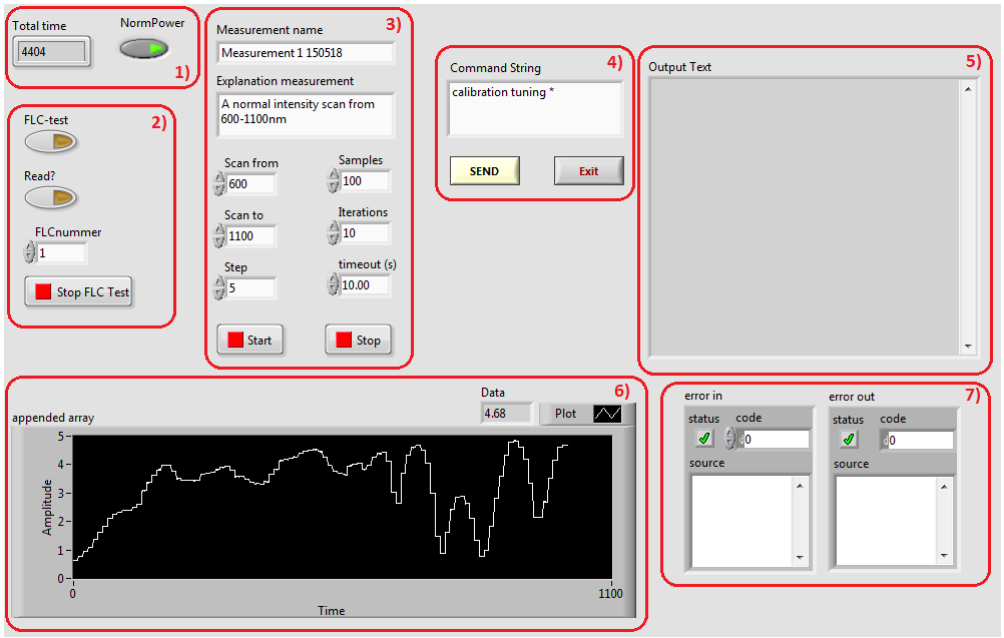

Figure 24: The interface of the LabView program used to investigate the component behaviour.

descriptive buttons, 9), were added to resume the program after performing a change. The manual filter wheel was never utilised for any measurements.

5.3 Data Processing

All calculations and plotting were preformed in Matlab R2017a. An already existing program performing the eigenvalue calibration method derived in section 3.3 was used on the acquired calibration data in order to find system matrices for the PSG and the PSA. Another program which performed the forward product decomposition from section 2.5.1 was used to find exact values, such as the azimuthal orientation of the calibration samples.

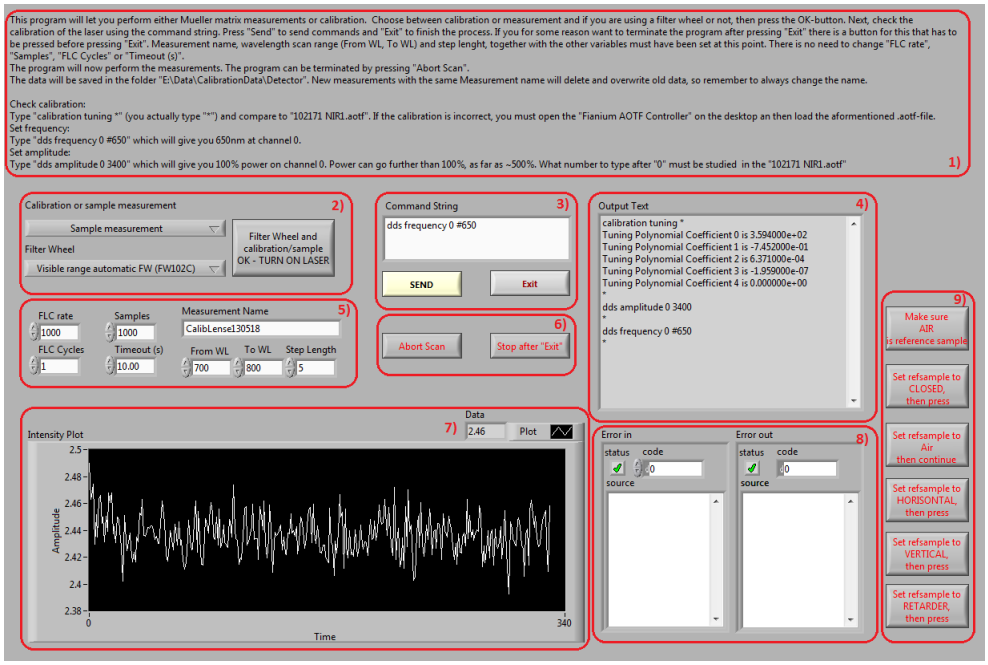

Figure 25: The interface of the LabView program used to perform Mueller matrix measurements.

6 Results and discussion

6.1 An FLC Bulk System

Bulk systems consisting of a tunable supercontinuum source and an FLC-based PSG and PSA, have multiple components that should be investigated in order to understand and ensure a good final result. The bandwidth, polarisation, intensity output, stability, and tuning speed of the source were explored. The switch time and stability of the FLCs, and the performance of the three calibration samples were also investigated. Finally, the performance of the bulk system was tested, and the prospects of advancing this into an imaging system reviewed.

6.1.1 The Light Source

The relative intensity of the light source in the 600-1100 nm range was investigated. Due to the high intensity of the source, three neutral density filters were applied to prevent saturation and possible destruction of the detector. The intensity was measured for every fifth nm in the regime, and the mean value of 1000 measurements per wavelength reported.

As one can clearly see from Figure 27, the measured relative intensity differs from the plot provided by the producer of the laser. Various setups were tested, but the results were more or less identical. An example was to exclude the use of neutral density filters and instead introduce two nearly crossed polarisers, but as with the other alterations this had no great effect.

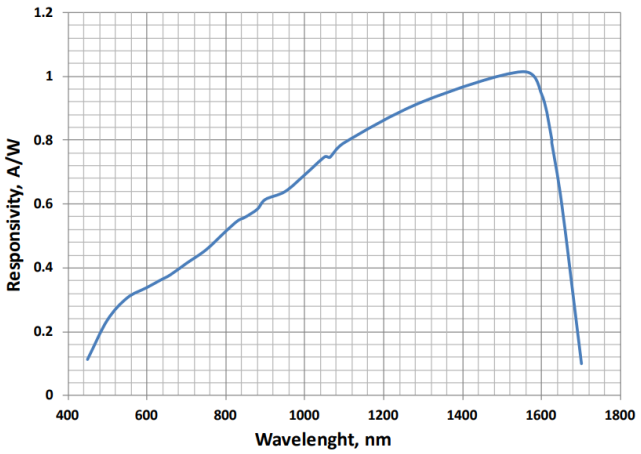

Figure 26: Typical responsivity of a visible range extended InGaAs photodiode. Credits: Luna Optoelectronics

Since the intensity scan exhibited similar results for the different experimental setups,

either a part of the source or the detector must be at fault. The graph provided by the producer of the laser shows the intensity spectrum for white light emitted from the photonic crystal fiber. There is no available data on how the AOTF may alter this spectrum, so this could possibly be the reason for the different result. The graph is also from a different model than the one used here, but according to the producers the graph should have an identical shape. Every laser has, however, a slightly unique specter, which might be the case for the one used here.

The responsivity of a typical extended InGaAs detector increases with the wavelength, as shown in Figure 26 [91]. This contradicts the lack of sharp high intensity peaks at $\sim$ 1050 nm in the measured intensity. Another plausible explanation may be the fact that the detector is old and has lost some of its responsivity. It would be of interest to test both the light source and the detector uniquely to determine the cause of the error, but this has not been possible due to lack of equipment.

It is, however, clear from the ratio plot in Figure 27a that a decrease in the intensity will be measured equally over the entire range. The source and detector are therefore suitable for Mueller matrix spectroscopy, regardless of the aforementioned errors.

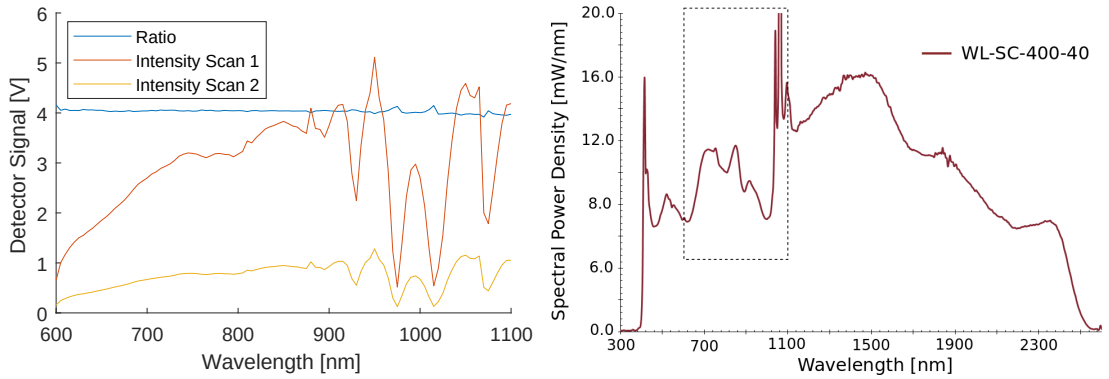

Figure 27: Figure (a): the relative intensity of the light source measured from 600 to 1100 nm with a 5 nm step length. The difference between *Intensity Scan 1* and *Intensity Scan 2* is an additional 25% neutral density filter at the latter. The blue line is the ratio between the two scans. Figure (b): the intensity of the corresponding 20W Fianium laser according to the producer. The 600-1100 nm regime has been framed with a stippled line.
Credits: NKT Photonics A/S

One of the big advantages of combining an AOTF with FLCs is the ability to quickly perform measurements at different wavelengths. In the efforts to shorten the time it takes to perform measurements, while still obtaining quality result, the switch speed and stability of the source were investigated. A random interval (920 to 970 nm) was chosen for study of the AOTF change speed. Figure 28 depicts how a stable output is reached within 2 milliseconds. A five millisecond delay in the software between the change of wavelength and measurements should therefore suffice.

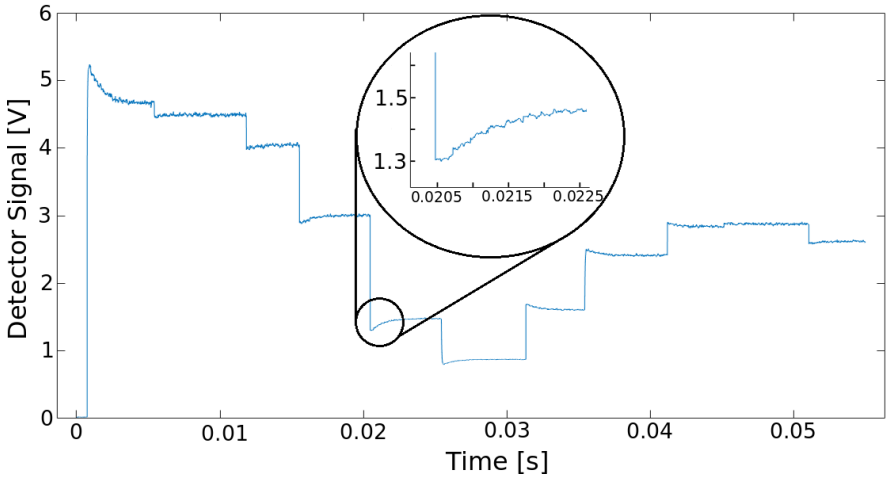

Figure 28: The speed of which the AOTF changes from one frequency to another. The scan is from 920 to 970 nm.

As can be seen from Figure 29, the light source output is stable with less than 0.2 % deviation. A one second plot is enough to show this, since the source changes wavelength many times per second when a Mueller matrix measurement is performed. The stability of the source is therefore of no concern.

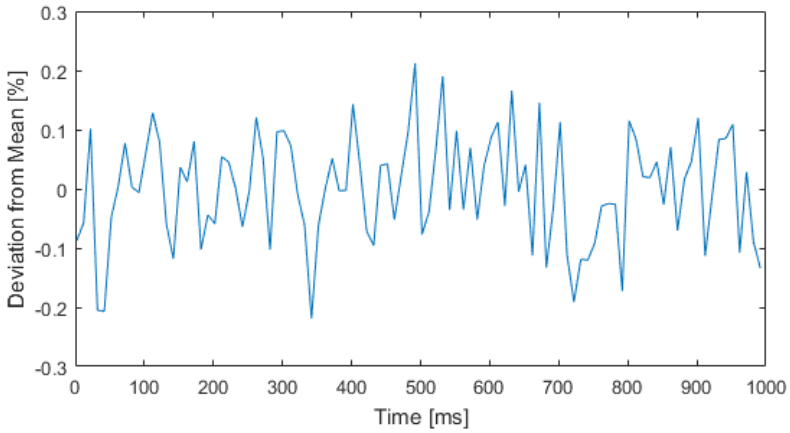

Figure 29: A one second mapping of the stability of the source.

Four spectrometer measurements, shown in Figure 30, were performed in order to study the bandwidth of the source. Only wavelengths in the 600 to 810 nm regime were explored, due to lack of a functioning NIR spectrometer. All four wavelengths were found to have a bandwidth of less than 2 nm, where *full width at half maximum* has been used as a standard. No second order harmonics of any significance were observed.

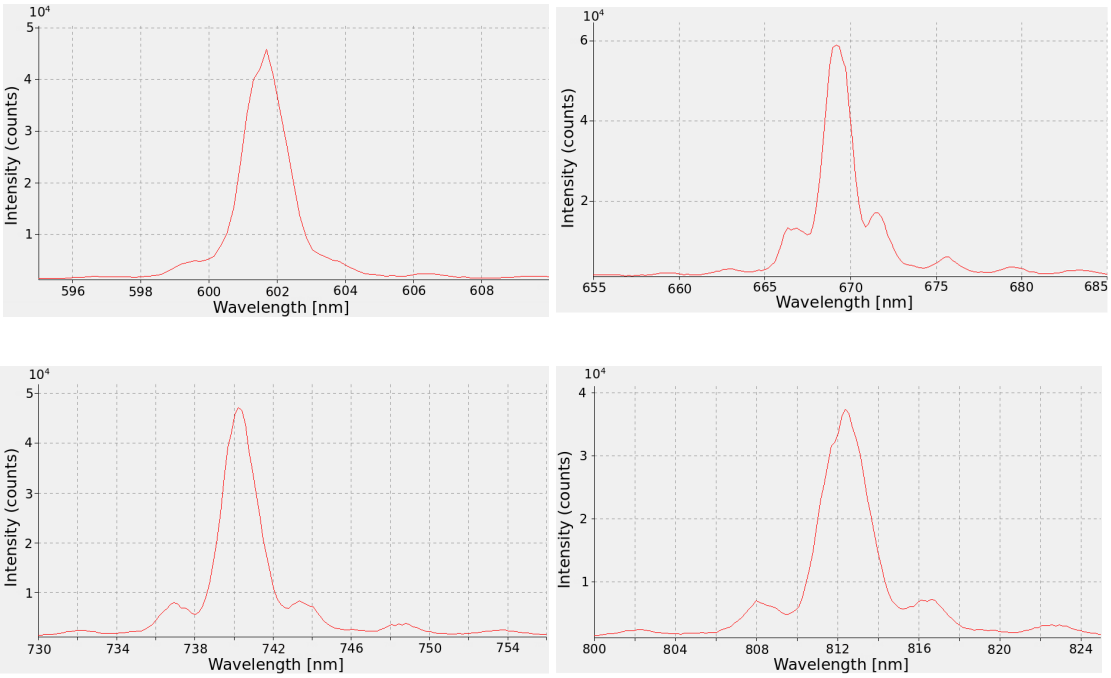

Figure 30: Spectrometer measurements at 600 nm, 670 nm, 740 nm, and 810 nm.

6.1.2 The FLCs

It is of crucial importance that the FLCs have reached a stable state before measurements are performed. The speed at which the FLCs shifted was investigated, and the results can be seen in Figure 31. Continuous measurements were performed as the system switched through the 16 possible states. The system would overshoot and then stabilise, reaching a steady state within ~ 5 ms.

Figure 32 shows a similar FLC switch time measurement, but this time measurements were performed over several seconds. The aim was to study the stability over a long period of time. The figure shows how the apparent steady state reached within a few milliseconds actually starts to drift, and a proper steady state is not reached until ~ 0.2 seconds have passed. This poor performance is not unusual for old components of this type, and a known solution is to switch the FLCs back and forth multiple times before a final state is set. Further testing will, however, be required to confirm the effect of repeated switching. In the meantime, a delay in the software was implemented to prevent measurements from being performed while the FLCs were still adjusting. The complete Mueller matrix measurement scans through all wavelengths for each FLC state. There are 16 changes of state, and a complete Mueller matrix measurement is thus prolonged by 3.2 seconds due to this delay.

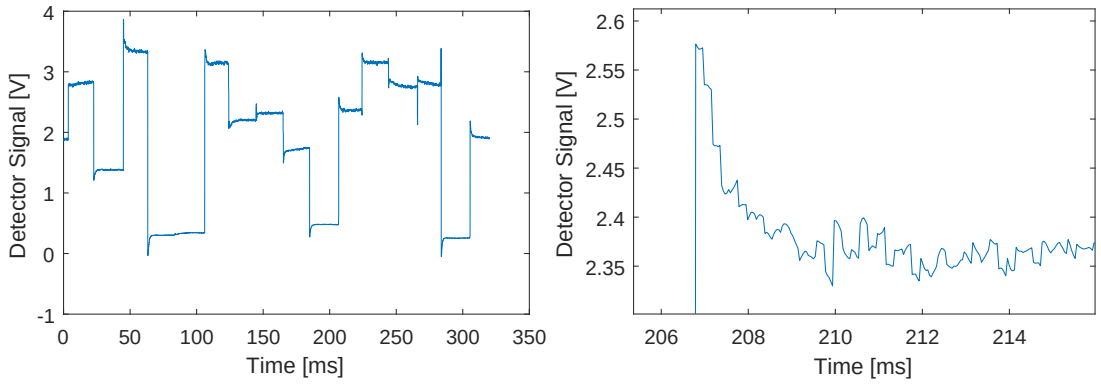

(a) (b)

Figure 31: Figure (a) shows the intensity measured on the detector for the 16 different states of the FLCs, while Figure (b) displays how a stable state is reached within milliseconds.

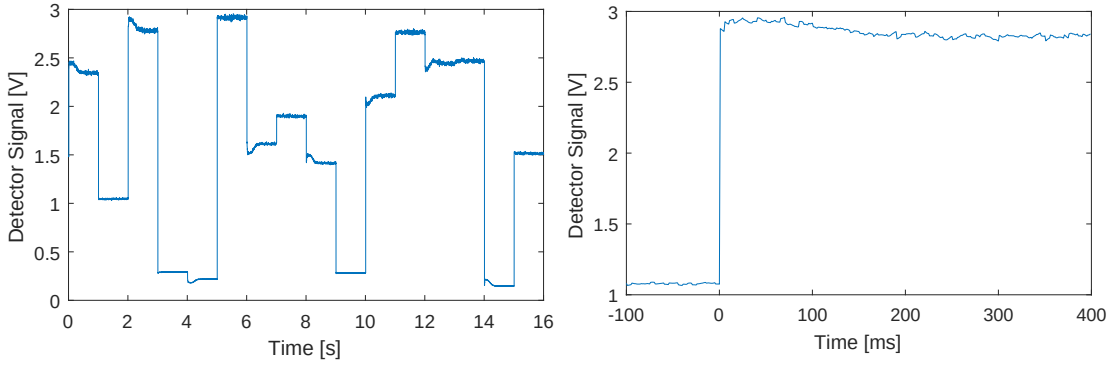

(a) (b)

Figure 32: Figure (a) shows switching through all 16 FLC states performed over several seconds. The overshoots are not as distinct as in Figure 31a due to lower measurement frequency. Figure (b) displays how the FLC will drift after a state has been set, but eventually reach a stable state.

6.1.3 Calibration Samples

According to the laser producer, the light source should emit vertically polarised light. If a perfect polariser is oriented perpendicular to the polarisation of the source, the resulting intensity output should equal zero. A good test of the two polarisers is therefore to individually orient them horisontally and perform an intensity scan. Perpendicular orientation was obtained by turning the laser on at 670 nm and then rotating the polariser under investigation until a minimum intensity on the detector was found. All other components, eventually also the neutral density filters, had been removed from the setup, so a slight misalignment of only a few degrees quickly caused saturation of the detector. A scan from 600 to 1100 nm with a step length of 5 nm was then performed, before the process was repeated for the second polariser.

It is clear from Figure 33 that the first polariser performed better than the second. This is in accordance with the alignment of the polarisers, where the first polariser obtained a far lower minimum detector output than the other. The conclusion must then be that the first polariser was better and more suited as a calibration sample.

A quite surprising result is the opposite intensity perturbation of the two polarisers. A local minima for the first polariser coincides with a local maxima for the second polariser. The periodicity of the perturbations is about 30 nm, and increases slightly with the longer wavelengths.

The only plausible explanation for this perturbation is the fact that the light emitted from the AOTF was not perfectly vertically polarised. If the polarisation varied slightly with the wavelength, the resulting intensity emitted from the polariser should also vary, as illustrated in Figure 34. If the polarisers were slightly misaligned with respect to each other, this would cause the occurrence of maximas and minimas at different wavelengths, as already seen in Figure 33.

Although it appears that the polarisation of the source might be perturbing around a vertical polarisation, this does not significantly impact the construction of the Mueller matrix spectrometer. The very first component of the PSG is a vertical polariser, so as long as the polarisation is stable for each wavelength, this will cause no problems. The poor performance of one of the polarisers would, however, prove a greater issue when calibration measurements were performed and analysed.

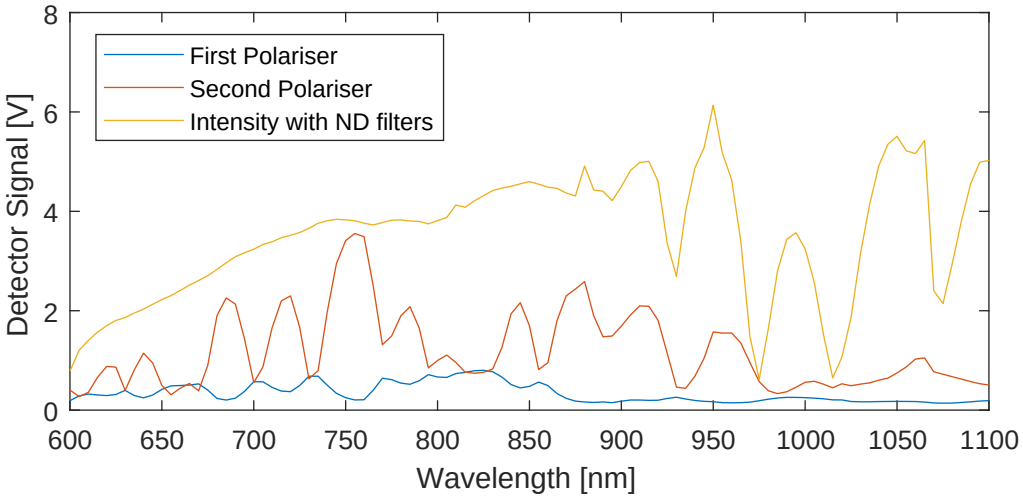

Figure 33: Intensity scan for the two calibration polarisers oriented orthogonal to the polarisation of the source. The relative intensity spectrum of the source is included as a reference regarding the shape of the intensity scan.

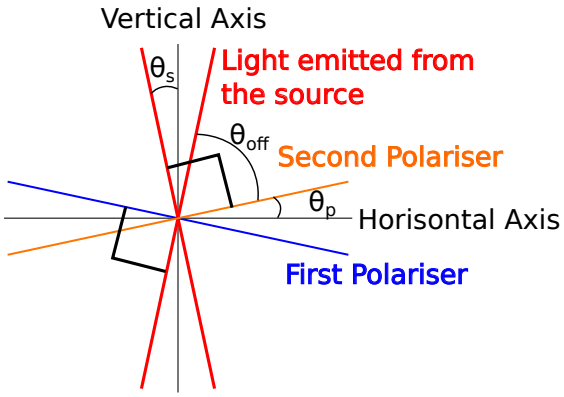

Figure 34: A small perturbation, θ_s, in the polarisation of the source will cause a shifting angle, θ_{off}, between the polarisation of the source and the polarisation filter. This results in a varying intensity measurement. Due to a slight relative misalignment, $2\theta_p$, between the two filters, a local minima at one wavelength might result in a local maxima for the other, and vice versa. For illustrative purposes, all angles are greatly exaggerated.

6.1.4 Calibration of the Spectroscopic Mueller Matrix Ellipsometer

A calibration scan from 600 to 1100 nm with a step length of 5 nm was performed and analysed in accordance with the eigenvalue calibration method described in section 3.3. The resulting Mueller matrix elements are shown in Figure 35, where all elements are normalised with regards to MM_{11}. Comparing these elements to the theoretical matrices in Appendix B, one sees a promising result in the 700 to 930 nm regime with a $< 2\%$ error in the air and polariser measurements. The errors in the Mueller matrix elements of the 90° polariser were greater than for the 0° polariser. This is not surprising given that the polariser with poorer performance was the same one used as a 90° polariser in the calibration process. The time to perform a complete calibration was around 90 seconds, but this was greatly dependent on the number of measurements per wavelength. A complete calibration is in reality four measurements of different samples, so a complete Mueller matrix measurement is performed in about 20 seconds, since the switching time of the filter wheel can be excluded. This time can easily be reduced by performing fewer measurements per wavelength and by resolving the matter of drifting FLCs.

According to the plot of the inverse condition numbers for the PSG and PSA in Figure 36, the two components display excellent performance in the visible regime. They fall off as the wavelength increases, and at 1100 nm the inverse condition number of the two components was about 0.25, which is relatively poor.

Forward product decomposition, explained in section 2.5.1, was used to study the orientation of the calibration samples. The orientation of the vertical and horisontal polarisation filters were found to be 0.1° and 89.2°, respectively. The retarder, on the other hand, was a slightly more complicated matter. The quartz crystal, acting as a quarter-waveplate at 910 nm, was studied both in the RC2, and with forward product

decomposition of the calibration data. The angles are graphed in Figure 37. In the graphs, the angle appears to be perturbing. The two results are more or less identical, except for a slightly higher amplitude in the RC2 measurements. It is, however, highly unlikely that the orientation of the securely fastened waveplate is actually perturbing, so the apparent perturbations are believed to be caused by Fabry-Pérot interferrence. The results are more easily understood if compared to a general linear retarder, shown in Appendix B. The five perturbing elements are all θ dependent, so when the interferrence is measured, these will cause the periodic change in orientation from Figure 37. The 33 and 44 matrix elements are $cos(\delta)$ dependent, where δ is the phase shift discussed in section 2.3.2. It is natural that this will decrease towards zero as $\delta = \pi/2$ at 910 nm. Studying the Mueller matrix elements of the retarder, one can see that at 910 nm the matrix is identical to that of a perfect retarder, with an error $< 1\%$ for all matrix elements.

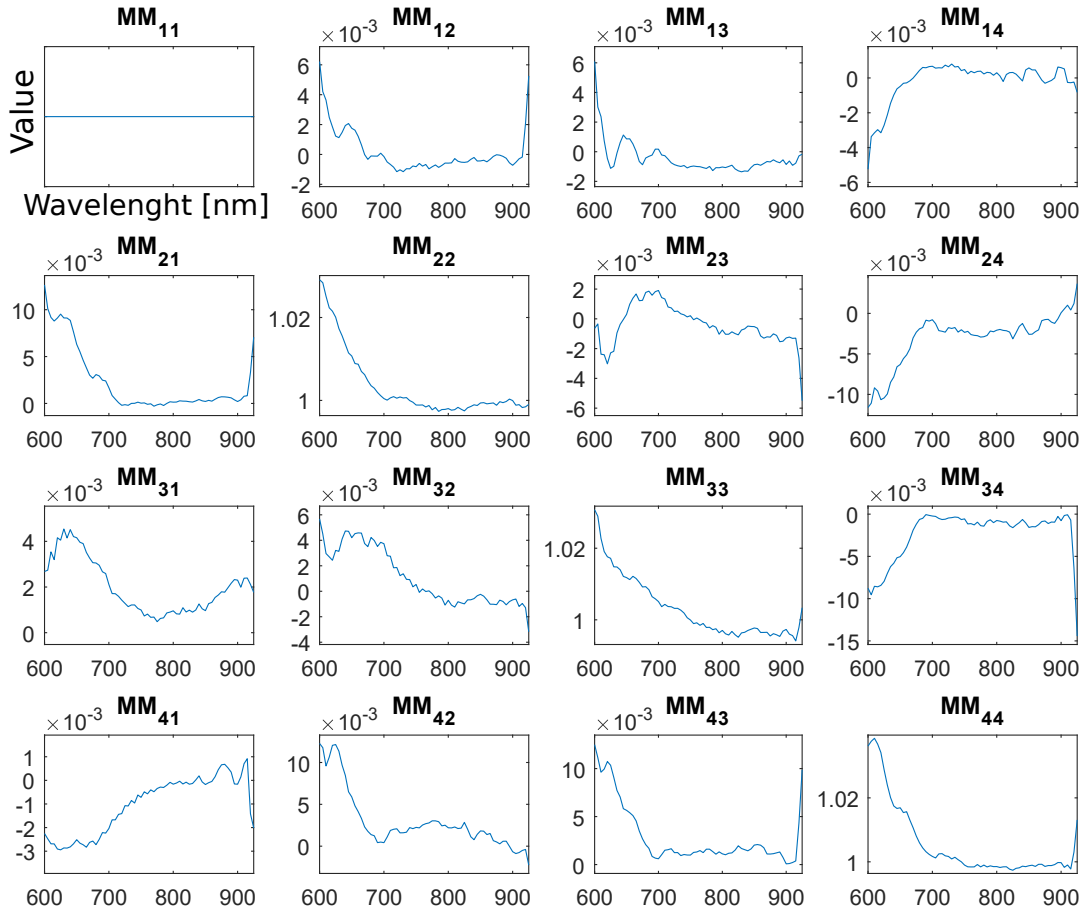

Figure 35 (a): The Mueller matrix elements of the air reference sample.

Satisfying results were achieved in the 700 to 930 nm range, and it could be interesting to review why a broader range was not accomplished. Given to the excellent inverse

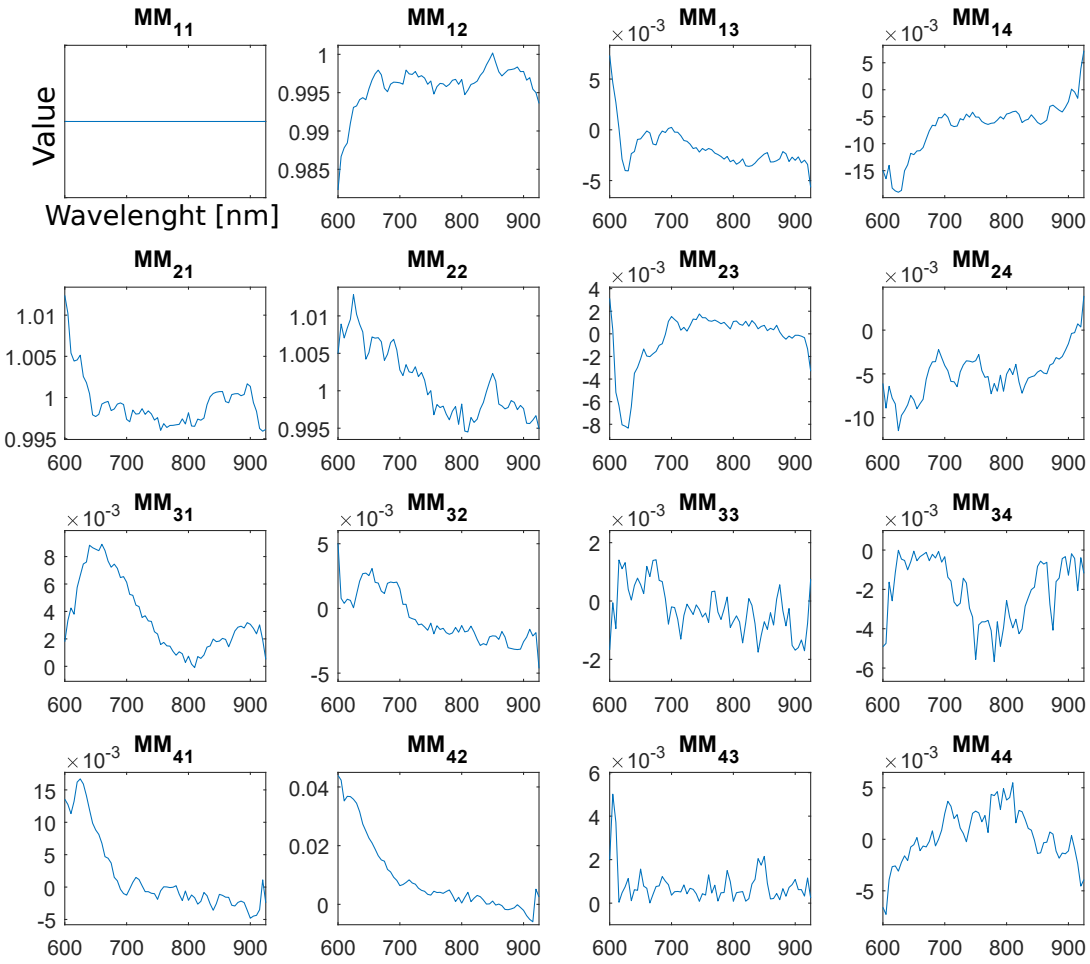

Figure 35 (b): The Mueller matrix elements of the 0° polariser reference sample.

condition numbers, it should be possible to obtain satisfying measurements, especially for shorter wavelengths. As a general rule, the best measurements were obtained with a low intensity input on the detector. Multiple alterations were tested, mainly experimenting with lowering the intensity before entering the PSG. All components were tilted slightly in order to prevent Fabry-Pérot interference from the highly spatially and temporally coherent source. One setup in particular showed promising results in the 600 to 930 nm regime with $< 1\%$ error for the Mueller matrix elements of both air and the 0° polariser. The 90° polariser elements were, however, off by an unacceptable amount. The use of a different polariser should therefore be investigated.

Regardless of the setup, the system failed completely at wavelengths surpassing 930 nm. The reason was believed to be the generation of second order harmonics, discussed in

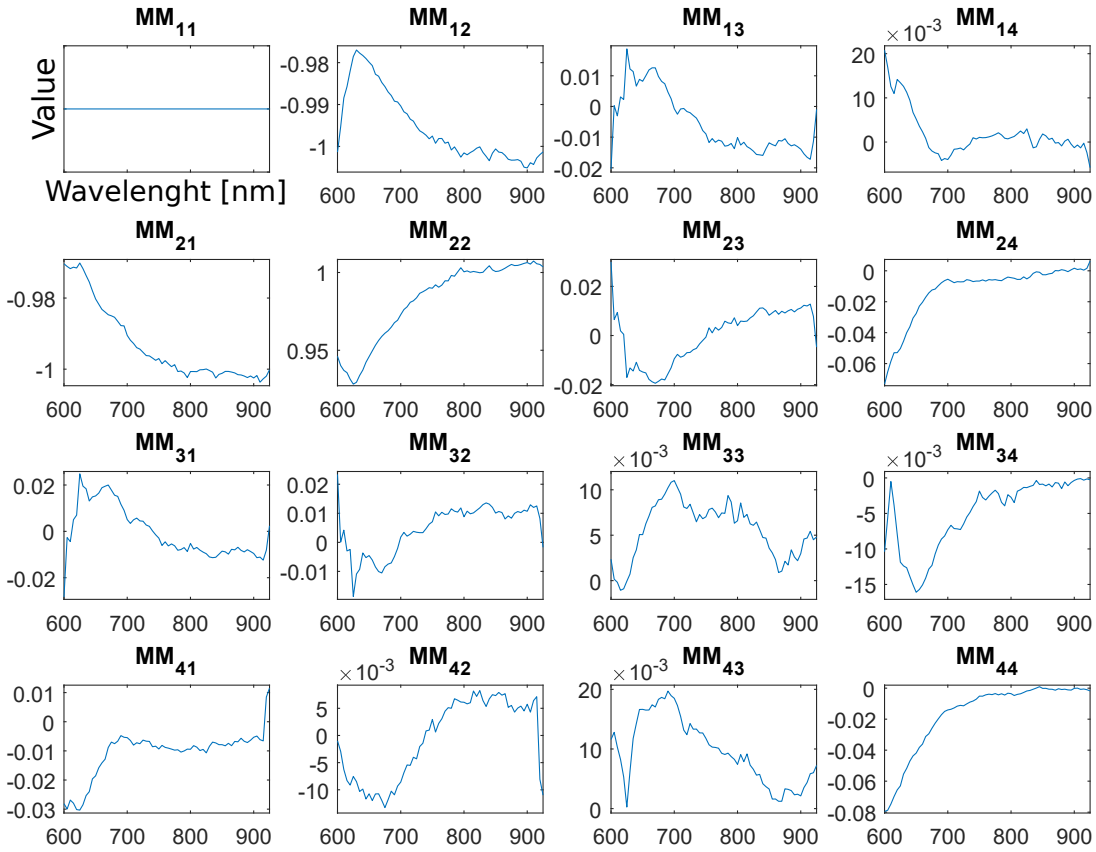

Figure 35 (c): The Mueller matrix elements of the 90° polariser reference sample.

section 2.6. These are clearly visible as the source passes 950 nm, and can easily be removed by introducing a longpass filter. Introduction of a longpass filter had, however, minimal effect. Numerous alterations were tested in order to reach an acceptable result, but none were successful.

6.1.5 Summary

The fast switching time and good stability of the supercontinuum laser source make it a useful tool for fast, high intensity measurements. The switching time of the FLCs proved surprisingly poor, since they would start drifting after an apparent steady state was reached. A true steady state was reached 0.2 seconds after switching was initiated. This is extremely slow for components of this type. Measures to prevent drifting have been suggested, but the short term solution was to delay the software and give the components time to stabilise before measurements were initiated. The program controlling the measurements scans through all wavelengths for each FLC state. If the switch time for the FLCs and the laser source had been the same, the program could have switched

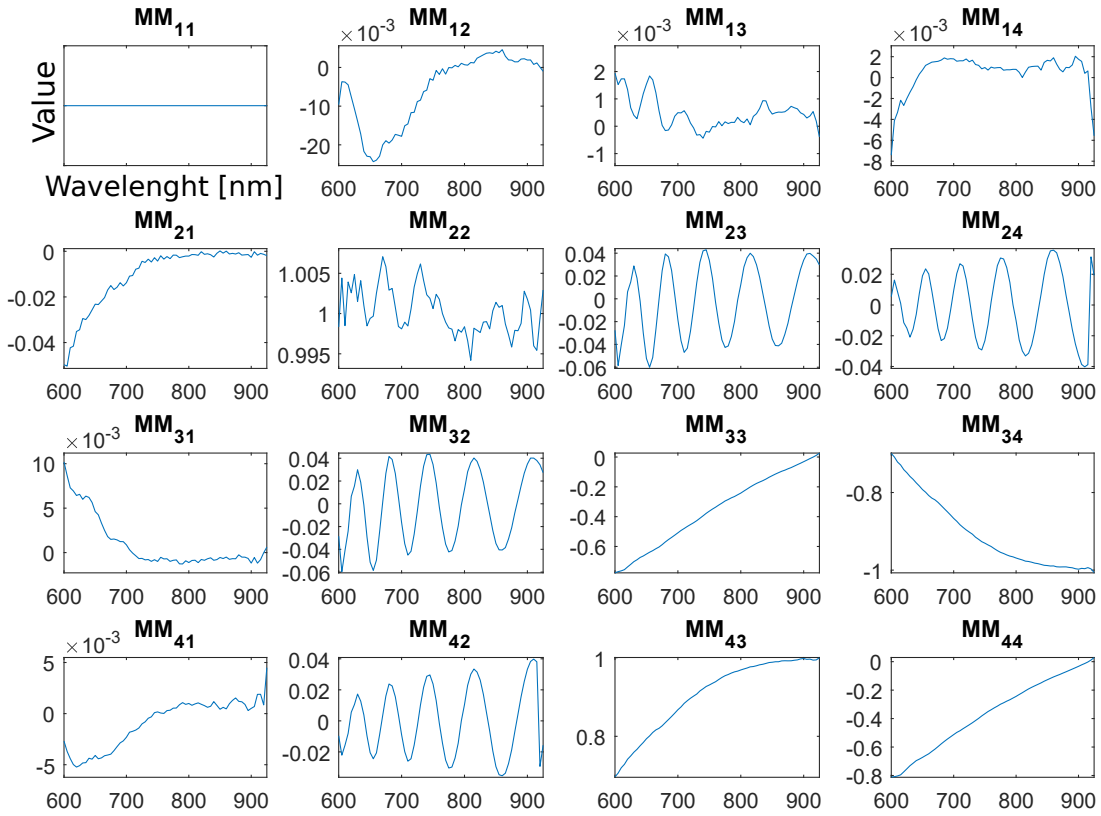

Figure 35 (d): The Mueller matrix elements of the retarder reference sample.

through all FLC states for each wavelength. Due to the drifiting of the FLCs, however, the former solution was much faster. The delay in the program is therefore not more than 3.2 seconds, which is acceptable.

When 100 detector measurements are performed for each wavelength and state, a complete Mueller matrix measurement takes about 20 seconds. Reducing the number of measurements to e.g. 10 will greatly lower the total measure time, but may compromise the quality of the complete measurement. Many different setups were tested and different numbers of measurements used. It was difficult to determine exactly how many detector measurements were necessary, but in most cases 100 measurements proved adequate. Further testing with reduction of this number should be performed in order to optimise the complete measurement.

High quality results were achieved in the 700 to 930 nm regime, and it is believed that this regime can be expanded down to 600 nm. Acquire good results further into the infrared regime remains a challenge that will require some attention. The combination of

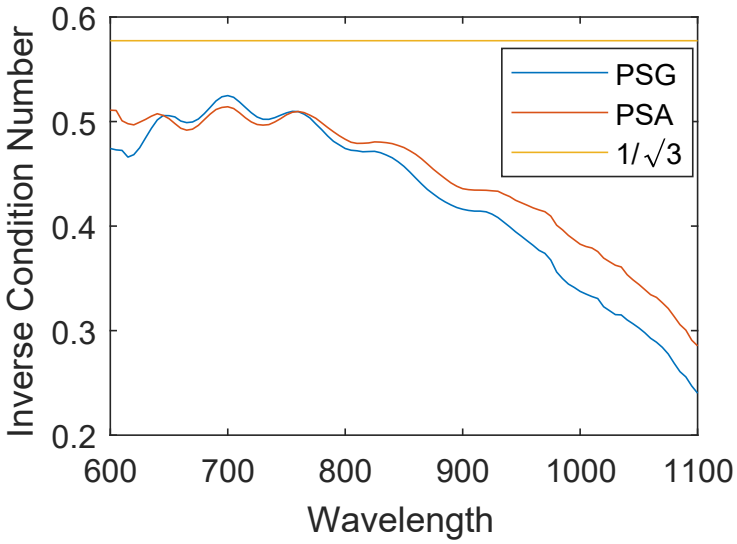

Figure 36: The wavelength dependent inverse condition number for the PSG and PSA compared to the maximum theoretical value in the 600 to 1100 nm regime.

a supercontinuum laser source and FLCs is believed to be suitable for imaging, and there are some suggestions on how this can be done. One solution involves beam expansion in order to image an area of 1-2 cm in diameter. A different approach is microscopic imaging for high resolution images of small areas. In either case, the acquisition of suitable achromatic lenses and a camera fit for the visible and near infrared regime is required. One should also be aware of possible *Speckle* in such an imaging system, which is observed as a randomly dotted pattern [92]. Speckle is interference caused by a highly spatially coherent source transmitted through or reflected in a rough surface. Due to the high spatial coherence of the laser speckle can occur upon interraction with the surface of the lenses, but may be resolved by the introduction of a diffuser.

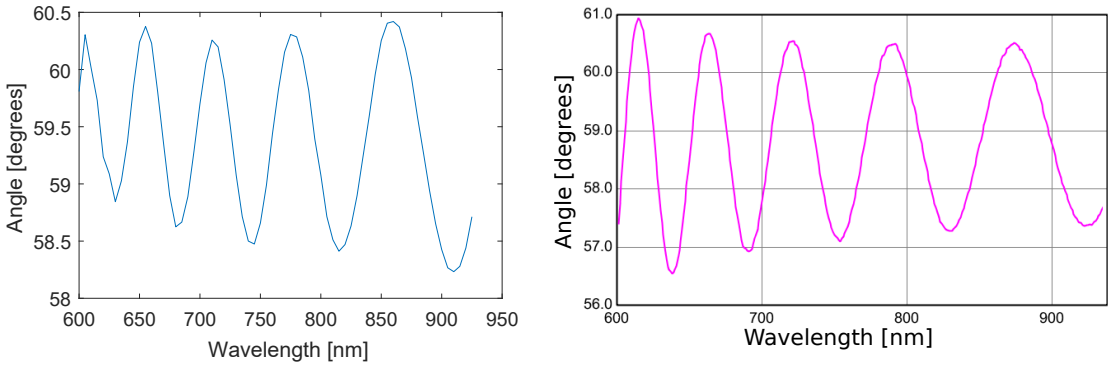

(a) **(b)**

Figure 37: Figure (a) shows the orientation of the retarder found through forward product decomposition in the 600 to 930 nm regime. Figure (b) is an RC2 measurement of the angle in the same regime.

6.2 Surface Studies of Multilayer Thin Films

The surface of the multilayered films were studied with different tools in the NTNU NanoLab. The goal was to ensure purity of the samples and low surface roughness.

6.2.1 Scanning Electron Microscopy

The study of the films using SEM was important as it revealed a problem, that if not detected early, might have led to a lot of confusion.

The effect of spitting, explained in section 4.2, is clearly visible in Figure 38. Spheres varying from some tens of nanometers to a micrometer in diameter cover the entire surface of the film, occupying roughly 5% of the area. A linescan was performed in order to ensure that these spheres were made of Au, and this was confirmed. The film investigated here is a simple 40 nm Au on Si-substrate film.

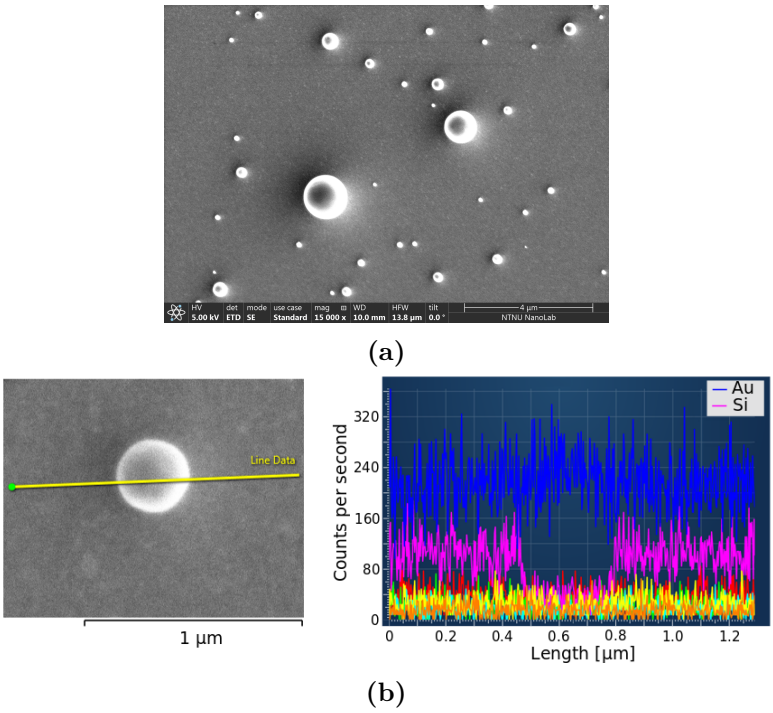

Figure 38: Figure (a) shows large spheres of Au covering the entire surface of the Au film on an SI-substrate. One of these spheres was studied with a linescan, where the SEM is able to determine what material is being investigated. The picture was taken in Standard mode, with 5.0 kV electron energy and detection of secondary electrons was performed using an ETD detector. The working distance was set to 10.0 mm. The right side of Figure (b) shows how the amount of Si drops when the sphere is being scanned, while the amount of Au is constant.

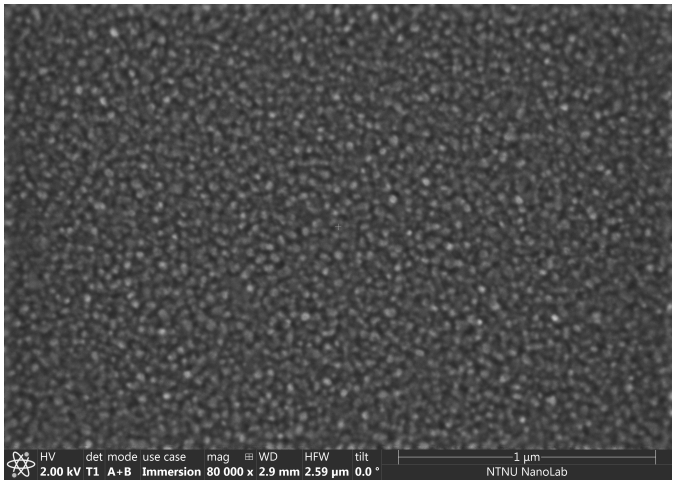

Figure 39: The complete multilayered film surface studied in SEM.

The issue with spitting was, however, resolved and the surface of a complete multilayered film is shown in Figure 39. It is clear from this image that the spitting was no longer a problem, and one can even see the contours of the surface roughness. This was, however, examined more thoroughly with an AFM.

6.2.2 Atomic Force Microscopy

Surface roughness was properly investigated with an atomic force microscope. The resulting images are shown in Figure 40 and numerical values listed in Table 4. The studied areas are about 500 × 500 nm.

It is clear that the Si-wafer is a highly suitable substrate when a low surface roughness is of importance. Once the issue with spitting was resolved, the Au layer also gave a satisfying result, with a sub nm root mean square (RMS) roughness. The roughness of the RF sputtered SiO_2 was higher than for Au, but Bhatt et. al show similar results [93]. The roughness of the complete multilayered film was in accordance with the roughness of the underlying layers, and was satisfyingly smooth for the intended purpose of nanostructuring.

Table 4: Surface root mean square (RMS) roughness for different samples made in the NanoLab.

	Si-wafer	Au on Si-wafer
RMS Roughness [nm]	0.257	0.786
	SiO_2 on Si-wafer	A complete multilayered film
RMS Roughness [nm]	1.485	1.547

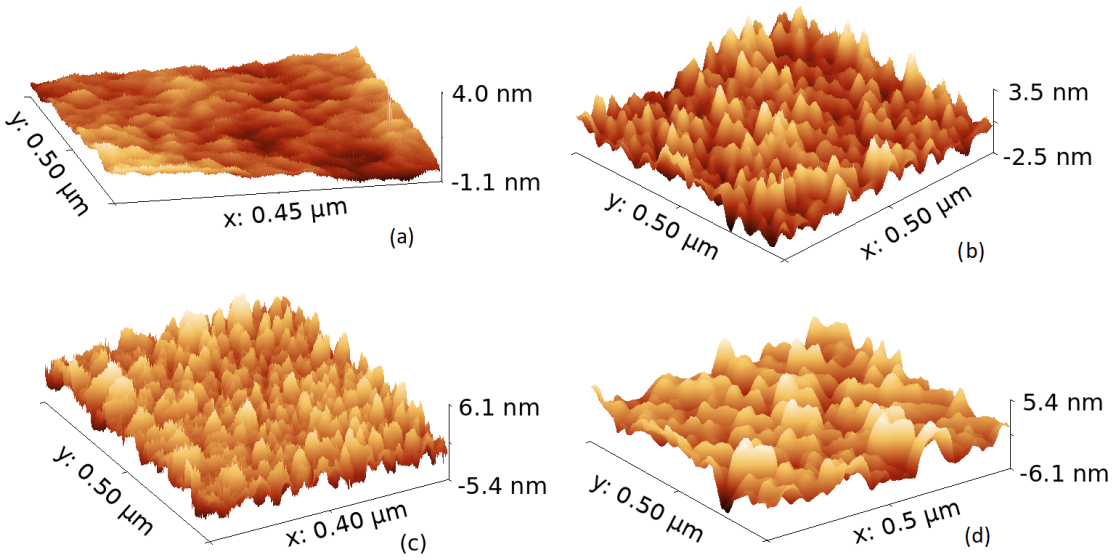

Figure 40: An atomic force microscope was used to find the surface roughness of (a) an Si wafer, (b) an Au film, (c) an SiO_2 film, and (d) a complete multilayered film. The RMS roughness values are listed in Table 4.

6.2.3 3D Optical Profiler

In contrast to the studies performed using AFM, a significantly larger area of a complete film was studied with a 3D optical profiler. The studied area was 95 × 71 micrometer and was studied in PSI mode with a green light source. The resulting image is shown in Figure 41, and exhibits a surface roughness similar to that found using AFM.

6.2.4 RC2 Measurements and Models

6.2.5 Au Layer

Two Au films of ∼30 and ∼40 nm thickness were made in order to construct a good ellipsometric model. Both films were electron beam evaporated on a pre-cleaned Si-wafer with an assumed deposition rate of 5.0 Å/s. The (N,C,S) values for the two films and the corresponding Au model is shown in Figure 43. In accordance with the theory presented in section 2.7, the Druide model dominated the longer wavelengths, while multiple Tauc-Lorentz models dominate the shorter wavelength regime. The resulting MSE is, as can be seen from Table 5, as low as 2.702, which is a satisfying result. Studies of the Au model showed that Au was close to opaque for thicknesses surpassing ∼60 nm.

To construct the model, first the film thickness was found. This was done by data using various existing models for Au. The surface roughness was set to 1 nm since

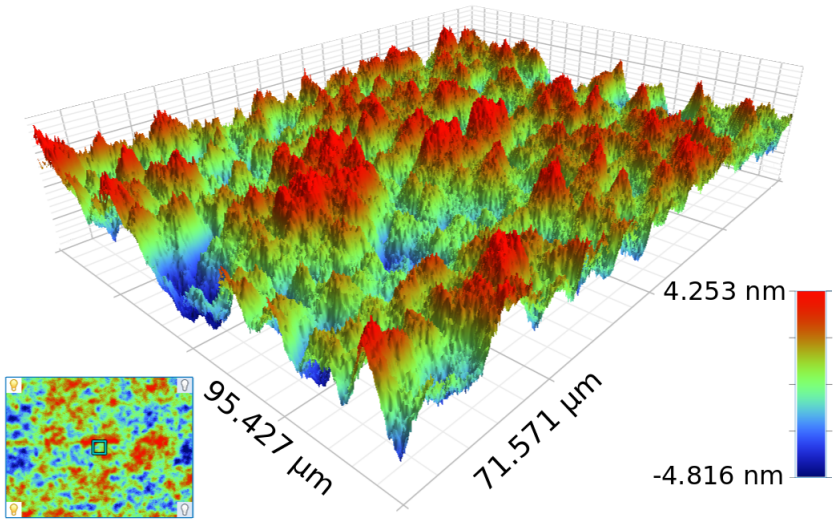

Figure 41: The complete multilayered film surface studied in a 3D optical profiler.

this was within close proximity of the results found using AFM. Once film thickness was determined, the model was built by introducing the Druide and Tauc-Lorentz oscillations and fitting the parameters. The optical e1 and e2 constants for the constructed model are graphed in Figure 42. The thickness of the films were about 15 % higher than expected. The true deposition rate must therefore have been closer to 5.8 Å/s.

Table 5: Model of two Au films on an Si substrate. The films were made to be about 30 and 40 nm thick, but the true thickness was measured and is shown here. The MSE shown is a combined MSE for the Au films and SiO_2 films.

Film	Thickness [nm]	Roughness [nm]	MSE
Au 30 nm	35	1.0	2.702
Au 40 nm	47		

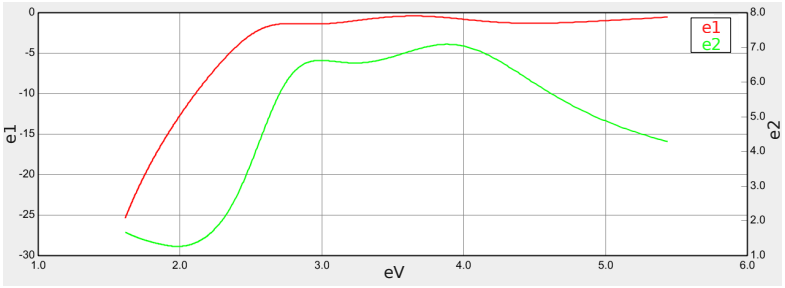

Figure 42: Optical constants e1 and e2 for the modelled Au layer.

Include Surface Roughness = ON Roughness = 1.00 nm
Layer # 1 = NanoLab Au Model Au Thickness = 47.04 nm (MSA)
Add Oscillator Show Dialog Fast Gaussian Calc = ON
Einf = 3.168
UV Pole Amp. = -260.1347 UV Pole En. = 15.000
IR Pole Amp. = 74.1746
Fit All Clear All Add Amp. Add Br. Add En.
1: Type = Tauc-Lorentz Amp1 = 59.9898
Br1 = 0.908 Eo1 = 2.660 Eg1 = 2.056 Common Eg = OFF
2: Type = Tauc-Lorentz Amp2 = 15.2769
Br2 = 2.027 Eo2 = 4.034 Eg2 = 1.021 Common Eg = OFF
3: Type = Tauc-Lorentz Amp3 = 38.2680
Br3 = 9.614 Eo3 = 8.945 Eg3 = 1.072 Common Eg = OFF
4: Type = Drude(RT) Resistivity (Ohm·cm)4 = 0.00021302 Scat. Time (fs)4 = 1.420
Substrate = Si

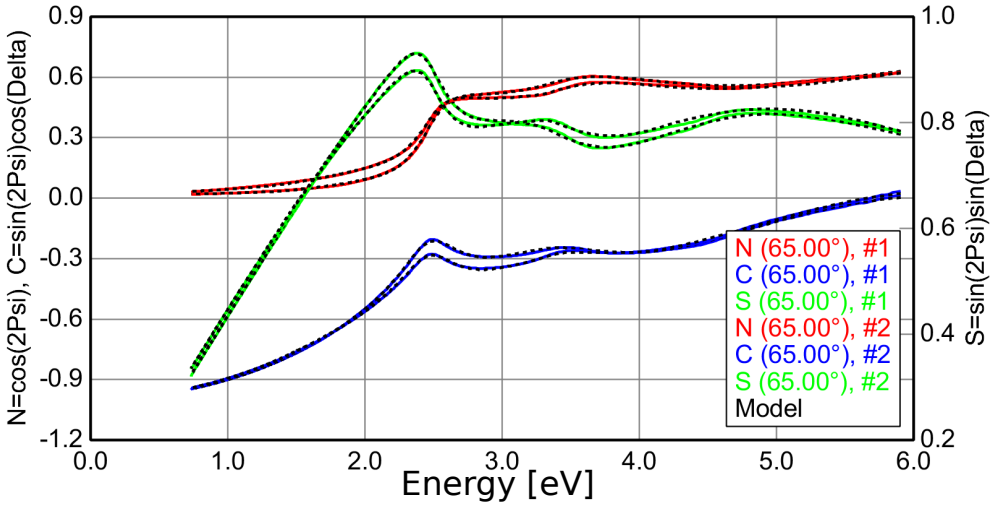

Figure 43: The modelled layer for Au and the corresponding (N,C,S) plot for the ∼30 and ∼40 nm film.

6.2.6 SiO_2 Layer

It was difficult to create a good model for the sputtered SiO_2. Numerous films were made, both directly on an Si substrate and on an opaque layer of Au. After some initial testing, the sputter rate at 300W and 3 mTorr Ar pressure was presumed to be $\sim$ 0.4 Å/s. The optical model of SiO_2 is based on three films of $\sim$ 30, $\sim$ 40, and $\sim$ 50 nm thickness, deposited on an Si wafer. The (N,C,S) plot of the films and the corresponding model is shown in Figure 44. As with the model for Au, the thickness of the SiO_2 films were found using other existing models. A Lorentz oscillation was then added due to some absorption in the UV-regime. This is visualised in the plot of the optical e1 and e2 constants in Figure 46. The roughness was set to 1.5 nm in accordance with the results from the AFM measurements.

As can be seen from Table 6, all films were measured to be about 10-15 % thicker than presumed. The actual sputter rate is therefore closer to 0.46 Å/s.

Table 6: SiO_2 films deposited either directly on an Si wafer or on an optical thick Au layer (∼100 nm). The SiO_2 layers were produced in various thicknesses. The target thickness of the SiO_2 layers is evident in the descriptive film name. The true SiO_2 film thicknesses were measured and are shown. The MSE shown is a combined MSE for the three SiO_2 films on Si and two SiO_2 films on Au, respectively.

Film	Thickness SiO_2[nm]	Roughness [nm]	MSE
SiO_2 30 nm on Si	32		
SiO_2 40 nm on Si	46	1.5	18.732
SiO_2 50 nm on Si	58		
SiO_2 35 nm on Au	38	1.5	29.637
SiO_2 45 nm on Au	49		

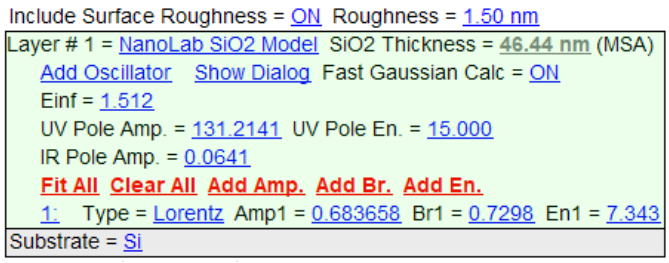

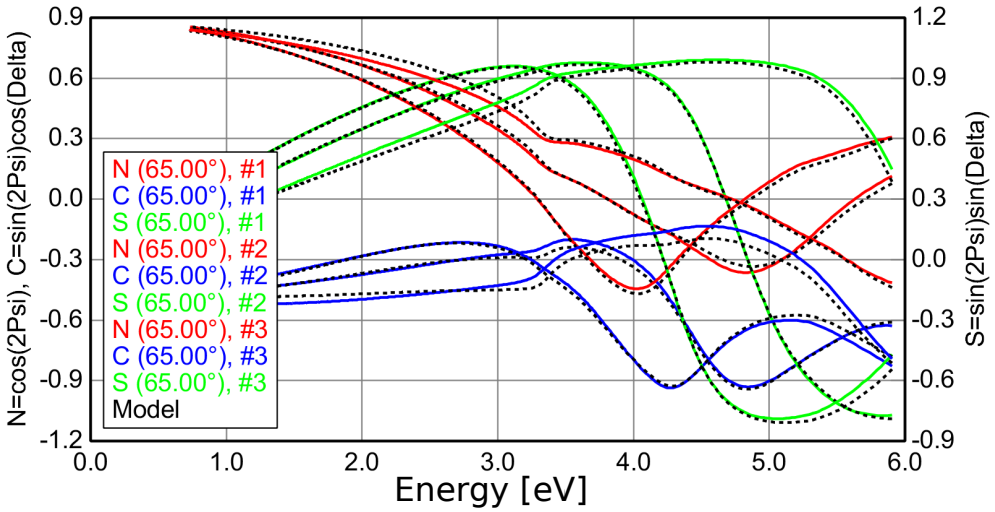

Figure 44: The modelled layer for SiO_2 and the corresponding (N,C,S) plot for the three films at 65° reflection.

Include Surface Roughness = ON Roughness = 1.50 nm
Layer # 2 = NanoLab SiO2 Model SiO2 Thickness = **48.67 nm** (fit)
Layer # 1 = NanoLab Au Model Au Thickness = 100.00 nm
Substrate = Si

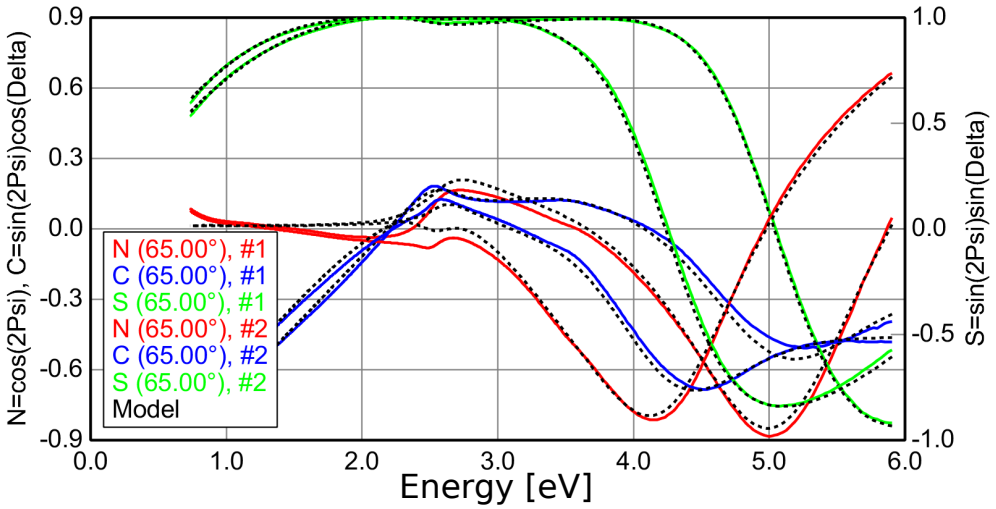

Figure 45: The modelled layer for SiO_2 on Au and the corresponding (N,C,S) plot for the two layers of SiO_2 on opaque Au at 65° reflection.

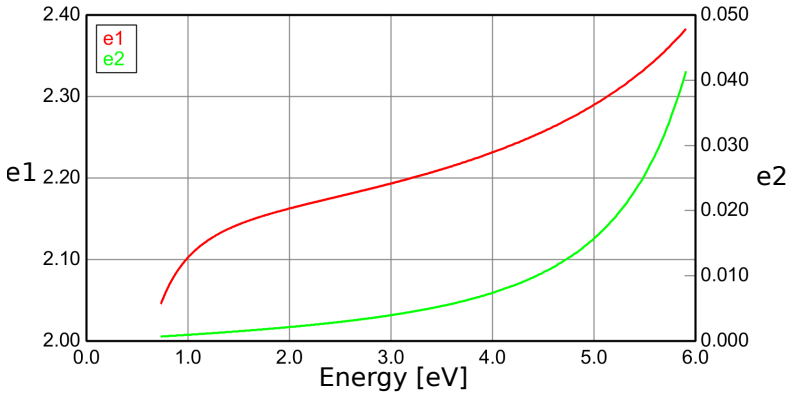

Figure 46: Optical constants e1 and e2 for the modelled SiO_2 layer.

6.2.7 A Complete Multilayered Film

The (N,C,S) measurement and the model of a complete multilayered film is shown in Figure 47. A standard model for Ti has been used, and seems to work well. The MSE

was found to be 3.760, which is a satisfying result.

This MSE is, surprisingly low, since one would expect the relatively high MSE from the modelled SiO_2 layer to affect the the end result in a more significant way. The reason for this unexpected result is believed to be the thickness of the top Au layer. An Au film of $\sim$ 60 nm or more is almost completely opaque, hiding all information about underlying films. The top Au layer of this multilayered sample is 46 nm, with an additional 3 nm of Ti before the SiO_2 layer is reached. Given these conditions, it is not surprising that results from the SiO_2 layer are suppressed compared to the ones from the top Au layer. It was desirable to make a multilayered film with a 30 nm Au top layer, to verify that the ellipsometric model was well suited. Unfortunately, the problem with spitting in the e-beam evaporator returned. Since this effect greatly alters the thickness and roughness, as well as the optical properties of Au, no more films were made within the time frame of this project.

The thickness of the Ti layers should also be reduced. The single purpose of Ti is to increase the adhesion between Au and SiO_2, but the thickness should be kept at a minimum since it otherwise may influence the optical properties in an unwanted way. Depending on the patterning method, the use of Ti may be skipped all together, but the resulting film will be extremely fragile. Modelling, however, will be simpler because the film consists of three, not five layers. If quality structuring is still achievable without the Ti layers, this may be a preferred solution.

6.2.8 Summary

Multiple films of different composition were made and tested with various instruments in order to determine surface roughness and optical properties. It was possible to construct solid optical models for both Au and SiO_2, especially the former. Both materials and the substrate showed sufficiently low surface roughness. An issue with spitting was detected and temporarily resolved. This is a complication that should be kept in mind when future deposition of Au is performed with this instrument. The deposition rate was 15% higher than expected for both materials, and the true deposition rate was found to be 5.8Å/s for Au and .44Å/s for SiO_2. Now that this is determined it will be possible to make films with a thickness uncertainty of $<$1 nm.

It was challenging to model the complete multilayered film due to the thickness of the top layer of Au. It is therefore recommended to decrease this thickness to 30 nm for easier modelling. This should be easy to realise now that the true deposition rate is determined.

The goal of creating a multilayered film that has been characterised, and is ready for nanostructuring, has been accomplished. The patterning technique suitable for this film is etching, since this method etches a pattern in an already existing layer, in this case Au. If one prefers to use the structuring method lift-off, however, this must be performed on a film that lacks the top Au layer, since this technique deposits a new pattern layer

Include Surface Roughness = ON Roughness = 1.50 nm
Layer # 5 = NanoLab Au Model Au Thickness = 46.21 nm
Layer # 4 = Ti Ti Thickness = 3.39 nm
Layer # 3 = NanoLab SiO2 Model SiO2 Thickness = 47.62 nm
Layer # 2 = Ti Ti Thickness = 3.00 nm
Layer # 1 = NanoLab Au Model Au Thickness = 100.00 nm
Substrate = Si

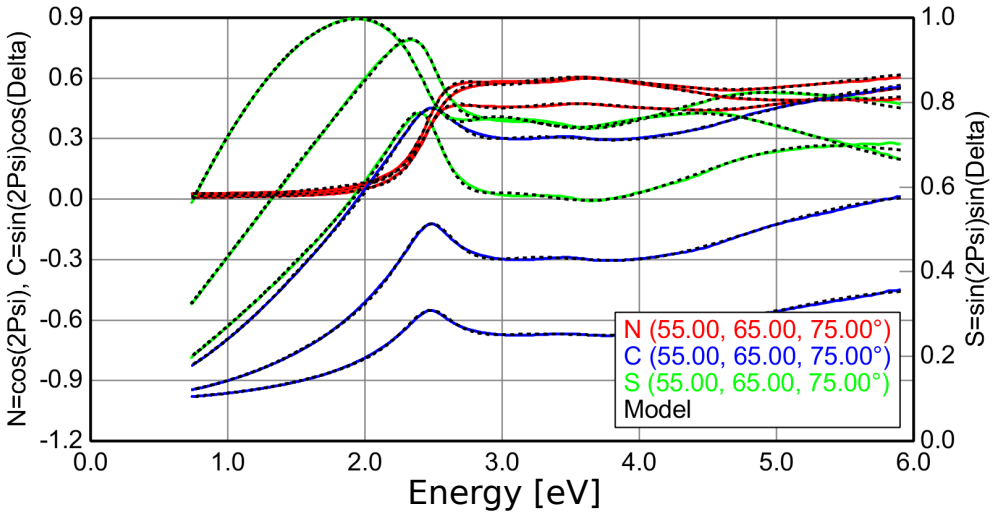

Figure 47: The modelled layer for the complete film and the corresponding (N,C,S) plot.

on top of an already existing film. Both methods should be tested in order to determine which gives the best result. Experiments on films without adhesive layers of Ti should also be performed, in order to see if these layers can be omitted.

7 Conclusion

A spectroscopic Mueller matrix ellipsometer in the 600 to 1100 nm range was built and calibrated. The bulk system was formed by a 2-ferroelectric liquid crystal (FLC) based polarisation state generator (PSG) and analyser (PSA), and an AOTF tunable high intensity supercontinuum laser source. The eigenvalue calibration routine displayed excellent results in the 700 to 930 nm regime, with a sub 2% Mueller matrix element error. The measured inverse condition numbers of the PSG and PSA were excellent in the visible regime. This is a good fundament for improvements of the Mueller matrix ellipsometer in the 600 to 700 nm regime, and options on how to achieve this have been discussed.

Both the FLCs and the ATOF source were investigated in terms of switching speed and stability. The source reached a stable state in less than 2 milliseconds, while the FLCs drifted slightly and reached a steady state 0.2 seconds after the switching of states was initiated. The total delay of 3.2 seconds constituted about 15% of the complete Muller matrix measurement in the 600 to 1100 nm range, and suggestions of how to resolve this problem have been discussed.

The experiments conclude that the supercontinuum laser source was highly suitable for Mueller matrix ellipsometry. The fast switching AOTF allowed measurements of complete Mueller matrices to be performed in seconds. In its current state, a spectroscopic Mueller matrix measurement from 600 to 1100 nm takes about 20 seconds, and suggestions have been given on how to considerably reduce this time. The system can also be easily changed to measure samples in reflection, and given its high performance, the system is deemed fit for development into an imaging system.

Production and characterisation of a multilayered thin film was a fundamental step in creating a beam splitting metasurface. Electron beam evaporation and sputtering was performed to make a film consisting of a bottom layer of opaque Au, an intermediate layer of $\sim$40 nm SiO_2, and a top layer of $\sim$40 nm Au, with adhesive layers of Ti in between. Studies of surface roughness were performed using Atomic Force Microscopy, Scanning Electron Microscopy, and 3D Optical Profilometry. Investigation of optical properties was done using a dual rotating compensator ellipsometer.

The surface roughness was found to be 1.5 nm, which is within an acceptable range. It was possible to construct a good optical model for each material, and thus a satisfying model for the complete multilayered film. The deposition rate for Au was 5.8Å/s, and for SiO_2, .44Å/s. The deposition rate was about 15% higher than expected for both materials. This caused a challenge, since the resulting thickness of the top Au layer made the model of a complete film depend almost entirely on the Au model. I therefore recommended reducing the top Au layer to 30 nm for the construction of an improved model, before structuring steps are initiated.

References

[1] F. R. S. J. Clerk Maxwell, "Viii. a dynamical theory of the electromagnetic field," *Phil. Trans. R. Soc. Lond.*, vol. 155, pp. 459–512, 1865.

[2] P. Drude, "Ueber oberflächenschichten. i. theil," 1889.

[3] P. Drude, "Ueber oberflächenschichten. ii. theil," 1889.

[4] K. L. Coulson, *Polarization and intensity of light in the atmosphere.* A. Deepak Publishing., 1988.

[5] D. Brewster, *"On the laws which regulate the polarisation of light by reflection from transparent bodies," Philosophical Transactions of the Royal Society of London*, pp. 125–159. London: Royal Scociety of London, 1815.

[6] A. Lakhtakia, "Would brewster recognize today's brewster angle?," *Optics News*, vol. 15, no. 6, pp. 14–18, 1989.

[7] J. McGregor, S. Temple, and G. Horváth, *Human Polarization Sensitivity*, pp. 303–315. Springer, Berlin, Heidelberg, 2014.

[8] M. Rothmayer, W. Dultz, E. Frins, Q. Zhan, D. Tierney, and H. Schmitzer, "Nonlinearity in the rotational dynamics of haidinger's brushes," *Applied Optics*, vol. 46, no. 29, pp. 7244–7251, 2007.

[9] R. Wehner, "Polarized-light navigation by insects," *Scientific American*, vol. 235, no. 1, pp. 106–115, 1976.

[10] H. G.Krapp, "Polarization vision: How insects find their way by watching the sky," *Current Biology*, vol. 17, no. 14, pp. R557–R560, 2007.

[11] S. Greif, I. Borissov, Y. Yovel, and R. A. Holland, "A functional role of the sky's polarization pattern for orientation in the greater mouse-eared bat," *Nature Communications*, vol. 5, no. 4488, 2006.

[12] R. Muheima, S. Sjöberga, and P. Rodrigueza, "Polarized light modulates light-dependent magnetic compass orientation in birds," *Proceedings of the National Academy of Sciences*, vol. 113, no. 6, p. 1654–1659, 2016.

[13] J. S. Tyo, D. L. Goldstein, D. B. Chenault, and J. A. Shaw, "Review of passive imaging polarimetry for remote sensing applications," *Applied Optics*, vol. 45, p. 5453, aug 2006.

[14] R. M. A. Azzam, "Division-of-amplitude Photopolarimeter (DOAP) for the Simultaneous Measurement of All Four Stokes Parameters of Light," *OPTICA ACTA*, vol. 29, no. 8, pp. 5–689, 1982.

[15] R. M. A. Azzam and K. A. Giardina, "Photopolarimeter based on planar grating diffraction," *Journal of the Optical Society of America A*, vol. 10, p. 1190, jun 1993.

[16] P. Lalanne, J. ome Hazart, P. Chavel, E. Cambril, and H. Launois, "A transmission polarizing beam splitter grating," *J. Opt. A: Pure Appl. Opt*, vol. 1, no. 99, pp. 215–219, 1999.

[17] J. Hough, "Polarimetry: a powerful diagnostic tool in astronomy," *Astronomy and Geophysics*, vol. 47, pp. 3.31–3.35, jun 2006.

[18] D. Yonetoku, T. Murakami, S. Gunji, T. Mihara, T. Sakashita, Y. Morihara, Y. Kikuchi, T. Takahashi, H. Fujimoto, N. Toukairin, Y. Kodama, and S. Kubo, "Gamma-Ray Burst Polarimeter (GAP) aboard the Small Solar Power Sail Demonstrator IKAROS," *Publications of the Astronomical Society of Japan*, vol. 63, pp. 625–638, jun 2011.

[19] S. Tan and R. M. Narayanan, "Design and performance of a multiwavelength airborne polarimetric lidar for vegetation remote sensing," *Applied Optics*, vol. 43, p. 2360, apr 2004.

[20] N. L. Seldomridge, J. A. Shaw, and K. S. Repasky, "Dual-polarization lidar using a liquid crystal variable retarder," *Optical Engineering*, vol. 45, p. 106202, oct 2006.

[21] A. G. Al-Rubaye, A. Nabok, and A. Tsargorodska, "Spectroscopic ellipsometry study of gold nanostructures for LSPR bio-sensing applications," *Sensing and Bio-Sensing Research*, vol. 12, pp. 30–35, feb 2017.

[22] D. Y. Lei, S. Kéna-Cohen, B. Zou, P. K. Petrov, Y. Sonnefraud, J. Breeze, S. A. Maier, and N. M. Alford, "Spectroscopic ellipsometry as an optical probe of strain evolution in ferroelectric thin films," *Optics Express*, vol. 20, p. 4419, feb 2012.

[23] M. Billardon and J. Badoz, "Modulateur de biréfringance," *Comptes Rendus de l'Académie des Science*, vol. 262, no. 11, 1966.

[24] G. E. Jellison and F. A. Modine, "Two-modulator generalized ellipsometry: theory," *Applied Optics*, vol. 36, no. 31, pp. 8190–8198, 1997.

[25] B. Wang and T. C. Oakberg, "A new instrument for measuring both the magnitude and angle of low level linear birefringence," *Review of Scientific Instruments*, vol. 70, no. 10, 1999.

[26] B. Wang, "Linear birefringence measurement instrument using two photoelastic modulators," *Optical Engineering*, vol. 41, no. 5, 2002.

[27] M. Bass, E. W. . V. Stryland, D. R. Williams, and W. L. . Wolfe, *Handbook of Optics Volume II; Devices, Measurements, and Properties, 2nd Ed.* McGRAW-HILL , INC, 1995.

[28] E. Compain and B. Drevillon, "High-frequency modulation of the four states of polarization of light with a single phase modulator," *Review of Scientific Instruments*, vol. 69, no. 4, p. 1574, 1998.

[29] E. Compain and B. Drevillon, "Complete high-frequency measurement of mueller matrices based on a new coupled-phase modulator," *Review of Scientific Instruments*, vol. 68, no. 7, p. 2671, 1997.

[30] D. Lara and C. Dainty, "Axially resolved complete mueller matrix confocal microscopy," *Applied Optics*, vol. 45, no. 9, pp. 1917–1930, 2006.

[31] E. Garcia-Caurel, A. Lizana, G. Ndong, B. Al-Bugami, C. Bernon, E. Al-Qahtani, F. Rengnez, and A. de Martino, "A mid-infrared mueller ellipsometer with pseudoachromatic optical elements," *Applied Optics*, vol. 54, no. 10, pp. 2776–2785, 2015. Export Date: 28 September 2015.

[32] S. Satirachat, P. Boonrod, W. Kerdsang, N. Haisirikul, and S. Suchat, "Polarization state control by using rotating quarter wave plate for the measurement by light," *Procedia Engineering*, vol. 8, pp. 243–247, 2011.

[33] A. D. Martino, E. Garcia-Caurel, J.-P. Gaston, and L. Yan, "Application of Spectroscopic Ellipsometry and Mueller Ellipsometry to Optical Characterization," *Applied Spectroscopy, Vol. 67, Issue 1, pp. 1-21*, vol. 67, pp. 1–21, jan 2013.

[34] S. Liu, W. Du, X. Chen, H. Jiang, and C. Zhang, "Mueller matrix imaging ellipsometry for nanostructure metrology," *Optics Express*, vol. 23, p. 17316, jun 2015.

[35] Y.-D. Chen, H. Y. Hsu, M. I. Khaleel, Y.-C. Chang, C.-H. Wu, and H.-C. Wu, "Study of biological reaction in cancer cell with spectroscopic imaging ellipsometry," vol. 9925, p. 992505, International Society for Optics and Photonics, sep 2016.

[36] M. I. Khaleel, Y.-D. Chen, C.-H. Chien, and Y.-C. Chang, "Sensing of Streptococcus mutans by microscopic imaging ellipsometry," *Journal of Biomedical Optics*, vol. 22, p. 056005, may 2017.

[37] D. Chan, "Optical investigations of bioorganic systems by spectrally resolved ellipsometry," 2005.

[38] J. Vizet, J. Rehbinder, S. Deby, S. Roussel, A. Nazac, R. Soufan, C. Genestie, C. Haie-Meder, H. Fernandez, F. Moreau, and A. Pierangelo, "In vivo imaging of uterine cervix with a Mueller polarimetric colposcope," *Scientific Reports*, vol. 7, p. 2471, dec 2017.

[39] A. Pors, O. Albrektsen, I. P. Radko, and S. I. Bozhevolnyi, "Gap plasmon-based metasurfaces for total control of reflected light," *Scientific Reports*, vol. 3, p. 2155, jul 2013.

[40] B. E. F. Fladmark, "Utvikling og implementering av et nytt spektroskopisk ellipsometerved bruk av liquid crystal variable retarders," Master Thesis, Norwegian University of Science and Technology, August 2012.

[41] L. M. S. Aas, P. G. Ellingsen, B. E. Fladmark, P. A. Letnes, and M. Kildemo, "Overdetermined broadband spectroscopic Mueller matrix polarimeter designed by genetic algorithms," *Optics Express*, vol. 21, p. 8753, apr 2013.

[42] P. G. Ellingsen, "Unpublished results,"

[43] P. A. Letnes, I. S. Nerboe, L. M. S. Aas, P. G. Ellingsen, and M. Kildemo, "Fast and optimal broad-band stokes/mueller polarimeter design by the use of a genetic algorithm," *Optics Express*, vol. 18, no. 22, pp. 23095–23103, 2010.

[44] L. M. S. Aas, P. G. Ellingsen, and M. Kildemo, "Near infra-red Mueller matrix imaging system and application to strain imaging," sep 2010.

[45] L. M. S. Aas, P. G. Ellingsen, M. Kildemo, and M. Lindgren, "Dynamic Response of a fast near infra-red Mueller matrix ellipsometer," sep 2010.

[46] M. Born and E. Wolf, *Principles of Optics, Fourth Edition*, p. 29. Oxford: Pergamon Press, 1970.

[47] R. C. Jones, "A new calculus for the treatment of optical systems.," *J. Opt. Soc. Am*, vol. 31, pp. 488–493, 1941.

[48] E. by John Daintith, *A Dictionary of Chemistry*, p. 371. Oxford: Oxford University Press, 6th ed., 2008.

[49] Z. Chen, T. Zeng, B. Qian, and J. Ding, "Complete shaping of optical vector beams," *Optics Explress*, vol. 23, 2015.

[50] N. G. Parke, "Matrix algebra of electromagnetic waves," *Technical Report no. 70*, vol. 24, 1948.

[51] A. B. Kostinski, C. R. Givens, and J. M. Kwiatkowski, "Constraints on mueller matrices of polarization optics," *Applied Optics*, vol. 32, no. 9, pp. 1646–1651, 1993.

[52] A. B. Kostinski, "Depolarization criterion for incoherent scattering," *Applied Optics*, vol. 31, no. 18, pp. 3506–3508, 1992.

[53] J. J. Gil, "Transmittance constraints in serial decompositions of depolarizing mueller matrices: the arrow form of a mueller matrix," *Journal of the Optical Society of America A*, vol. 30, no. 4, pp. 701–707, 2013.

[54] J. J. Gil and E. Bernabeu, "Depolarization and polarization indices of an optical system," *Optica Acta: International Journal of Optics*, vol. 33:2, pp. 185–189, 1986.

[55] R. M. A. Azzam, "Propagation of partially polarized light through anisotropic media with or without depolarization: A differential 4×4 matrix calculus," *Journal of the Optical Society of America*, vol. 68, no. 12, pp. 1756–1767, 1978.

[56] R. Ossikovski, "Differential matrix formalism for depolarizing anisotropic media," *Optics Letters*, vol. 36, no. 12, pp. 2330–2332.

[57] H. Noble and R. Chipman, "Mueller matrix roots algorithm and computational considerations," *Optical Express*, vol. 20.1, 2012.

[58] R. Ossikovski, "Differential and product mueller matrix decompositions: a formal comparison," *Optics Letters*, vol. 37, no. 2, pp. 220–222, 2012.

[59] S.-Y. Lu and R. A. Chipman, "Interpretation of mueller matrices based on polar decomposition," *Journal of the Optical Society of America A*, vol. 13, no. 5, pp. 1106–1113, 1996.

[60] S. Manhas, M. K. Swami, P. Buddhiwant, N. Ghosh, P. K. Gupta, and K. Singh, "Mueller matrix approach for determination of optical rotation in chiral turbid media in backscattering geometry," *Optics Express*, vol. 14, no. 1, pp. 190–202, 2006.

[61] P. A. Franken, A. E. Hill, C. W. Peters, and G. Weinreich, "Generation of Optical Harmonics," *Physical Review Letters*, vol. 7, pp. 118–119, aug 1961.

[62] R. R. Alfano and S. L. Shapiro, "Observation of Self-Phase Modulation and Small-Scale Filaments in Crystals and Glasses," *Physical Review Letters*, vol. 24, pp. 592–594, mar 1970.

[63] J. M. Dudley, G. Genty, and S. Coen, "Supercontinuum generation in photonic crystal fiber," *Reviews of Modern Physics*, vol. 78, pp. 1135–1184, oct 2006.

[64] R. Paschotta, "Article on "Photonic Crystal Fibers"," *Encyclopedia of Laser Physics and Technology*.

[65] I. T. Sorokina, V. V. Dvoyrin, N. Tolstik, and E. Sorokin, "Mid-IR Ultrashort Pulsed Fiber-Based Lasers," *IEEE Journal of Selected Topics in Quantum Electronics*, vol. 20, pp. 99–110, sep 2014.

[66] R. Paschotta, "Article on "Four-wave Mixing"."

[67] M. Sheik-Bahae, D. J. Hagan, and E. W. Van Stryland, "Dispersion and band-gap scaling of the electronic Kerr effect in solids associated with two-photon absorption," *Physical Review Letters*, vol. 65, pp. 96–99, jul 1990.

[68] R. Paschotta, "Article on "Raman Scattering","

[69] L. Bei, G. I. Dennis, H. M. Miller, T. W. Spaine, and J. W. Carnahan, "Acousto-optic tunable filters: fundamentals and applications as applied to chemical analysis techniques," *Progress in Quantum Electronics*, vol. 28, pp. 67–87, jan 2004.

[70] P. B. Johnson and R. W. Christy, "Optical Constants of the Noble Metals," *Physical Review B*, vol. 6, pp. 4370–4379, dec 1972.

[71] S. A. Maier, *Plasmonics: Fundamentals and Applications*. New York, NY: Springer US, 2007.

[72] T. Oates, H. Wormeester, and H. Arwin, "Characterization of plasmonic effects in thin films and metamaterials using spectroscopic ellipsometry," *Progress in Surface Science*, vol. 86, pp. 328–376, dec 2011.

[73] J. Tauc, R. Grigorovici, and A. Vancu, "Optical Properties and Electronic Structure of Amorphous Germanium," *physica status solidi (b)*, vol. 15, no. 2, pp. 627–637, 1966.

[74] A. R. Forouhi and I. Bloomer, "Optical dispersion relations for amorphous semiconductors and amorphous dielectrics," *Physical Review B*, vol. 34, pp. 7018–7026, nov 1986.

[75] H. Fujiwara and Wiley InterScience (Online service), *Spectroscopic ellipsometry : principles and applications*. John Wiley & Sons, 2007.

[76] R. M. A. Azzam, "Arrangement of four photodetectors for measuring the state of polarization of light," *Optics Letters*, vol. 10, pp. 309–311, 1985.

[77] F. Stabo-Eeg, M. Kildemo, I. Nerbo, and M. Lindgren, "Well-conditioned multiple laser mueller matrix ellipsometer," *Optical Engineering*, vol. 47, no. 7, 2008.

[78] G. H. Golub and C. F. V. Loan, *Matrix Computations*, pp. 52–59. Baltimore: The Johns Hopkins University Press, 1996.

[79] J. S. Tyo, "Noise equalization in stokes parameter images obtained by use of variable-retardance polarimeters," *Optics Letters*, vol. 25, no. 16, pp. 1198–1200, 2000.

[80] E. Compain, S. Poirier, and B. Drevillon, "General and self-consistent method for the calibration of polarization modulators, polarimeters, and mueller-matrix ellipsometers.," *Applied optics*, vol. 38, pp. 3490–3502, jun 1999.

[81] L. M. S. Aas, *Mueller Matrix Imaging and Spectroscopy*. PhD thesis, NTNU, November 2013.

[82] S. T. Lagerwall and I. Dahl, "Ferroelectric liquid crystals," *Molecular Crystals and Liquid Crystals*, vol. 114, pp. 151–187, 1984.

[83] V. S. Hagen, "Advanced mueller matrix imaging ellipsometry," Master Thesis, Norwegian University of Science and Technology, August 2014.

[84] D. W. Berreman, "Optics in Stratified and Anisotropic Media: 4×4-Matrix Formulation," *Journal of the Optical Society of America*, vol. 62, p. 502, apr 1972.

[85] H. Wöhler, G. Haas, M. Fritsch, and D. A. Mlynski, "Faster 4 × 4 matrix method for uniaxial inhomogeneous media," *Journal of the Optical Society of America A*, vol. 5, p. 1554, sep 1988.

[86] S. Teitler and B. W. Henvis, "Refraction in Stratified, Anisotropic Media*," *Journal of the Optical Society of America*, vol. 60, p. 830, jun 1970.

[87] P. Yeh, "Optics of anisotropic layered media: A new 4 × 4 matrix algebra," *Surface Science*, vol. 96, pp. 41–53, jun 1980.

[88] H. G. Tompkins and E. A. Irene, *Handbook of ellipsometry*. William Andrew Pub., 2005.

[89] T. E. Everhart and R. F. M. Thornley, "Wide-band detector for micro-microampere low-energy electron currents," *Journal of Scientific Instruments*, vol. 37, pp. 246–248, jul 1960.

[90] A. Harasaki, J. Schmit, and J. C. Wyant, "Improved vertical-scanning interferometry," *Applied Optics*, vol. 39, p. 2107, may 2000.

[91] P.-S. Shaw, T. C. Larason, R. Gupta, S. W. Brown, and K. R. Lykke, "Improved Near-Infrared Spectral Responsivity Scale," *Journal of Research of the National Institute of Standards and Technology [J. Res. Natl. Inst. Stand. Technol*, vol. 105, no. 105, pp. 689–700.

[92] H. M. Pedersen, "Compendium tfy4195 optics, ntnu,"

[93] V. Bhatt and S. Chandra, "Silicon dioxide films by RF sputtering for microelectronic and MEMS applications," *Journal of Micromechanics and Microengineering*, vol. 17, pp. 1066–1077, may 2007.

A Jones Matrices

$$\begin{bmatrix} 1 & 0 \\ 0 & 1 \end{bmatrix}$$
Air

$$\begin{bmatrix} 1 & 0 \\ 0 & 0 \end{bmatrix} \qquad \begin{bmatrix} 0 & 0 \\ 0 & 1 \end{bmatrix} \qquad \frac{1}{2}\begin{bmatrix} 1 & 1 \\ 1 & 1 \end{bmatrix}$$
Horisontal polariser Vertical polariser 45°-polariser

$$\frac{1}{2}\begin{bmatrix} e^{i\delta_x} & 0 \\ 0 & e^{i\delta_y} \end{bmatrix}$$
Genreal waveplate

$$e^{-i\pi/4}\begin{bmatrix} 1 & 0 \\ 0 & i \end{bmatrix} \qquad e^{i\pi/4}\begin{bmatrix} 1 & 0 \\ 0 & -i \end{bmatrix}$$
QWP, Fast axis horisontal QWP, Fast axis vertical

$$e^{-i\pi/2}\begin{bmatrix} 1 & 0 \\ 0 & -1 \end{bmatrix} \qquad e^{i\pi/2}\begin{bmatrix} 1 & 0 \\ 0 & -1 \end{bmatrix}$$
QWP, Fast axis horisontal QWP, Fast axis vertical

$$\begin{bmatrix} cos(\theta) & -sin(\theta) \\ sin(\theta) & cos(\theta) \end{bmatrix}$$
Rotator

B Mueller Matrices

$$\begin{bmatrix} 1 & 0 & 0 & 0 \\ 0 & 1 & 0 & 0 \\ 0 & 0 & 1 & 0 \\ 0 & 0 & 0 & 1 \end{bmatrix}$$

Air

$$\frac{1}{2}\begin{bmatrix} 1 & 1 & 0 & 0 \\ 1 & 1 & 0 & 0 \\ 0 & 0 & 0 & 0 \\ 0 & 0 & 0 & 0 \end{bmatrix} \qquad \frac{1}{2}\begin{bmatrix} 1 & -1 & 0 & 0 \\ -1 & 1 & 0 & 0 \\ 0 & 0 & 0 & 0 \\ 0 & 0 & 0 & 0 \end{bmatrix} \qquad \frac{1}{2}\begin{bmatrix} 1 & 0 & 1 & 0 \\ 0 & 0 & 0 & 0 \\ 1 & 0 & 1 & 0 \\ 0 & 0 & 0 & 0 \end{bmatrix}$$

Horisontal polariser Vertical polariser 45°polariser

$$\begin{bmatrix} 1 & 0 & 0 & 0 \\ 0 & cos(2\theta) & sin(2\theta) & 0 \\ 0 & -sin(2\theta) & cos(2\theta) & 0 \\ 0 & 0 & 0 & 1 \end{bmatrix}$$

Rotator

$$\begin{bmatrix} 1 & 0 & 0 & 0 \\ 0 & 1 & 0 & 0 \\ 0 & 0 & cos(\delta) & sin(\delta) \\ 0 & 0 & -sin(\delta & cos(\delta) \end{bmatrix}$$

Retarder

$$\frac{\tau}{2}\begin{bmatrix} 1 & cos(2\alpha) & 0 & 0 \\ cos(2\alpha) & 1 & 0 & 0 \\ 0 & 0 & sin(2\alpha)cos(\delta) & sin(2\alpha)sin(\delta) \\ 0 & 0 & -sin(2\alpha)sin(\delta & sin(2\alpha)cos(\delta) \end{bmatrix}$$

Retarder and diattenuator.

$$\begin{bmatrix} 1 & 0 & 0 & 0 \\ 0 & cos^2(2\theta) + cos(\delta)sin^2(2\theta) & cos(2\theta)sin(2\theta) - cos(2\theta)cos(\delta)sin(2\theta) & sin(2\theta)sin(\delta) \\ 0 & cos(2\theta)sin(2\theta) - cos(2\theta)cos(\delta)sin(2\theta) & cos(\delta)cos^2(2\theta) + sin^2(2\theta) & -cos(2\theta)sin(\delta) \\ 0 & -sin(2\theta)sin(\delta) & cos(2\theta)sin(\delta) & cos(\delta) \end{bmatrix}$$

General Linear Retarder